2020

Plastic substrate design for enhanced light outcoupling from Organic Light Emitting Diodes (OLEDs)

Rajiv Kaudal
Iowa State University

Plastic substrate design for enhanced light outcoupling from Organic Light Emitting Diodes (OLEDs)

by

Rajiv Kaudal

A dissertation submitted to the graduate faculty

in partial fulfillment of the requirements for the degree of

DOCTOR OF PHILOSOPHY

Major: Condensed Matter Physics

Program of Study Committee:
Joseph Shinar, Co-major Professor
Ruth Shinar, Co-major Professor
Rana Biswas
Kai-Ming Ho
Curtis Struck

The student author, whose presentation of the scholarship herein was approved by the program of study committee, is solely responsible for the content of this dissertation. The Graduate College will ensure this dissertation is globally accessible and will not permit alterations after a degree is conferred.

Iowa State University

Ames, Iowa

2020

DEDICATION

To my daughter, ***Aayashree***.

TABLE OF CONTENTS

Page

LIST OF FIGURES

Page

LIST OF TABLES

Page

ACKNOWLEDGMENTS

I am grateful to my parents, my wife and her parents, my newborn daughter and, to my siblings and my brother in law.

I express my sincere gratitude to both of my major advisors; Drs. Joseph and Ruth Shinar for their unwavering guidance throughout this dissertation work. Especially, I felt very fortunate to have Dr. Ruth Shinar, the PI of the one of the cutting-edge OLED research programs from EERE/DOE as my research mentor.

I would like to thank Dr. Rana Biswas for the supporting simulations in the project. I would also like to express my sincere gratitude to the team of MicroContinuum Inc., to its President and CTO Dr. Dennis Slafer and Diane Martin.

I am equally grateful to Dr. Eeshita Manna and Dr. Chamika Hippola who preceded me in the project.

Dr. Joong-Mok Park from Ames Laboratory helped me with my research work on several occasions.

Dr. Dusan Danilovic provided me encouragement throughout this dissertation. I am also thankful to my peers Joshua Wolanyk, Erik Dykstra, Raghunanadan B. Iyer, and Michael Fralaide.

I would like to thank DE-EE0007621 and DE-EE0008724 grants for supporting this work.

ABSTRACT

Enhancing light extraction from Organic Light Emitting Diodes (OLEDs) is an ongoing scientific and industrial challenge that is particularly important for lighting applications. Light extraction, or the outcoupling factor η_{out} of conventional OLEDs devoid of any extraction means is limited to ~20%. This limit stems mainly from three photon loss processes: (i) so-called "external" waveguiding in the substrate, (ii) internal waveguiding in the high refractive index anode and organic layers, and (iii) excitation of surface plasmon polaritons at the metal cathode/organic interface. The ~30% external waveguided light can be extracted via a microlens array or a hemispherical lens at the air-side of the OLEDs' substrate. However, mitigating the internal waveguided light and surface plasmon excitation losses, which amount to ~50% of the lost photons, in a cost-effective approach remains a challenge. Substrate corrugation is one of the innovative approaches used for addressing this issue. In this work, corrugated plastic substrates of polycarbonate and polyethylene terephthalate/cellulose acetate butyrate of various designs, such as different patterns' height and periodicity, were evaluated. Detailed substrates' design is a crucial metric for device performance; hence it requires in-depth analysis. Tapping mode atomic force microscopy (AFM) was used for probing the geometry, uniformity, and smoothness of the various plastic substrates. The essence of the work performed in this dissertation is combining promising substrate designs with carefully stacked green and white OLEDs that resulted in ~2x enhancements in η_{out} due to the patterns only, i.e., without additional means for extracting the externally waveguided light. In addition to broad optoelectronic characterization of the OLEDs, analyses of device stack conformality and top surface structure were performed via focused ion beam, SEM and AFM techniques.

CHAPTER 1. INTRODUCTION TO OLED TECHNOLOGY AND ATOMIC FORCE MICROSCOPY PART 1

1.1 Brief History of OLED Technology

A. Bernanose and co-workers observed first electroluminescence in organic materials with an application of high alternating voltage to acridine derivatives deposited on a cellophane thin film at the Nancy-Universite in France [1]. W. Helfrich & W.G. Sneider were the first to demonstrate EL from anthracene single crystal utilizing the invention of ohmic, dark-injecting electrodes by Pope's group in 1960 [2]. Later in 1983, EL from a thick polymer PVK (Poly (9-vinylcarbazole)) layer was also reported with high injecting electrodes [3]. All these devices required high driving voltage, hence were of limited practical applications.

The first breakthrough in the OLED technology came in the year of 1987 when Ching W.Tang and Steven Van Slyke showed a OLED with a NPB (N, N′-Di(1-naphthyl)-N,N'-diphenyl-(1,1'-biphenyl)-4,4'-diamine)/Alq_3 (Tris-(8-hydroxyquinolinato)aluminum) bilayer heterojunction structure [4]. This OLED had external quantum efficiency of 1% with maximum brightness exceeding 1000 Cd/m^2 at ~ 10 V. Later, Friend and coworkers demonstrated the first polymer LED (PLED) based on PPV [5]. The first flexible OLED was reported in 1992 by Grustafasson et al. on a Polyethylene terephthalate (PET) substrate [6]. Kido group from Japan were the first to demonstrate the White OLED with a maximal brightness of (~3400 Cd/m^2) [7]. Forrest and coworkers reported the first phosphorescent OLEDs based on PtOEP (Platinum octaethylporphyrin) in 1998 [8]. This work opened the new possibility of increasing efficiency of the OLED to 100 %. The first commercial OLED display was developed by Pioneer in 1997 [9].

1.2 OLED Structure

OLED, as shown in Figure 1.1, is an ultrathin organic layer of a few hundred nanometers stacked on the substrate often glass or plastic. The organic layers reside in between the electrodes, anode and cathode.

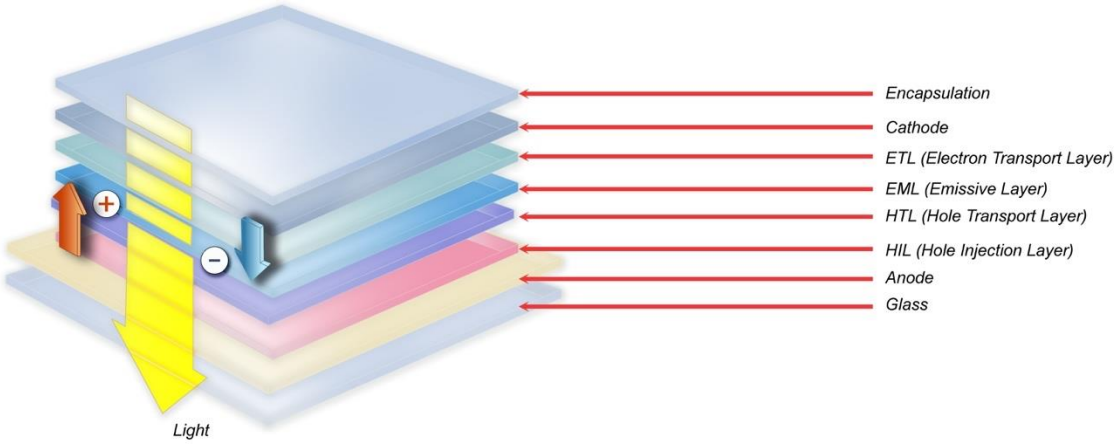

Figure 1.1: Schematic of an OLED with its various components

Figure 1.2 is the energy band diagram/energetics of an OLED on the forward bias that captures its working principle. Two major characteristics of an OLED are:

I. Diode/Rectifying character

Charge injection and their subsequent transport/drift are only possible if the energy/voltage supplied is sufficient to overcome the interface barrier due to band bending. This is favored only in the forward bias as opposed to steeper band bending on the reverse bias which forbids charge injection and its flow. This rectifying behavior of allowing charge flow in only one direction qualifies it as a diode.

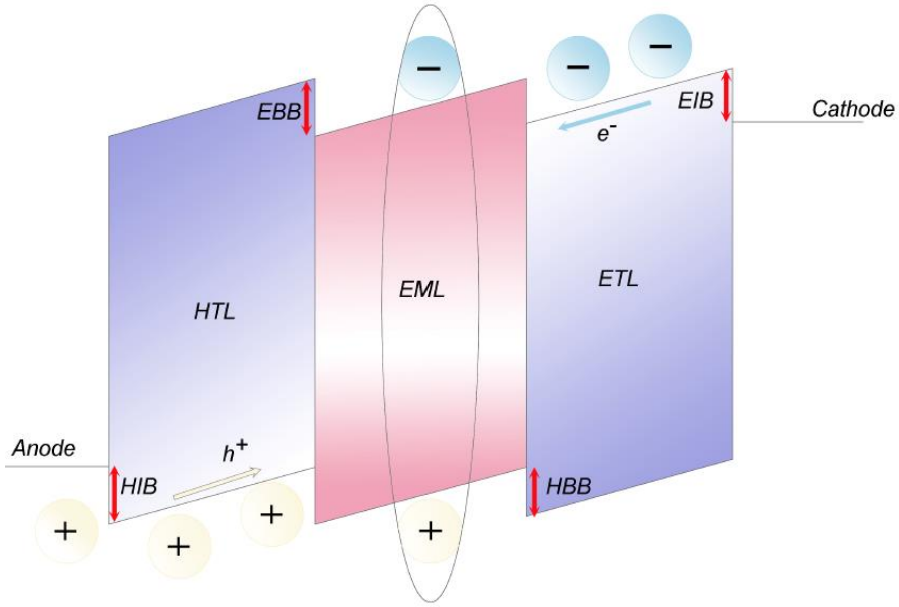

Figure 1.2: Energetics of an OLED structure

(EBB: Electron Blocking Barrier; EIB: Electron Injection Barrier; HBB: Hole Blocking Barrier; HIB: Hole Injection Barrier)

II. Electroluminescence

As the field is applied, hole (h^+) and electron (e^-) drift from opposite direction, perpendicularly to the stack plane, surpassing the barrier on the interfaces adjacent to the Emission zone. The next step is the formation of coulombic bound state of electron and hole which is energetically unstable and hence decay radiatively releasing photon/light.

1.3 Operating Principles

1.3.1 Organic Semiconductors: π-conjugated materials

The semiconducting behavior in organic compound arises due to the alternation of single and double bonds through the molecule or the polymer backbone [10]. This property also called π conjugation is possible due to sp^2 hybridization in carbon atoms. 3D projection of sp^2

hybridization for the ethylene molecule is shown in ***Figure 1.3***. In this hybridization 2s and two 2p (p_x and p_y) orbitals combined to form strongly localized sigma (σ) bonds aligning three equal energy sp orbitals in a triangular planar structure with an angle of 120° between them.

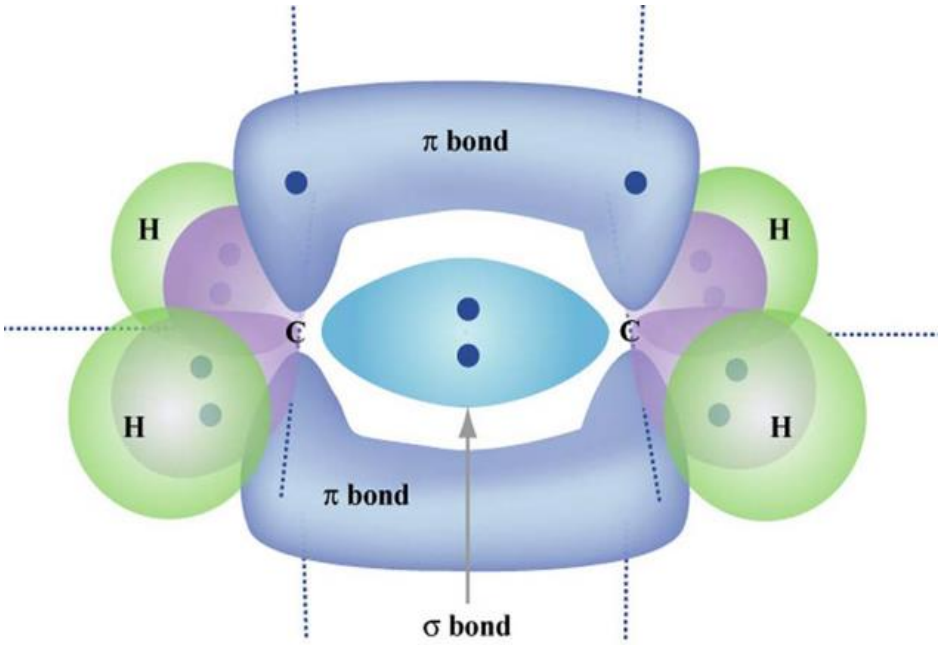

Figure 1.3: Molecular structure of ethylene showing sp^2 hybridization [11]

The remaining p_z orbital forms a π bond with another adjacent p_z orbital, perpendicular to the σ-bond plane. The electrons associated with the π bond is thus delocalized and capable of hopping from one molecule to another [10].

The semiconductor like band structures in π-conjugated materials can be explained through Molecular Orbital (MO) theory [12]. The molecular orbital wave function of the π bond can be expressed as a linear combination of atomic orbital wave function and their corresponding linear coefficients are determined by minimization of the total energy of the system. For instance, two p_z orbitals result in splitting of two energy levels; bonding and antibonding molecular orbitals. As Pauli exclusion principle limits two electrons on each energy state, the electrons will occupy only the ground state (bonding) of the π orbital.

In the molecular system with more carbon atoms, the two bonding and anti-bonding energy levels form quasi-continuous energy bands as shown in ***Figure 1.4***. The energy levels associated with bonding orbitals are occupied by electrons and are called Highest energy occupied molecular orbital (HOMO) level. The energy level associated with the antibonding orbitals remains empty and is referred as Lowest energy unoccupied molecular orbital (LUMO) level [10, 12]. The difference in these two levels is the band gap of the material which is an intrinsic property of the material. HOMO and LUMO level corresponds to the top of the valence and the bottom of the conduction band in inorganic semiconductor.

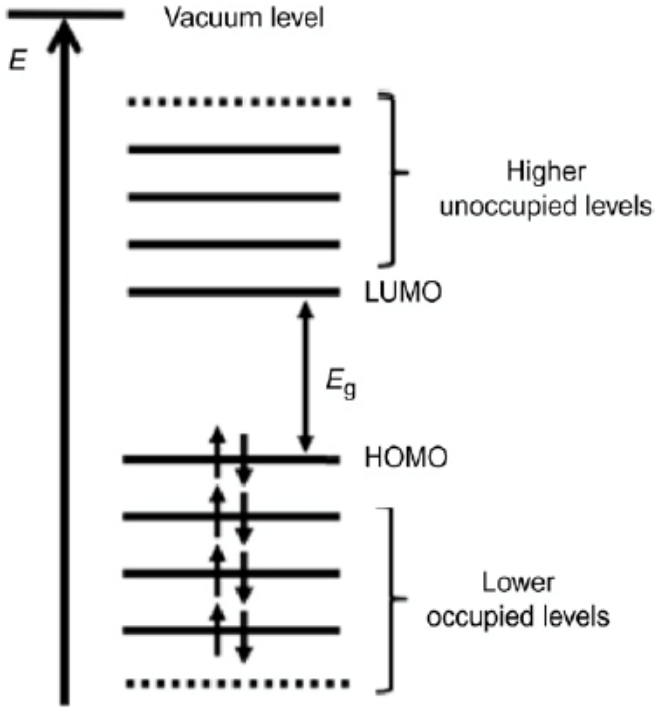

Figure 1.4: Electron distribution on the HOMO and LUMO level of Organic semiconductor [13]

1.3.2 Carrier injection from metal to organic semiconductors

OLED being a field-driven device operates on charge injection [14]. Following two factors are important for the charge injection:

I. Contact

Ohmic contact between the metal and the organic layer ensures effective charge injection in an OLED. In such contact, the interface barrier is minimal and thus require lower operational voltage. Contacts in reality, however are quasi-ohmic. Organic semiconductors, being highly disordered systems with trap states contribute to such behavior [14].

II. Carrier mobility

Transport phenomena in the organic semiconductor are bulk limited as the rate of the injected charge carriers is always greater than the transport capacity/charge mobility of the organic semiconductor [15].

The charge injection from metal to the organic layer is described by these two models:

I. Fowler-Nordheim Tunneling

This model as shown in ***Figure 1.5*** describes the lowering of the potential barrier due to the effect of the image charge potential and the electric field in the interface. Mathematically it is written as in ***Eqn***. ***1.1***,

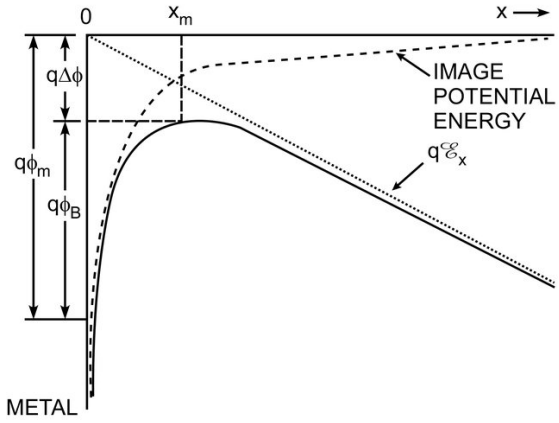

Figure 1.5: Potential barrier lowering due to the image potential and the field in the metal/organic semiconductor interface [16]

$$q\varphi_B(x) = q\varphi_m - qEx - \frac{q^2}{16\pi\epsilon x} \quad \text{.....} \quad 1.1$$

where x is the distance between the charge carrier and metal/organic interface and φ_m is the work function of the electrode. The second term in the right-hand side corresponds to the potential barrier reduction due to the applied electric field and the third term is the image potential formed at the interface [14].

II. Thermionic injection

It occurs when the thermal energy of the charge carrier exceeds the potential barrier. The thermionic current at any given temperature is governed by

$$J_{thermionic} = AT^2 e^{-\frac{q\varphi_B}{kT}} \quad \text{..... 1.2}$$

A is the Richardson constant, which depends on the carrier effective mass [14,17].

With the rise in the electric field, the triangular barrier grows shallower and the field-assisted tunneling or the FN tunneling becomes dominant. The injection current due to the tunneling of carriers through a narrow triangular barrier is of the following form

$$J_{FN\ tunneling} \propto \frac{q^3}{4h\varphi_B} E^2 e^{-\frac{8\pi\varphi_B^{1.5}\sqrt{2m^*}}{3hE}} \quad \text{..... 1.3}$$

The first term is the tunneling pre-factor and the rate of current backflow. FN tunneling prevails on the high electric field or at very high potential barrier regime [14].

1.3.3 Charge transport

The charge transport in organic semiconductor takes place via hopping rather than band like transport in inorganic semiconductor [18]. This is largely due to the localized state of the charge in organic materials. The localized energy states can be thought of as a series of potential wells that can trap a carrier [19,20]. Carrier surpasses the potential barrier through Lattice vibration (phonon-assisted) or with the applied electric field.

1.3.4 Exciton formation and recombination

The injected holes and electrons form energetically favorable polaron or bipolaron states within the molecule. This coulombically-correlated polarons of positive and negative nature are called an exciton [21].

Frenkel Exciton*:* Exciton radius for organic semiconductor is small as compared to the inorganic semiconductor. This stems from the fact that the dielectric constant of the organic material is $\epsilon \sim 3-5$ as compared to its $\epsilon > 10$ for inorganic semiconductor. As dielectric constant is inversely related to the binding energy, the exciton in organic semiconductor also called Frenkel exciton to have higher binding energy ~ 1 eV as compared to Wannier exciton in inorganic semiconductor [21].

Capture Radius*:* The physical quantity that governs the dissociation of the exciton is its capture radius (Rc), defined by,

$$\text{Rc} = \frac{e^2}{4\pi\epsilon\epsilon_0 K_B T} \quad \text{..... 1.4}$$

Recombination is possible only when electron and hole gain enough coulombic energy to surpass the thermal energy [22]. The capture radius is typical of ~ 15 nm for organic materials.

Field assisted dissociation and the charge accumulation at the interfaces are two major factors for exciton depletion via quenching mechanism [14].

1.3.5 Fluorescence/Phosphorescence

The spin states of the injected electrons and holes are statistically independent. The combination of the electron and hole pair can either form the singlet exciton (SE) state (total spin, S=0) or one of the three triplet exciton (TE) states (S=+1), with 0.25 and 0.75 probabilities respectively [23].

Jablonski diagram as depicted in ***Figure 1.6*** shows the optical transitions both due to photoexcitation as well as photoemission within the various electronic states of the molecules [25]. Primarily it is useful on accessing information of the transition made within a various vibrational level of an electronic state (Intra level transitions) or among the different electronic states (inter transitions).

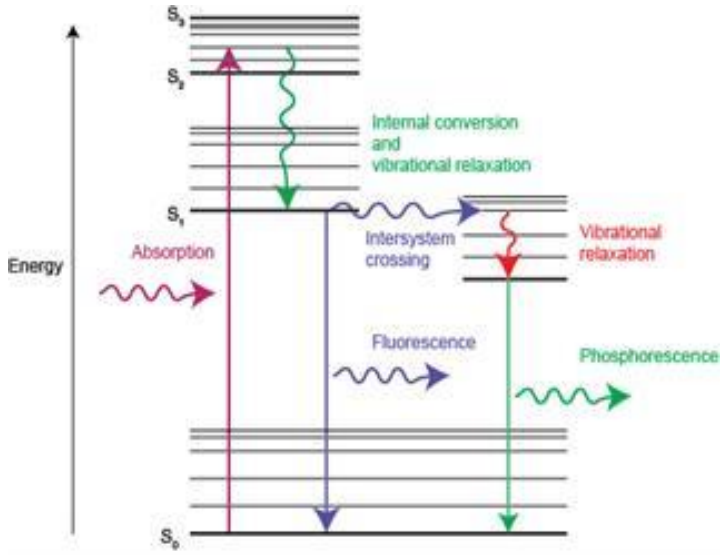

Figure 1.6: Jablonski diagram showing Photoluminescence [24]

Any transitions to higher electronic states require absorption of the photon as shown by the red line in ***Figure 1.6***. The excited state can decay to the ground state either radiatively or non-radiatively. Fluorescence and Phosphorescence are the two major mechanisms by which the excited state can decay radiatively to the ground state and are represented by the blue and green lines in ***Figure 1.6*** respectively.

The implication to OLED*:* As per the selection rule of optical transitions, recombination is allowed only within the similar spin configurations ($\Delta S = 0$) when the interaction between orbital and spin angular momentum is small. The ground state is a singlet state, spin conservation rule only allows SEs to decay radiatively to the ground state. This process of light emission

which is faster (t ~ 0.1ns -100 ns) by SEs is known as the fluorescence and provides the upper bound ~ 25% efficiency for Fluorescent OLEDs [26].

Phosphorescence, on the other hand, is a much slower process (t ~ 1 $\mu s - 10\ s$) and require presence of heavier elements like Ir, Pt in the molecule. The presence of such elements increases higher spin-orbit coupling due to the larger interaction between the spin and orbital angular momentum [26]. Under this condition, spin-orbit interaction is no longer forbidden ($\Delta S \neq 0$) leading radiative recombination of TEs to the ground state yielding 100 % Internal Quantum Efficiency (IQE). The large spin-orbit coupling due to the presence of the heavy metal in the molecule also enhances the probability of Inter System Crossing (ISC), non-radiative transitions from SEs to TEs. Thus, it is possible to have 100 % efficiency in Phosphorescent OLEDs [8].

1.3.6 Energy Transfer in OLEDs

Light sensitive materials undergo energy transfer either via radiative energy transfer or resonance energy transfer [26]. The former process requires; (i) overlap of the absorption and emission spectra of the acceptor and donor materials (ii) the acceptor molecules absorb the photon emitted by the donor molecule. In later processes, however there is no actual photon emission and reabsorption by the donor-acceptor molecules.

The implication to OLED: Coulombic (Förster Energy Transfer or FRET) or Electron exchange (Dexter Energy Transfer or DET) interaction between donor and acceptor molecules are the two major energy transfer mechanisms for guest/host system in an OLED. Both of these processes are shown in ***Figure 1.7***.

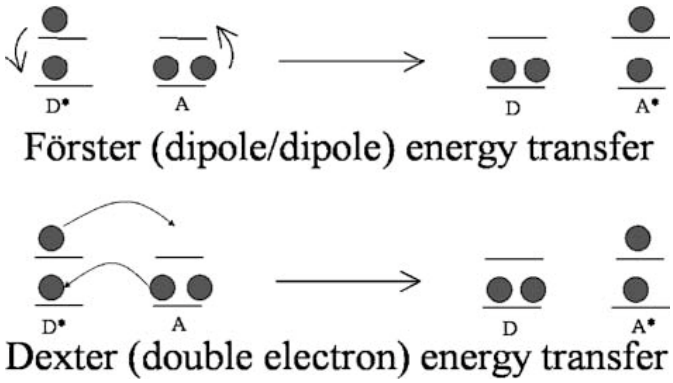

Figure 1.7: Schematic showing FRET and DET processes [27]

In FRET, excitons generated in the host molecule induce dipoles in the guest molecule. The energy transfer occurs via non-radiative dipole-dipole coupling between the inducing exciton donor field and induced acceptor field [28]. The efficiency of the FRET processes is very sensitive to the distance between acceptor and donor molecules and can be described by the following equation.

$$K_{FRET} = \frac{1}{\tau_H}({}^{R_0}/_{R})^6 \quad \text{.....} 1.5$$

where τ_H is the exciton lifetime for hole molecule, R is the distance between the host and guest molecule and R_0 is the Förster radius that depends on the overlap integral of the donor's emission spectra with acceptor's absorption spectra. FRET occurs when the distance between donor-acceptor molecules are within the range of 1-10 nm.

DET, on the other hand, is a short-range mechanism and typically occurs when the distance between donor-acceptor molecules is very small ($< 1\ nm$). It occurs through excited electron transfer from donor molecule to acceptor molecule [29]. This is a direct electron exchange process and requires overlap between donor-acceptor molecules. The energy transfer is given by the following equation

$$K_{DFT} \propto J\ e^{-2r/L} \quad \text{.....} 1.6$$

Here J is the spectral overlap integral between donor-acceptor molecules, r and L are the distance and sum of the Van der Waals radii of the donor-acceptor molecules respectively. This is more prevalent in phosphorescent OLEDs. Spin conservation in FRET is $\Delta S = 0$ whereas in DET, triplet to singlet or singlet to triplet state is allowed.

1.4 Light Extraction and OLED Efficiency

The optoelectronic characterization of an OLED is based on its Current-Luminance-Voltage (J-L-V) measurement. Current/luminous efficiency (Candela/Amp) and Power efficiency (Lumen/Watt) are obtained from the J-L-V measurement. The luminous efficiency is the ratio of the Brightness (Cd/m^2) to the Current density (Amp/m^2) and thus measures the amount of photon generated as current being injected. Power efficiency is representative of the voltage dependence and thus entails on the resistance issue.

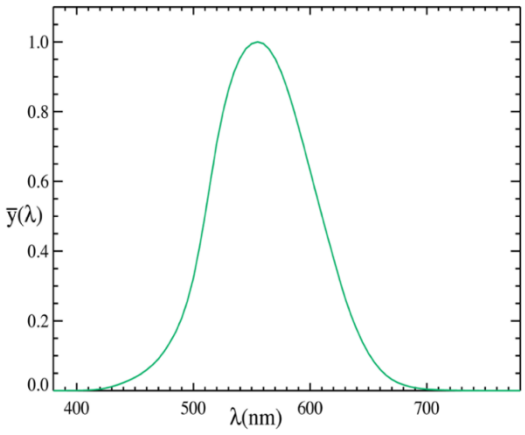

Figure 1.8: Photopic curve [30]

In general, the light flux generated in the forward direction depends on the light perception of human eyes, which is described by the luminosity function shown in ***Figure 1.8.*** The human eye is most sensitive $\lambda = 555\ nm$ and the perception goes down with the change of wavelength on either side of the peak [31]. It is thus crucial to use a different measure of

efficiency when comparing OLEDs with different EL spectra. External Quantum Efficiency (EQE) as a metric takes the photopic curve into account and hence is the most reliable quantity for the efficiency measurement. The external quantum efficiency (η_{EQE}) of an OLED is given by the number of photons generated per electrical charge injected without taking the emission wavelength into account

$$\eta_{EQE} = \eta_{OUT}\, \gamma r_{ex}\, \eta_{PL} \quad \text{..... 1.7}$$

where $\eta_{PL}$is the PL quantum yield, r_{ex} is the fraction of singlet or triplet excitons generated, γ is the charge balance factor, and η_{OUT} is the outcoupling efficiency [32,33]. For phosphorescent OLEDs all three factors except η_{OUT} can be optimized to 1.

Power efficiency (η_P) of the light source is the most important operational parameter and is given by

$$\eta_P = \theta\, \eta_{EQE}\, \frac{V_\lambda}{V} \quad \text{..... 1.8}$$

θ is the overlap of the light source with the spectral sensitivity of the eye, V_λ is related to the energy of the emitted photon, V is the operational voltage, η_{EQE} as defined in ***Eqn 1.7.*** It is clear that power efficiency decreases as V increases. The operating voltage as related to the device drive current and has an important influence on the device lifetime [32,34].

The outcoupling factor depends on the refractive index (RI) matching of the organic layers, the anode, and the substrate as well as the surface plasmon excitation related losses at the metal cathode [32]. An equation for η_{OUT} is given by,

$$\eta_{out} = 1 - \sqrt{1 - n^{-2}} \approx 1/(2n^2) \quad \text{..... 1.9}$$

where n is the effective refractive index of the organic stack. With RI of organics being ~ 1.7, only ~ 17-20% of the light generated inside can be extracted for a standard ITO/glass OLED.

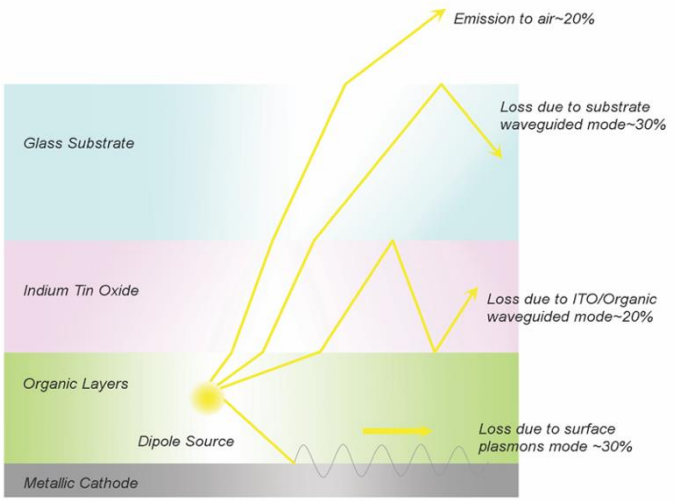

Figure 1.9: Schematic showing loss channels in OLED [35]

Various loss mechanisms within the OLED are shown in ***Figure 1.9*** and can be divided into:

I. Internal Losses

These losses ~ 50% arise within the active region of the OLED. Internal waveguiding that arises due to the difference in the refractive index of the anode and the organic layers as well as the surface plasmon excitations (SPPs) on the organic/metal interface are the two major ways for this category. Various approaches viz., corrugated substrate, Vacuum hole nanoarrays, sub anode metal grid, photonic crystal, bucking surface is used for addressing this issue [32, 36-39].

II. External Losses

This loss is due to the substrate/air interface and is ~30%. To mitigate this issue microlens arrays, half spherical lens is used on the substrate/air side [36,40].

The principal goal of DOE Solid state lighting program is to increase the efficiency to 70% by 2020 [41]. Major efforts are still underway both from the scientific as well as the industrial community for the mitigation of the loss mechanisms using internal as well as the external extraction means [32,34]. This dissertation explores one of the promising possibilities; using low cost patterned plastic substrates.

PART 2

1.5 Atomic Force Microscopy (AFM)

Atomic Force Microscope measures the force between scanning tip and sample to track the surface topography of the sample [42]. Lenard -Jones (L-J) potential as shown in ***Figure 1.10*** (a) is the model potential for the qualitative discussion of tip sample interaction. It comprises of two terms; Vander Waals interaction ($\propto {}^{1}/_{r^6}$) that describe the attractive part of the interaction dominant at the larger distances, and a strong repulsive interaction ($\propto {}^{1}/_{r^{12}}$) dominant in very short distances.

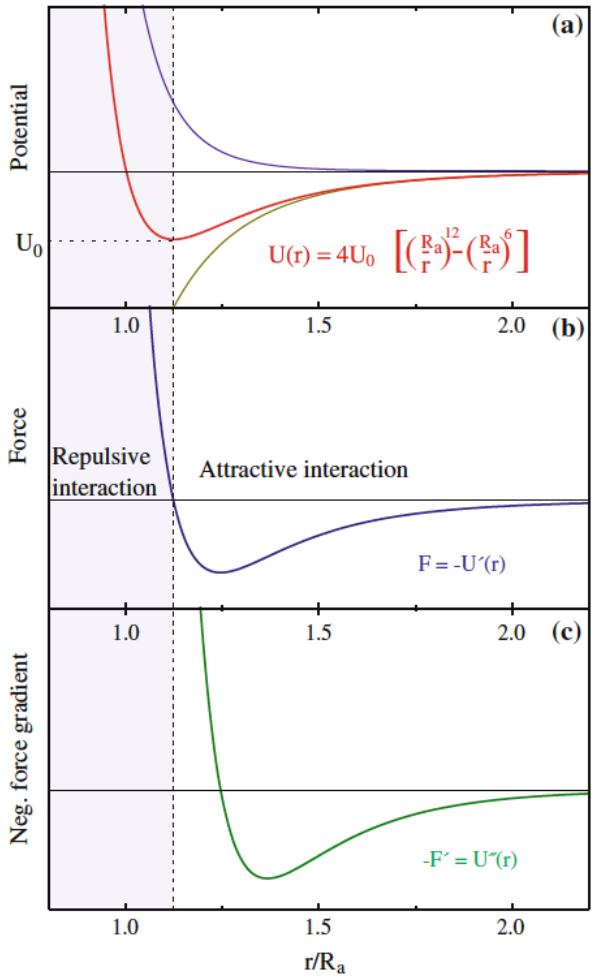

Figure 1.10: :(a) Lenard Jones (L-J) Potential, (b) Force, (c) Force gradient plot for tip sample interaction [43]

Mathematically,

$$U_{LJ}(r) = 4U_0[(\frac{R_a}{r})^{12} - (\frac{R_a}{r})^6] \quad \text{..... 1.10}$$

where U_0 is the depth of the potential well, r is the distance between the atoms and R_a is the depth at which $U_{LJ}(r)$ is zero. Both the force

$$\boldsymbol{F} = -\frac{dU}{dr} \quad \text{..... 1.11}$$

and its gradient

$$\nabla \boldsymbol{F} = -\frac{d^2U}{dr^2} \quad \text{..... 1.12}$$

are other important physical quantities important for AFM and are shown in ***Figure 1.10*** (b) & 10 (c) respectively [43].

Two most common modes used in AFM are (i) static mode and (ii) dynamic mode [44].

1.5.1 Snap to contact

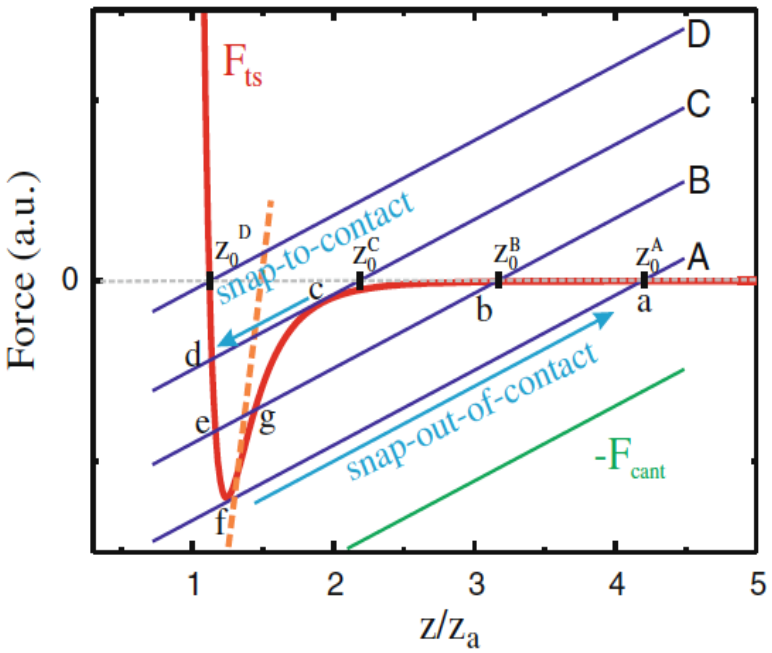

Figure 1.11: Force curve showing snap to/out of contact behavior of tip and sample surface [43]

Snap to contact as shown in ***Figure 1.11*** (blue arrow between c and d) means that tip is deliberately made to be in contact to the surface. This property is favored in the static mode as

opposed to the dynamic mode. In the static mode the cantilever is not oscillated but is always in constant contact of the surface.

In the dynamic mode the cantilever is excited to oscillate, and snap-to-contact is to be prevented at all cost since this would stop the oscillation of the cantilever. Two ways by which it can be prevented are (i) the stiffer cantilever (ii) large oscillation amplitude that enable cantilever force to overcome tip sample force [45].

1.5.2 Beam Deflection

The bending of the cantilever that quantify tip sample interaction is measured by the beam deflection method as shown in ***Figure 1.12***. The laser from the laser diode is focused on the backside of the cantilever and is reflected into the photodiode. The bending of the cantilever is detected by the split photodiode, i.e., two photodiodes separated by the small slit.

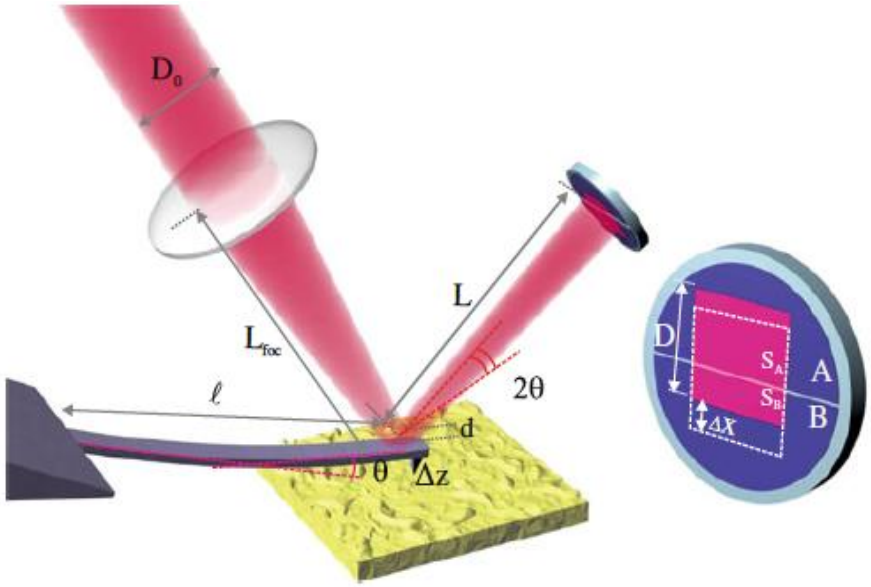

Figure 1.12: Beam deflection method used in AFM for cantilver bending[43]

The difference in the optical signals of the two parts of the split photodiode which is $(S_A - S_B)$ is proportional to the angular deflection of the laser beam and therefere proportional to the cantilever delection (bending). The absolute intensity detected by the photodiode can vary

due to fluctuations in the laser intensity and depending on the focusing of the laser beam onto the cantilever. In order to be independent of the absolute intensity of the signal the normalized intensity is used

$$(S_A - S_B)\Big/(S_A + S_B) \quad \text{..... 1.13}$$

The beam deflection method requires a mirror like surface on the back of the cantilever. Also, the cantilever should be large enough to reflect the light without too much diffraction. This is necessary since the diameter of the beam on the photodiode must be smaller than the active diameter of the photodiode. In this type of set up it is the sample that is scanned not the tip because when scanning the cantilever, the laser spot on the back of the cantilever is no longer focused on the cantilever [44].

1.5.3 Dynamic mode characteristics

The characteristics curve for the dynamic mode AFM is shown in ***Figure 1.13***. In this mode, the cantilever is excited using a piezo actuator which oscillate the cantilever base [46].

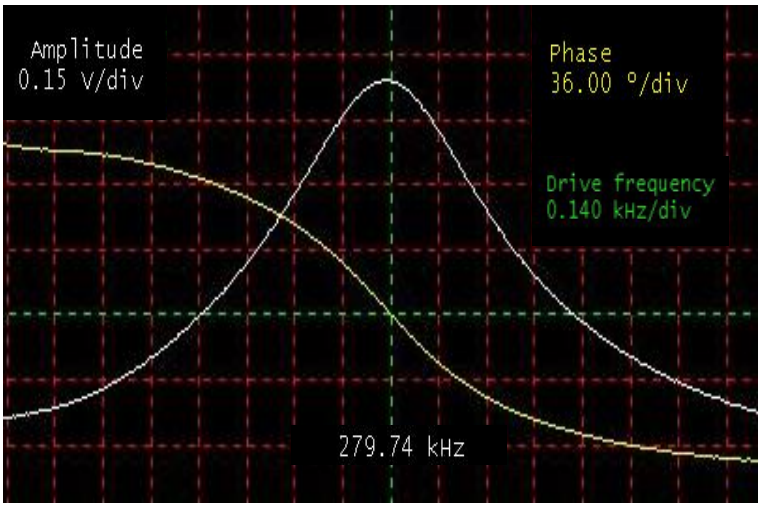

Figure 1.13: Amplitude/Phase curve showing resonance peak in Dynamic AFM

The driving frequency is very close to the resonance frequency of the cantilever. Due to the interaction between the tip and the surface, the resonance frequency of the cantilever changes. Compared to STM where two important parameters are the tunneling current and the tunneling voltage there are many parameters that are important for the dynamic mode AFM viz.,

1. The resonance frequency of the cantilever, ω_0
2. The force constant of the cantilever, k
3. The quality factor of the cantilever, Q_{cant}
4. The driving amplitude of the oscillation, A_{drive}
5. The oscillation Amplitude, A
6. The phase φ between driving and the oscillation
7. The driving frequency, ω_{drive}
8. The frequency shift of the resonance frequency $\Delta\omega$ relative to ω_0 due to tip sample interaction.

1.5.3.1 Opted qualities of Cantilever/Tip for Dynamic mode

AFM cantilever need to have (i) high resonance frequency (ii) small spring constant. Considering the basic equation of the harmonic oscillator.

$$\omega_{cant} = \sqrt{\frac{k}{m}} \quad \text{..... 1.14}$$

The small cantilever can possess both qualities (i) small spring constants (for high force sensitivity~ nanonewton). (ii) high resonance frequencies of the cantilever (fast scanning and good stability with respect to vibrations). High resonance frequency is imperative to immune AFM from external vibrations and hence usually the resonance frequencies are$\gg 10\ kHz$. Both characteristics are met by the Bruker TESPA-V_2 cantilever as shown by its characteristics depicted on ***Figure 1.14***.

(a)

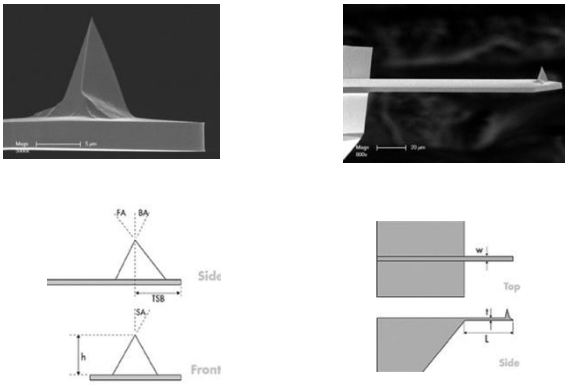

(b)

TESP-V2/TESPA-V2 Specifications

	Units	Target	Min	Max
Tip				
Shape	-	Pyramidal	-	-
Resistivity	Ω-cm	0.018	0.010	0.025
Tip Radius	nm	8.0	-	12.5
Tip Height, H	µm	12.5	10.0	15.0
Tip Set Back	µm	13.5	11.0	16.0
Tip Front Angle	deg	25.0	22.5	27.5
Tip Back Angle	deg	17.5	15.0	20.0
Tip Side Angle	deg	20.0	17.5	22.5
Cantilever				
Resistivity	Ω-cm	0.018	0.010	0.025
Shape	-	Rectangular	-	-
Cantilever Thickness	µm	3.4	2.65	4.15
Length (L)	µm	125	115	135
Width (W)	µm	40	38	42
Flexural Stiffness (k)	N/m	42	20	80
Flexural Resonant Frequency (f_o)	kHz	320	230	410
Body				
Material	-	Single Crystal Si	-	-
Type	-	Anisotropic Etch	-	-
Resistivity	Ω-cm	0.018	0.010	0.025
Dopant	-	Antimony	-	-
Thickness	µm	300	295	305
Backside Reflective Coating				
TESPA-V2 Material	-	Aluminum	-	-
Thickness	nm	40	30	50

Figure 1.14: (a) SEM images of the Cantilever and Tip along with its schematic. (b)Physical characteristics of the cantilever and Tip as provided by Bruker Co. for TESPA-V2 model. (cantilever of this model is used for the AFM work in this dissertation) [47]

1.5.3.2 Operating Principle

A scheme of dynamic mode AFM is shown below in ***Figure 1.15***. Oscillator generates the sinusoidal driving signal ω_{drive} which excites the piezoelectric actuator driving the cantilever base. As cantilevers have the resonance frequencies of several hundred kHz (in our case 320 kHz) the piezoelectric actuator requires even higher resonance frequency.

This often cannot be realized using a tube piezo element as it has too low resonance frequencies. The dither piezo element which is an additional piezo element with a high frequency is used for oscillating the cantilever base. As cantilever excites, it oscillates with much larger

amplitude of A as being close to the resonance, than the excitation amplitude. When tip and sample approach each other the oscillation amplitude at the fixed excitation frequency ω_{drive} will change due to a shift of the resonance frequency as induced by the tip-sample interaction. The deflection of the cantilever (sinusoidal signal) is measured as shown in ***Figure 1.15*** by the beam deflection method. Preamplifier electronics convert the signal from the split photodiode to the voltage signal proportional to the cantilever deflection. This signal is an AC signal at the frequency ω_{drive} with an amplitude proportional to the cantilever oscillation amplitude *A*. Lock-in-amplifier is employed to obtain the amplitude of the AC signal at frequency ω_{drive}. Driving signal acts as a reference signal for the lock-in-amplifier. A quasi-DC signal amplitude is obtained as the output of the lock in amplifier which is used as the input signal for the z-feedback controller. This amplitude is compared to the setpoint amplitude. The appropriate z_{signal} is determined by the controller for maintaining a constant oscillation amplitude. Maintaining a constant oscillation amplitude corresponds to the constant tip-sample distance. The z-feedback signal is the height signal mapping the topography during data acquisition.

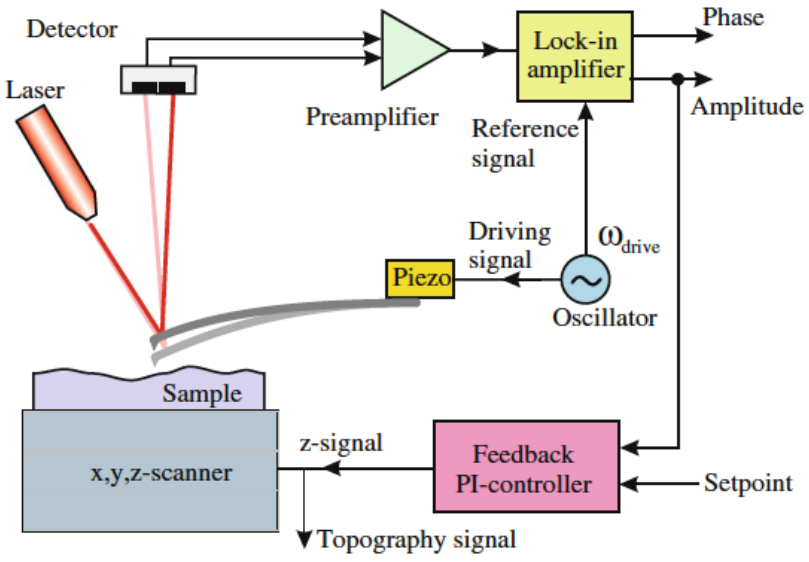

Figure 1.15: Schematic for the dynamic mode AFM [43]

1.5.3.3 Intermittent Contact /Tapping Mode

Intermittent/tapping mode force characteristics for the tip sample interaction is shown in ***Figure 1.16***. This mode is a type of dynamic mode where the tip is oscillated at much higher frequency to avoid any contact with the surface. The imaging is implemented in ambient air by oscillating the cantilever at or very near the cantilever resonance frequency at typical oscillation frequencies between 50 and 500 kHz.

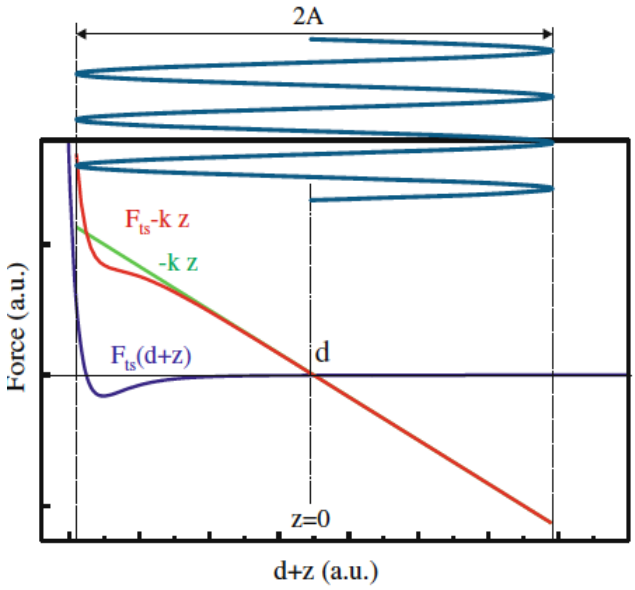

Figure 1.16: Force distance curve showing Intermittent/tapping mode characteristics [43]

Free amplitude in the range of 10-100 nm are used in this mode when the tip is not in contact with the surface. Force constants of the range of 10-50 N/m is usually used. The oscillation amplitude of the tip is measured by the detector and input to the controller electronics. The feedback loop then adjusts tip sample separation to maintain a constant set point amplitude for instance 80-90% of the free amplitude. In order to stabilize the oscillation in the net repulsive interaction regime (high amplitude branch), the driving frequency is often chosen below the resonance frequency of the free cantilever i.e. $\omega < \omega_0$.

In contrast to the contact mode, in the tapping mode no sidewise frictional forces are exerted on the sample minimizing the wear on the delicate samples.

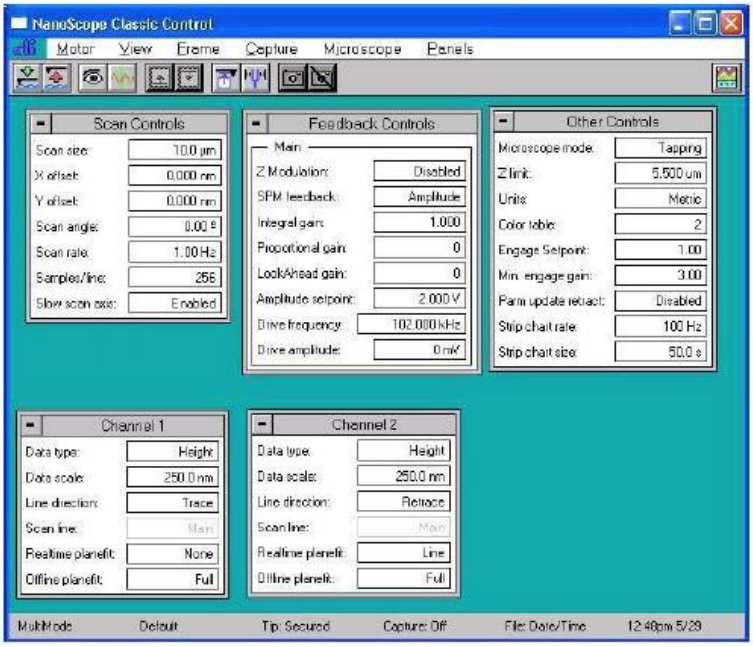

Figure 1.17: Nasoscope Interface for Tapping mode AFM [48]

1.5.3.4 Height/Phase Map

AFM in tapping mode generates Amplitude as well as the phase map as shown in ***Figure 1.18***. Amplitude image is more used in this dissertation for accessing;

1. Physical quantities/metric of substrate design primarily its height and period
2. Geometry (Concavity/Convexity) of the pattern
3. Homogeneity/Surface conformality

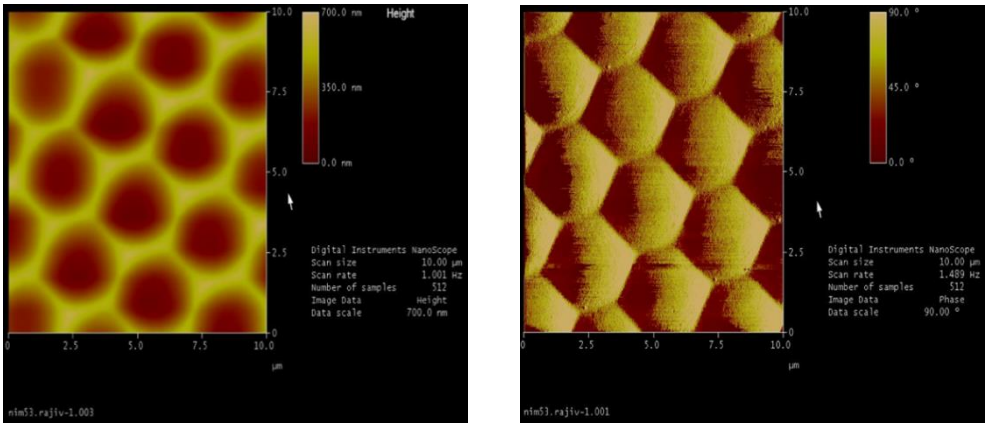

Figure 1.18: Height/Phase map for the same surface

1.6 Dissertation Organization

The ultimate goal of this dissertation is to demonstrate the feasibility of the patterned plastic OLED substrate for efficient light extraction. Achieving this goal requires systematic study of various substrate design and their subsequent characterization.

AFM as a characterization tool is proficient on providing both qualitative and quantitative information of the substrate that can be used advantageously for the optimal substrate design. This is the essence of the first two chapters of this dissertation. Chapter two, in particular, detail out the ongoing effort aimed on developing Integrated Plastic OLED substrate by the industrial partner, MicroContinuum Inc. in the project.

Chapter three undertakes more qualitative approach on understanding the phenomenal aspect of light extraction in the OLEDs as subjected to various design of the patterned plastic substrate.

Chapter four detail out the strong enhancement observed in the green phosphorescent OLED fabricated on the nanopatterned polycarbonate substrate.

Chapter five report on the strong enhancement of White phosphorescent OLED on the micropatterned PET substrate.

AFM as well as the OLED results of this dissertation have significant contributions on the following papers;

1. “Enhanced Light Extraction from OLEDs Fabricated on Patterned Plastic Substrates” published on 2018 on *Advanced Optical Materials, 6*(4), 1-11.

2. “Enhanced Light Outcoupling from OLEDs on Corrugated Plastic Substrates: Effect of Pattern Design”, manuscript in preparation to the submission.

1.7 References

[1] Bernanose, A., & Comte, M., Vouaux, P. (1953). *J. Chim. Phys,50* (64)

[2] Kallmann, H., Pope, M. (1960). *J. Chem. Phys, 32* (300)

[3] Partridge, R. (1983). *Polymer, 24* (733)

[4] Tang, C., & Vanslyke, S. (1987). Organic electroluminescent diodes. *Applied Physics Letters, 51*(12), 913-915.

[5] Burroughes, J.H., Bradley, D.D.C, Brown, A.R., Marks, R.N., MacKay, K., Friend, R.H., Burns, P.L., Holmes, A.B. (1990). *Nature, 347* (539)

[6] Gustafsson, G., Cao, Y., Treacy, G.M., Klavetter, F., Colaneri, N., Heeger, A.J. (1992). *Nature 357* (477)

[7] Kido, J., Hongawa, K., Okuyama, K., Nagai, K. (1994.) *Appl. Phys. Lett. 64* (815)

[8] Baldo, M.A., O'Brien, D.F., You, Y., Shoustikov, A., Sibley, S., Thompson, M.E., Forrest, S.R. (1998). *Nature 395* (151)

[9] http://pioneer.jp/en/info/globalnetwork/japan/tohokupioneer/mainbusinesses/oled/

[10] Sariciftci, N., & Namdas, E. (2010). *Semiconducting and metallic polymers / Alan J. Heeger, N. Serdar Sariciftci, Ebinazar B. Namdas.* (Oxford graduate texts). Oxford: Oxford University Press.

[11] https://ocw.mit.edu/courses/materials-science-and-engineering/3-091sc-introduction-to-solid-state-chemistry-fall-2010/bonding-and-molecules/10.-hybridized-molecular-orbitals-paramagnetism/MIT3_091SCF09_lec10.pdf

[12] Simon, Steven H., & Simon, Steven H. (2013). *The Oxford solid state basics / Steven H. Simon.* (First ed.). Oxford: Oxford University Press.

[13] Kalyani, N., Swart, H., & Dhoble, S. (2017). *Principles and applications of organic light emitting diodes (OLEDs) / N. Thejo Kalyani, Hendrik Swart, S.J. Dhoble.* (Woodhead Publishing series in electronic and optical materials).

[14] Kafafi, Z. (2005). *Organic electroluminescence / [edited by] Zakya Kafafi.* (Optical engineering (CRC Press) 94). Boca Raton, FL: CRC

[15] Miyata, S., & Nalwa, H. (1997). *Organic electroluminescent materials and devices / edited by Seizo Miyata and Hari Singh Nalwa.* Amsterdam: Gordon and Breach. Press, Taylor & Francis

[16] Sze, S., & Lee, M. (2012). *Semiconductor devices, physics and technology / S.M. Sze, M.K. Lee.* (3rd ed.). Hoboken, N.J.: Wiley.

[17] Taur, Y., & Ning, T. (2009). *Fundamentals of modern VLSI devices / Yuan Taur, Tak H. Ning.* (2nd ed.). Cambridge, UK; New York: Cambridge University Press.

[18] Geoghegan, M., & Hadziioannou, G. (2013). *Polymer electronics Mark Geoghegan and Georges Hadziioannou.* (Oxford master series in physics). Oxford, U.K.: Oxford University Press.

[19] Kohler, A. (2015). *Electronic processes in organic semiconductors: An introduction.* Weinheim: Wiley Vch.

[20] Locklin, J., & Bao, Zhenan. (2007). *Organic field-effect transistors / [edited by] Zhenan Bao, Jason Locklin.* (Optical science and engineering (CRC Press); 128). Boca Raton: CRC Press.

[21] Pope, M., & Swenberg, Charles E. (1999). *Electronic processes in organic crystals and polymers / Martin Pope, Charles E. Swenberg.* (2nd ed., Monographs on the physics and chemistry of materials 56). New York: Oxford University Press.

[22] Muccini, M., & Toffanin, S. (2016). *Organic light-emitting transistors: Towards the next generation display technology / Michele Muccini, Stefano Toffanin.*

[23] Koden, M. (2016). *OLED display and lighting / Mitsuhiro Koden.* (Wiley series in display technology).

[24] https://www.renishaw.com/en/photoluminescence-explained--25809

[25] Andrews, D. (2014). *Molecular photophysics and spectroscopy / David L. Andrews.* (IOP concise physics). San Rafael, CA: Morgan & Claypool.

[26] Valeur, B. (2002). *Molecular fluorescence: Principles and applications / Bernard Valeur.* Weinheim: Wiley-VCH.

[27] Browne, W., O'boyle, N., Mcgarvey, J., & Vos, J. (2005). Elucidating excited state electronic structure and intercomponent interactions in multicomponent and supramolecular systems. *Chemical Society Reviews*, *34*(8), 641-663.

[28] Förster, Th. (1959) *Transfer mechanisms of electronic excitation*. Discuss. Faraday Soc., *27*, 7 – 17.

[29] Dexter, D.L. (1953) *A theory of sensitized luminescence in solids*. J. Chem. Phys., *21*, 836 – 850.

[30] https://en.wikipedia.org/wiki/Photopic_vision

[31] Tsujimura, T. (2012). *OLED displays: Fundamentals and applications / Takatoshi Tsujimura.* (Wiley SID series in display technology). Hoboken, N.J.: Wiley.

[32] National Research Council. Committee on Assessment of Solid-State Lighting. *Assessment of Solid-state Lighting, Phase Two / Committee on Assessment of Solid-State Lighting, Phase 2, Board on Energy and Environmental Systems, Division on Engineering and Physical Sciences.* 2017.

[33] Hippola, Chamika, Kaudal, Rajiv, Manna, Eeshita, Xiao, Teng, Peer, Akshit, Biswas, Rana, Slafer, Warren Dennis, Trovato, Tom, Shinar, Joseph, and Shinar, Ruth. (2018). Enhanced Light Extraction from OLEDs Fabricated on Patterned Plastic Substrates. *Advanced Optical Materials, 6*(4), 1-11.

[34] National Research Council. Committee on Assessment of Solid-State Lighting. *Assessment of Solid-state Lighting, Phase Two / Committee on Assessment of Solid-State Lighting, Phase 1, Board on Energy and Environmental Systems, Division on Engineering and Physical Sciences.* 2013.

[35] Mann, V., & Rastogi, V. (2017). Dielectric nanoparticles for the enhancement of OLED light extraction efficiency. *Optics Communications, 387*, 202-207.

[36] Jeon, Sohee, Lee, Sunghun, Han, Kyung-Hoon, Shin, Hyun, Kim, Kwon-Hyeon, Jeong, Jun-Ho, & Kim, Jang-Joo. (2018). High-Quality White OLEDs with Comparable Efficiencies to LEDs. *Advanced Optical Materials, 6*(8), 1-8.

[37] Qu, Y., Coburn, C., Fan, D., & Forrest, S. (2017). Elimination of Plasmon Losses and Enhanced Light Extraction of Top-Emitting Organic Light-Emitting Devices Using a Reflective Subelectrode Grid. *ACS Photonics, 4*(2), 363-368.

[38] Ishihara, K., Fujita, Matsubara, Asano, Noda, Ohata, Hirasawa, Nakada, and Shimoji. (2007). Organic light-emitting diodes with photonic crystals on glass substrate fabricated by nanoimprint lithography. *Applied Physics Letters, 90*(11), Applied Physics Letters, 12 March 2007, Vol.90(11).

[39] Koo, W., Jeong, S., Araoka, F., Ishikawa, K., Nishimura, S., Toyooka, T., & Takezoe, H. (2010). Light extraction from organic light-emitting diodes enhanced by spontaneously formed buckles. *Nature Photonics, 4*(4), 222-226.

[40] Park, Jm, Gan, Zq, Leung, Wy, Liu, R, Ye, Z, Constant, K, Shinar, J, Shinar, R, and Ho, Km. (2011). Soft holographic interference lithography microlens for enhanced organic light emitting diode light extraction. *Optics Express, 19*(14), A786-A792.

[41] US Department of Energy 2018 *Solid-State Lighting R&D Opportunities* 2019, Sec. 6.2, p. 52.

[42] Sarid, D. (1994). *Scanning force microscopy: With applications to electric, magnetic, and atomic forces / Dror Sarid.* (Rev. ed., Oxford series in optical and imaging sciences 5). New York: Oxford University Press.

[43] Voigtländer, B. (2015). *Scanning Probe Microscopy Atomic Force Microscopy and Scanning Tunneling Microscopy / by Bert Voigtländer.* (1st ed. 2015. ed., NanoScience and Technology).

[44] Placidi, E. (2017). *Introduction to atomic force microscopy / Ernesto Placidi.*

[45] Castro García, R. (2010). *Amplitude modulation atomic force microscopy / by Ricardo García.* Weinheim: Chichester: Wiley-VCH; John Wiley

[46] Haugstad Greg, (2012). *Atomic Force Microscopy: Understanding Basic Modes and Advanced Applications,* John Wiley & Sons, Inc.

[47] https://www.brukerafmprobes.com/images/product/specPDF/3844.pdf

[48] MultiMode SPM Instruction Manual, NanoScope Software Version 5

CHAPTER 2. PROBING INTEGRATED PLASTIC OLED SUBSTRATES USING TAPPING MODE ATOMIC FORCE MICROSCOPY

2.1 Abstract

Integrated Plastic OLED substrates include nanoarrays/microarrays with ITO anode as a transparent field conductor, metal mesh as an accessory field conductor and a microlens array on the back side of the substrate along with a barrier coating against penetration of oxygen and moisture. These substrates incorporate both “internal” and “external” light extraction means for recovering photons from “internal” waveguiding in the high refractive index organics+ ITO, minimizing photon loss due to surface plasmon excitation at the metal cathode, as well as “externally” waveguided photons in the substrate respectively. MicroContinuum Inc., is an industrial partner, in this ongoing project with expertise in fabrication of low-cost substrates. Understanding the design aspects of each substrate component and establishing a metric for it is the first step toward the successful implementation of this approach. This study, via intermittent contact mode atomic force microscopy (AFM), carefully lays out the quantitative aspects of integrated plastic OLED substrates.

2.2 Introduction

Organic electronics devices, in particular OLEDs, are already a mature technology in display applications underpinning daily lives (in mobile phone displays and TVs) due to their inherent attributes such as color quality as well as their lightweight, portability, and flexibility [1-3]. In addition to display, OLEDs are being developed for solid state lighting and sensing applications, with increasing interests in flexible organic devices for medical applications [4-6].

Flexible OLEDs on flexible plastic substrates have several advantages over standard glass substrates. Plastic substrates are amenable to roll-to-roll (R2R) fabrication as shown in ***Figure 2.1*** and are consequently very cost effective [7]. Moreover, some low-cost plastic substrates, such as Polycarbonate (PC), have a relatively high refractive index e.g., $n_{PC} \approx 1.6$ and thus can serve as a promising transparent substrate for enhancing light extraction from OLEDs in lighting and display products.

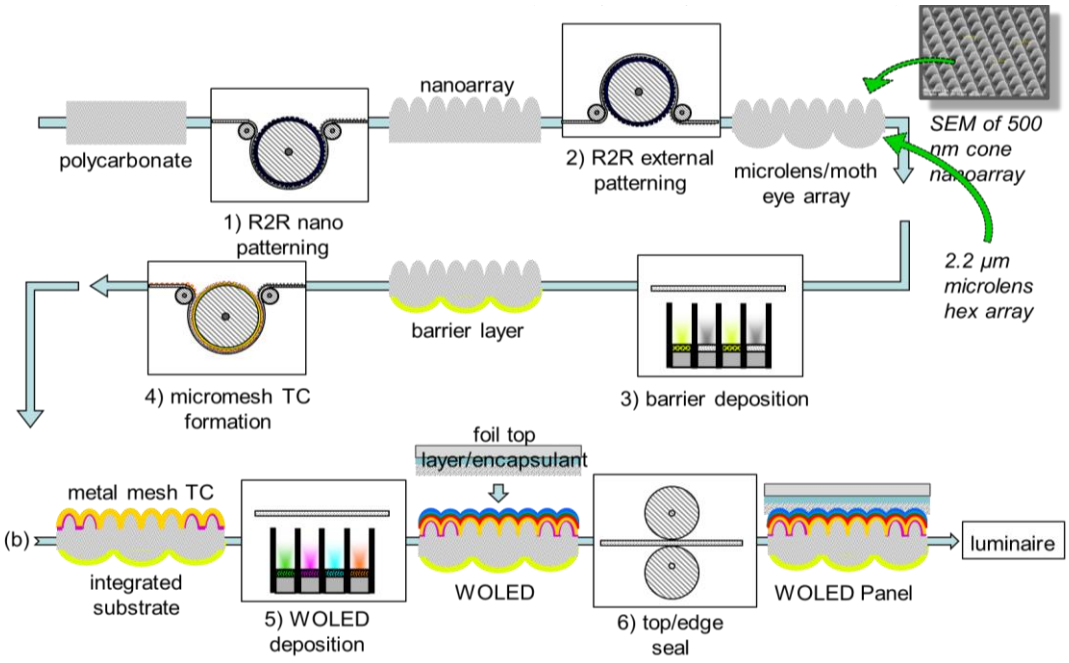

Figure 2.1: Schematic of R2R manufacturing of integrated plastic substrates and OLEDs

MicroContinuum Inc., an industrial partner on the project, has been developing the integrated plastic OLED substrates as shown in ***Figure 2.2*** (with designs that are based on the team's theoretical calculations) that encompass 1. Top Nano/Microarrays, 2. ITO as a primary field conductor, 3. Thin Cu mesh as an auxiliary field conductor, 4. Microlens Array on the backside of the OLED substrate, and 5. Barrier layer [8]. The top nano- or microarrays (on which the OLEDs are fabricated)-assist in recovering the photons lost to internal waveguiding, and in mitigating surface plasmon excitation-related loss [9]. The-microlens array at the air-side of the

substrate extracts the light trapped in the substrate, while the barrier layer prevents oxygen and moisture from penetrating the OLED [10,11].

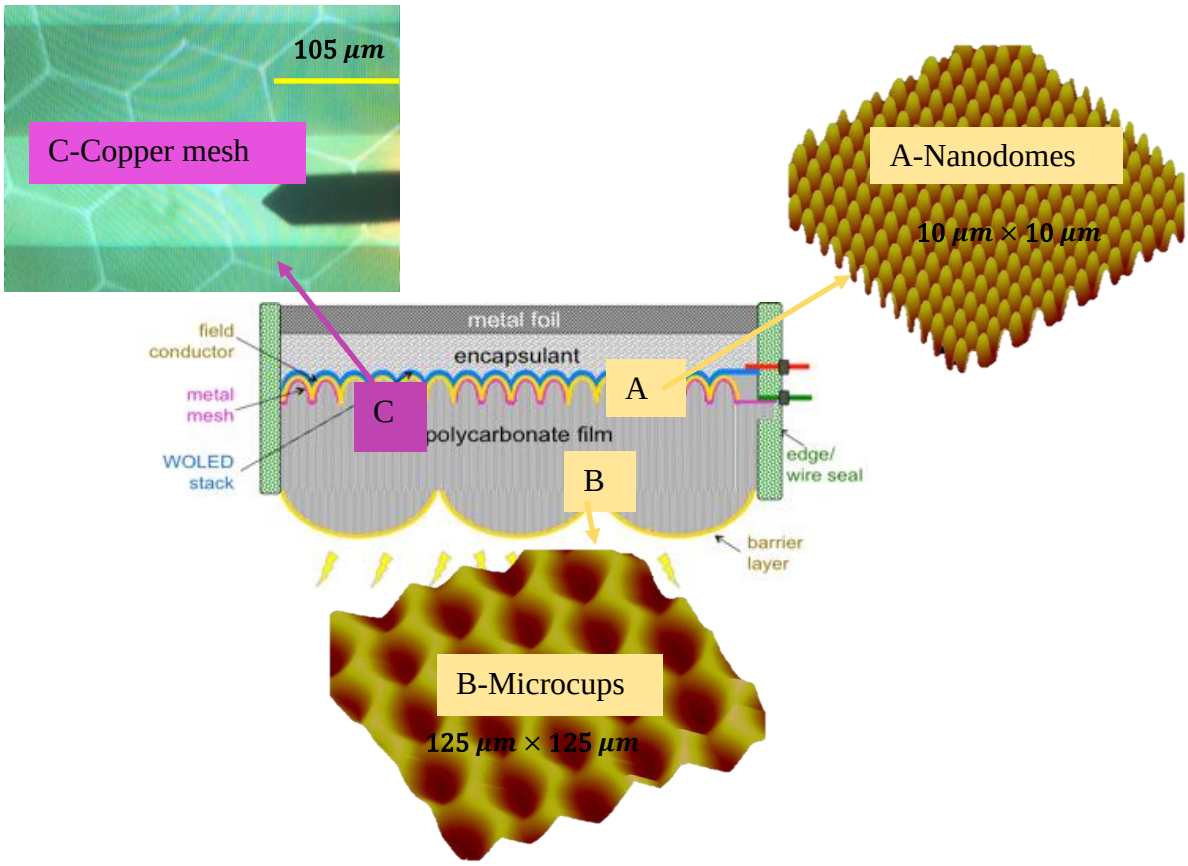

Figure 2.2: Schematic of an OLED on Integrated Plastic Substrate

The quantitative characterization of each component of the integrated plastic OLED substrate is imperative for successful optimization of the overall substrate design. Imaging techniques, like AFM, SEM, and optical microscopy, can assist in achieving such goal [12]. Some of the important parameters to consider in characterizing the substrates are the structural features (height and pitch, convex or concave, periodic or aperiodic), structure smoothness (that has to be devoid of sharp edges), as well as ease of sample preparation and handling reproducibility, stability & delamination in multi-layer structures, impurities). Other important parameters include conductivity and identification of structures that can result in shorts.

Atomic Force Microscopy (AFM) in its intermittent contact mode is one of the optimal probing techniques for soft polymer samples [13]. As constant contact between the probe and the sample is avoided in this mode, the underlying surface morphology remains intact [14]. As plastic samples are both insulating and of low melting temperature, SEM is not optimal for imaging these types of samples [15]**.** In addition**,** SEM requires a conducting coating, which may modify and possibly damage the underlying surface [15]. Also, in SEM it is common practice to tilt the sample with respect to the incident electron probe for proper image acquisition [15]**.** Thus, extraction of attributes like feature height, period, and step at interfaces requires information of the tilt angle [15]. This however is eliminated in the AFM where the sample remains horizontal with respect to the cantilever thus avoiding the necessity of tilt angle.

2.3 Results and Discussions

In this chapter the results are presented in the order of the complexity of the design. Planar plastic as well as the aperiodic surface on Silicon is characterized first, with surface roughness as their metric. Next, patterned plastic substrates of two kinds; PC and PET/CAB are investigated establishing corrugation height, period as their metric. ITO on some of these patterned substrates are tabulated next. Two specific examples and transfer ITO method are provided as an ongoing effort for the development of ITO on patterned plastic substrates. Cu mesh both buried and proud (with and without ITO) on planar as well as ITO on corrugated PET succeeds next. Microlens array as well as barrier coating layer are discussed on the end.

2.3.1 Planar/Non planar (Aperiodic) Plastic OLED Substrates

OLED on planar substrates as shown in ***Figure 2.3*** are used as reference/control OLED. LCC, MOBAY, BAYER, TORAY and ZEONOR refers to different vendors/sources of plastic. LCC PC is 330 µm thick with acrylic hard coat on backside. MOBAY PC from MOBAY corp. is

380 µm thick, TORAY PC from TORAY Plastics (Japan) is 360 µm thick. ZEONOR is a cyclic olefin polymer film (100 µm thick) made by Zeon Chemicals (Japan) [16,17]. BAYER PC is from BAYER company and is 375 µm thick PC film [18].

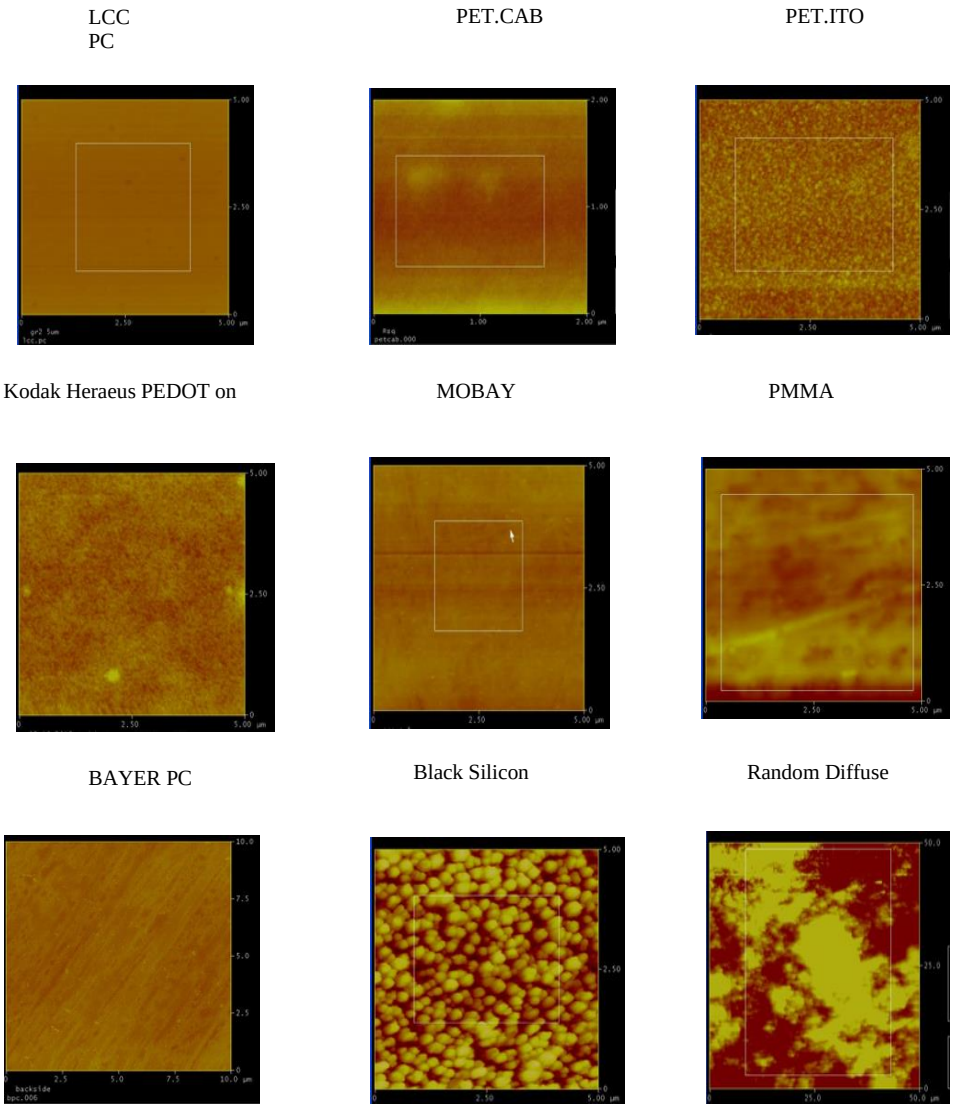

Figure 2.3: AFM images of representative planar/nonplanar substrate

Polyethylene terephthalate/ Cellulose acetate butyrate (PET/CAB) is a two-layer film with a 12 µm cellulose acetate butyrate on 75 µm thick polyester (PET=Mylar ©) film [19]. PC and PET/CAB differs on (i) *Thickness*: PC substrate is thicker than PET and hence is less

susceptible to oxygen and moisture. (ii) *Softening point of CAB layer*: CAB layer on the PET has a softening point (~ 90 ℃) and hence cannot be exposed to higher temperature [20].

Black silicon and Random diffuse, shown respectively as the last two samples on ***Figure 2.3*** are the aperiodic structure made by wet etching of silicon and have a very rough surface [21]. The roughness of all these substrates are given in ***Table 2.1.***

Table 2.1: Roughness of various planar/nonplanar substrates

Plastic Type	*Surface*	*Root mean square Roughness (nm)*
LCC-PC	Flat	~1.6
PET/CAB	”	~1.9
PET/ITO	’’	~ 2.4
Kodak Heraeus PEDOT on PET	”	~ 2.4
MOBAY PC	”	~3.0
PMMA	”	~ 4.1
BAYER PC	”	~ 5.0
Black Silicon	Random pattern	~ 45.0
Random Diffuse	”	~74.0

2.3.2 Micro/Nanopatterned Polycarbonate (PC) Substrates

Patterning on PC as well as PET/CAB is done by pressing the template with the (reverse) pattern on the surface of these films by a proprietary process. NREL: National Renewable Energy Laboratory, NILT: “NIL” Technologies, SAIC are the places where the patterns were originally developed.

As shown in ***Figure 2.4***, NREL, SAIC and Motheye are hexagonal pattern whereas NILT is a square pattern. The height and the period of these patterns are tabulated on ***Table 2.2***. The height of these patterns depends on the pressure exerted during patterning. Two variants of height; Tall and Shallow are characterized for NREL, NILT and SAIC.

Table 2.2: Attributes of patterned PC substrates

Pattern	*Period (nm)*	*Height (nm)*
Moth eye	~ 300	~ 100
NREL LCC (convex & concave)	~750	~ 200-400
NREL-ZEONOR	~750	~65
NILT (convex & concave)	~ 400	~ 100-300
SAIC LCC & PMMA (convex & concave)	~ 250-4000	~ 1000

SAIC, NREL and NILT have both concave as well as convex version as shown in ***Figure 2.4.***

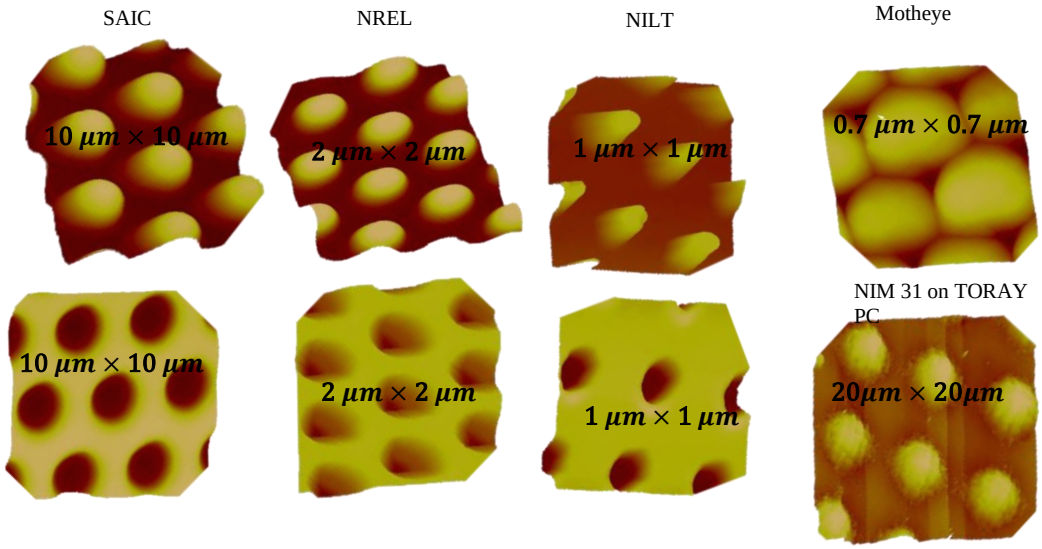

Figure 2.4: AFM images of patterned PC substrates.

2.3.3 Micropatterned PET/CAB Substrates

PET/CAB substrates also called as NIM "X" substrates as shown in ***Figure 2.5*** are exclusively concave in design. NIM stands for "**Ni**ckel **M**aster" which is used as a stamping tool for pattern generation [22]. The period of these pattern ranges from the micron to tens of micron and its shape being either hexagonal, square or linear. The corrugation attributes of the pattern of this category is tabulated on ***Table 2.3.***

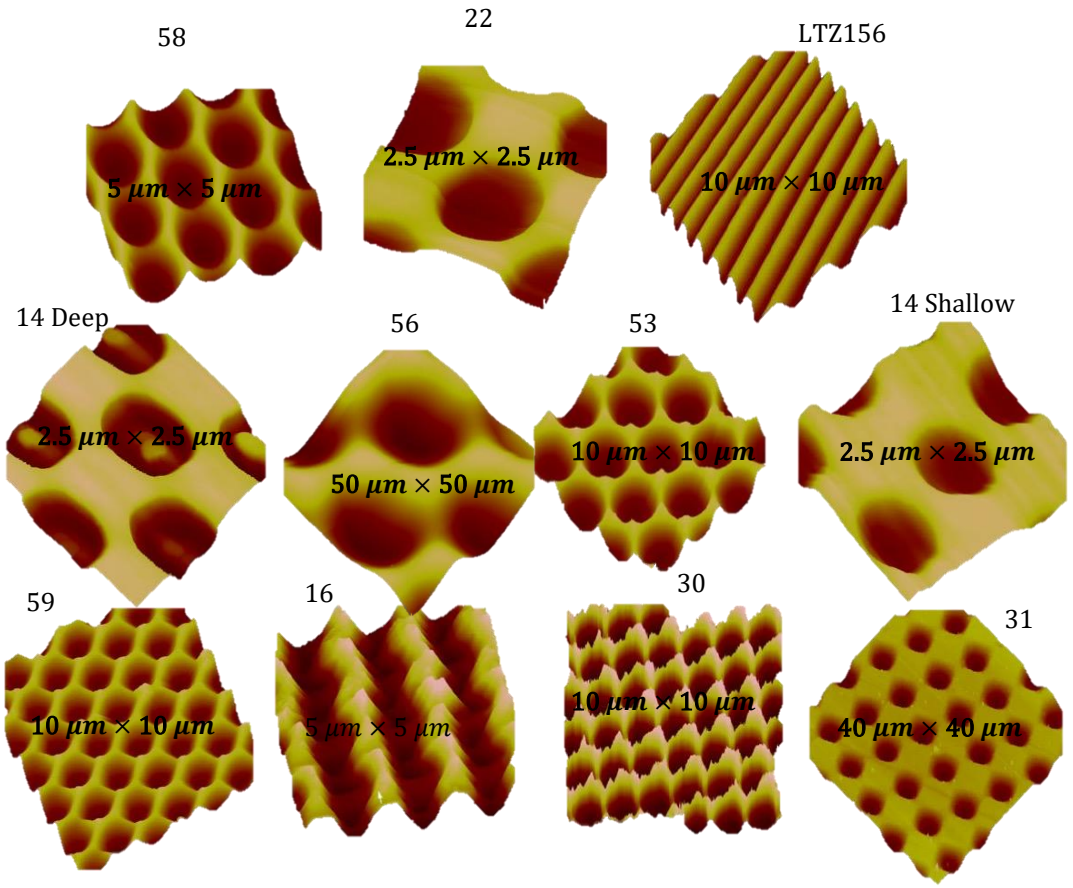

Figure 2.5: AFM images of patterned PET/CAB substrates

Table 2.3: Attributes of patterned PET/CAB substrates

Pattern	*Height (nm)*	*Period (μm)*	*Geometry*
NIM 14 - Deep Gaussian	~ 500	1.5	Square
NIM 14 -Shallow Gaussian	~ 324	1.5	Square
NIM 16	~586	1.5	1-D Grating
NIM 30	~696	1.5	Hexagonal
NIM 31	~ 320	7.8	Square
NIM 53	~500	3.0	Hexagonal
NIM 56	~1300	28	Hexagonal
NIM 22	~ 624	1.4	Square
NIM 58	~246	1.7	Hexagonal
NIM 59	~454	1.7	Hexagonal
UV on PET (LTZ156B)	~ 510	1.0	1-D Grating

2.3.4 Indium Tin Oxide on Patterned Plastic Substrates

ITO is commonly used as an anode for OLEDs. The reasons are its transparency over the visible range and its higher work function required for hole injection [23]. As a layer it can also be sputtered directly over the substrate. This provide better control over its thickness which is crucial for the patterned substrate to preserve surface conformality. The higher sputtering temperature that results on crystalline ITO is critical for its better quality [24]. MCI however uses RF sputtering method at room temperature for ITO sputtering [25]. The lower melting temperature of the plastic substrate impede MCI from sputtering at higher temperature. The goal of this section is twofold; first to establish the quantitative merit of the ITO on patterned substrates and then to explore some of the approaches developed by MCI on producing better ITO surface.

2.3.4.1 Patterned Substrates with ITO

The corrugation attributes of the ITO coated substrate of both PC and PET/CAB is provided below on ***Table 2.4***. The general observation is that with wider period substrate height/depth is retained as to its bare substrate.

Table 2.4: Attributes of ITO on patterned PC or PET/CAB substrates

ITO on PC/PET.CAB	*Height (nm)*	*Period (μm)*
NIM 58	~220	~1.80
NIM 31	~ 335	~ 8.10
NIM 59	~ 500	~ 1.87
NIM 14	~ 180	~ 1.24
NILT Convex)	~ 142	~ 0.41
NILT (Concave)	~162	~0.46
NREL (Convex)	~175	~0.72
SAIC (Concave)	~ 300	~ 4.00
Dual Corrugation NILT Pits on SAIC-1	~ 50	~0.38

Three ITO coated substrates on PET/CAB is shown in ***Figure 2.6***. ITO sputtered on NIM 31 which is square array is more optimal than hexagonal array in NIM 58 and NIM 59 for OLED stacking.

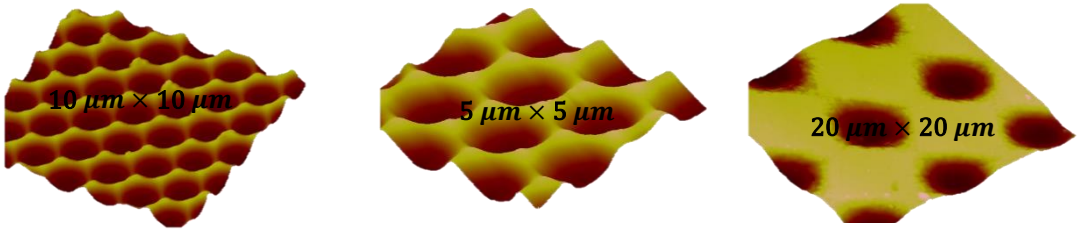

Figure 2.6: AFM images of ITO on patterned PET/CAB substrates

ITO sputtered on narrower period PET/CAB substrates have sharp edges (see NIM 58 and NIM 59) as compared to the wider period substrates (NIM 31). Thus, ITO layer on the wider period structure are smoother and have fewer sharp features.

2.3.4.2 ITO/NOA on patterned surfaces

MCI is currently investigating on different possibilities of incorporating ITO on structure that are more compatible for the OLED light extraction. Two major efforts are elucidated below

I. Norland Optical Adhesive (NOA) coated over ITO on SAIC-1 Pattern

NOA 170 is a yellow tinted liquid adhesive with a refractive index of 1.70 that will cure to a clear film when exposed to long wave ultraviolet and/or visible light wavelength [26]. Due to its high refractive index it is used along with the OLED substrate like glass for the substrate mode extraction [27]. This and following section describe MCI's effort on incorporating this layer in the patterned plastic substrate.

Figure 2.7 show an interface with A: ITO on SAIC-1 pattern and B: NOA coated over ITO on SAIC pattern as on the optical microscope. The green arrow represents the interface between these regions.

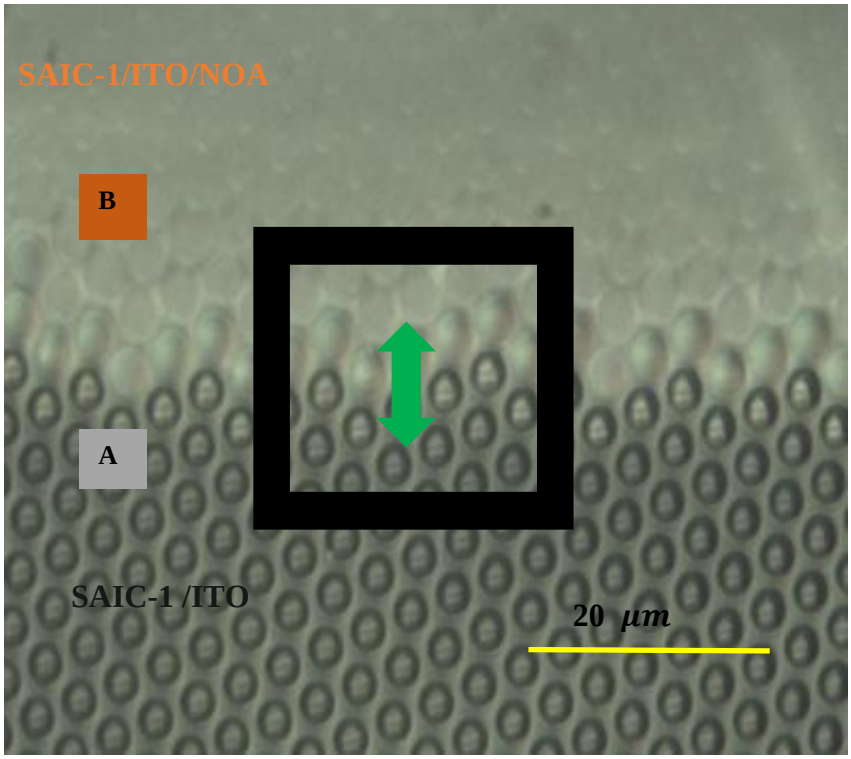

Figure 2.7: Optical Microscope image of SAIC-1/ITO (Region A) and SAIC-1/ITO/NOA (Region B) and their interface highlighted [8].

The AFM image in ***Figure 2.8*** is much more magnified image for the same interface. The profile infers on the rate of the change of the surface while traversing from region A to region B. As shown in the surface profile the region A is concave pit structure of SAIC-1/ITO pattern. The profile dampens as it gets closer to the interface of the SAIC-1/ITO/NOA region.

Figure 2.9 elaborate more on this with the separate surface profile for two regions along with the interface. The interface is of step height of ~ 400 nm that infers on thick NOA layer. Region A, i.e., SAIC-1/ITO is smooth with ~ 800 nm height and ~ 4 μm period. Region B that has NOA on top shows fissures/cracks. It could be due to the melting of NOA in the process of curing. The feature height of ~ 300 nm with similar period is measured for this region.

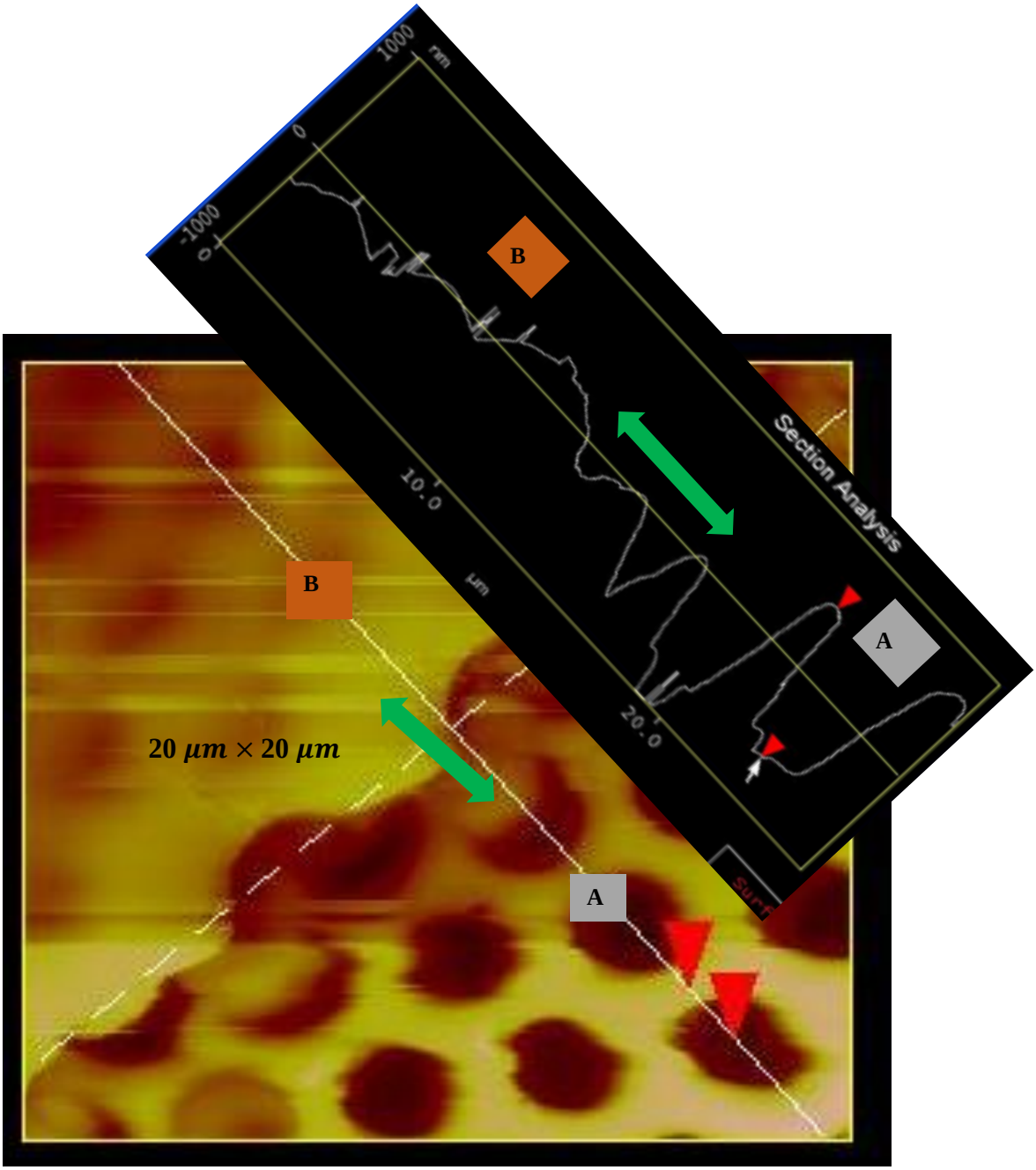

Figure 2.8: AFM image of the SAIC-1/ITO and SAIC-1/ITO/NOA interface with the surface profile

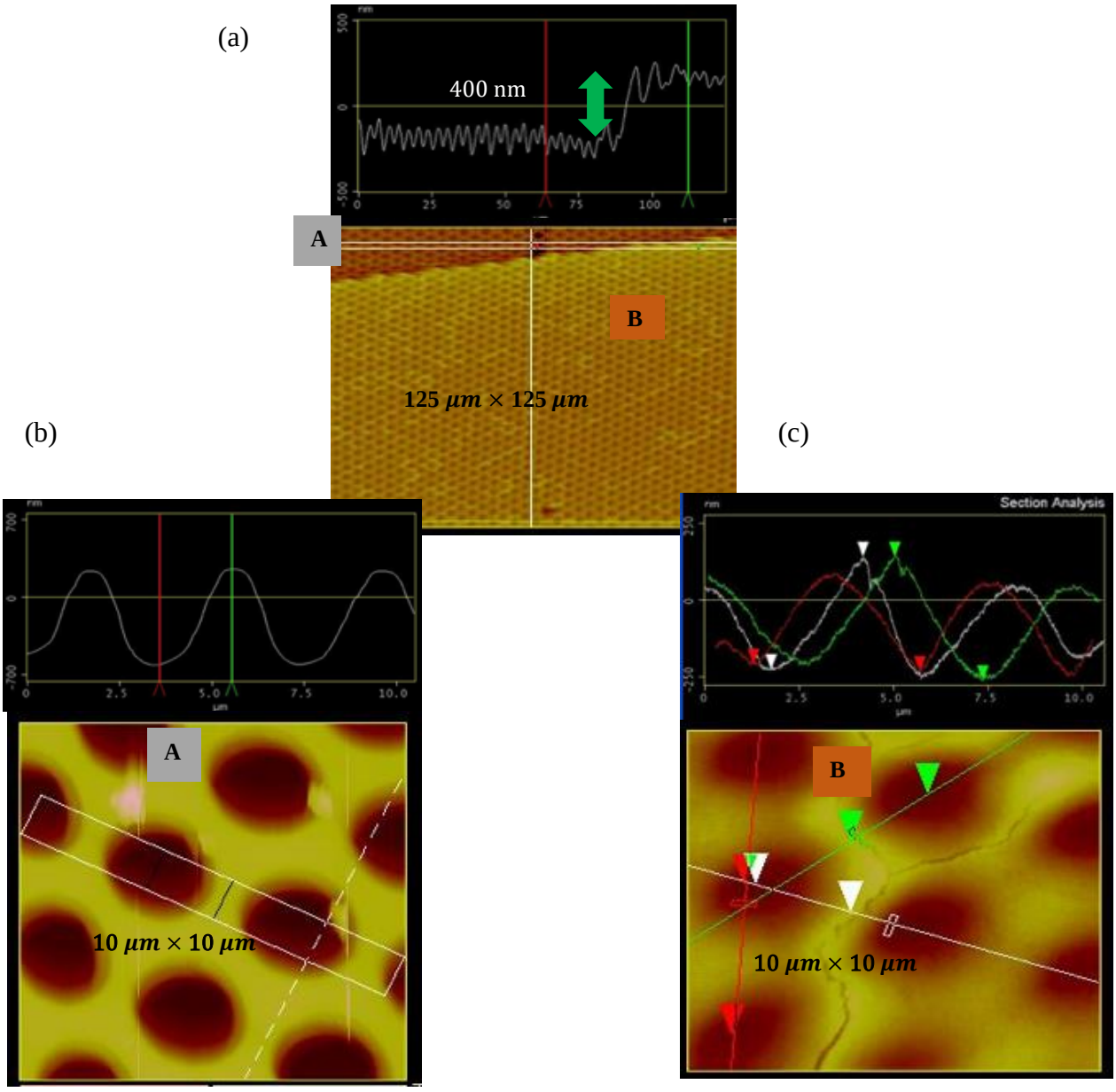

Figure 2.9: (a) Interface between SAIC/ITO and SAIC/ITO/NOA showing step height of 400 nm, (b) Profile of SAIC/ITO and (c) Profile of SAIC/ITO/NOA (cracks are visible).

II. Dual Corrugation

The schematic of dual corrugated structure is shown in ***Figure 2.10 (a).*** Incorporating top corrugation over the NOA layer is the additional attribute for this structure compared to the one described above. As shown in ***Figure 2.10 (b)***, NILT pattern laid over the NOA layer is the top

corrugation whereas ITO on SAIC-1 pattern is the bottom corrugation. The puffy surface on the top is indicative of the uneven NOA surface.

(a) (b)

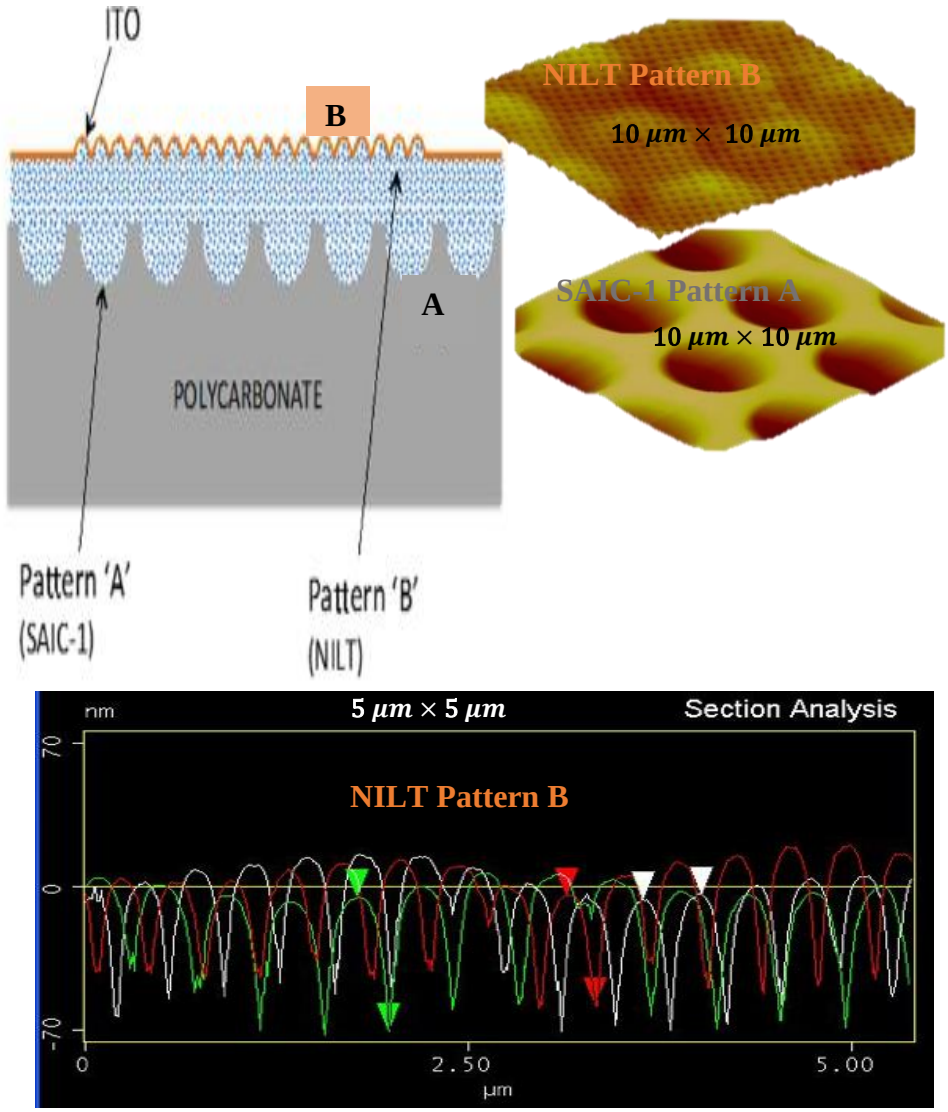

Figure 2.10: (a) Schematic for the dual corrugation, (b) AFM images for the NILT pattern(top) and SAIC-1 pattern (bottom) and (c) Section profile for NILT pattern (h~50nm; a~380 nm).

It is clear from ***Figure 2.10 (b)*** that the patches of NILT is superimposed on 4 μm pits of the SAIC-1 pattern. Green, white and red curve of the NILT pattern (*h~50nm; a~380 nm)* on ***Figure 2.10 (c)*** also infer to uneven surface.

2.3.5 Transfer ITO (Planar and Patterned PET

Smooth ITO surface is necessary as a better anode layer for OLED [28]. Schematic in ***Figure 2.11*** is the MCI's concept on producing smoother ITO using transfer method. Some of the initial results on such attempt is shown below:

I. Planar Reticulated PET

RMS Roughness measured of the transfer ITO on planar PET substrate is summarized in ***Table 2.5***. The values indicate that the surface is rough.

Figure 2.12 show the surface of $(5\ \mu m\ \times\ 5\ \mu m)$ scan with its roughness highlighted.

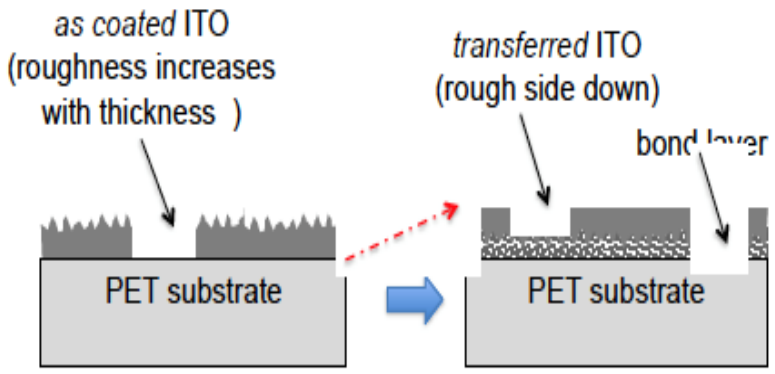

Figure 2.11: Schematic for Transfer ITO on PET

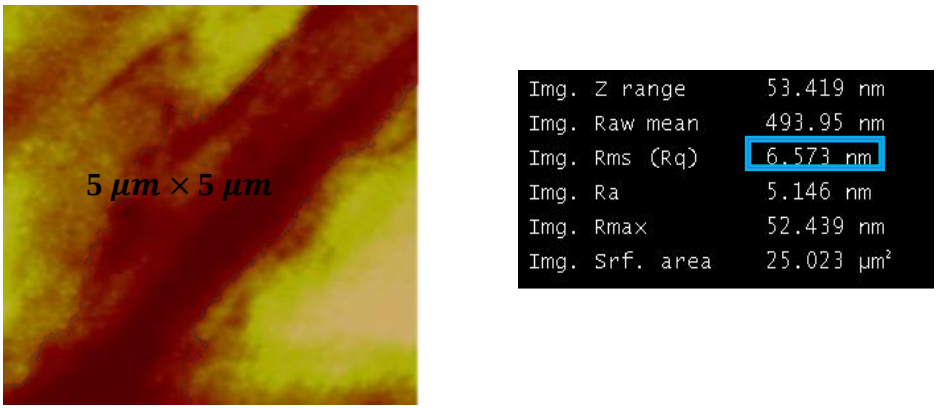

Figure 2.12: Planar ITO surface on PET $(5\ \mu m\ \times\ 5\ \mu m)$ *and its roughness highlighted.*

Table 2.5: RMS Roughness of planar reticulated PET

Scan Area *(μm × μm)*	*Root Mean Square Roughness (nm)*
2	~ 7.9
5	~ 6.6
10	~ 8.1

II. Patterned Reticulated PET

Similarly transfer ITO on the pattern surface is also indicative of non-smooth surface. The two different samples of transfer ITO on NILT pattern as shown in ***Figure 2.13*** shows highly uneven surface ~ 150 nm step.

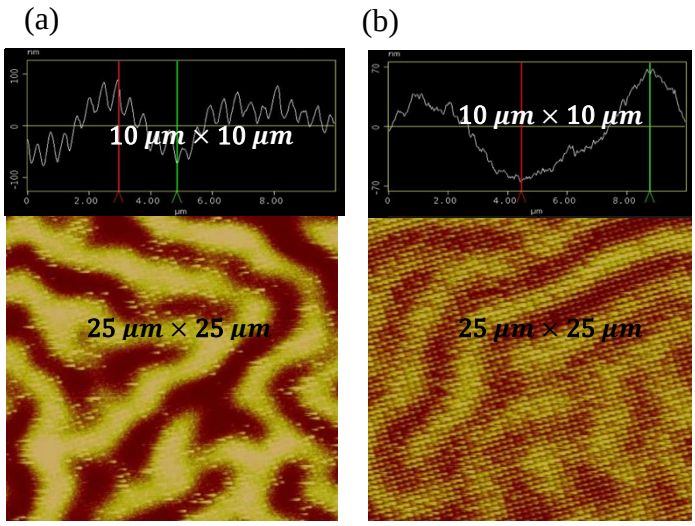

Figure 2.13: (a) NILT Pits with transfer ITO surface (and the profile of the same surface on top) and (b) NILT Bumps with transfer ITO surface (along with its surface profile on top).

2.3.6 Cu mesh on Planar PET with and without ITO

Cu mesh on addition to the ITO enhances the anode conductivity that improves hole injection [29]. Two different type of Cu mesh (Proud and Buried) as shown in schematic on ***Figure 2.14*** are summarized below. Proud and buried mesh differs on the protrusion of the Cu structure over the surface. Proud structure is above the substrate surface whereas the buried surface is beneath the surface. Step height as a metric indicate degree of protrusion over the surface.

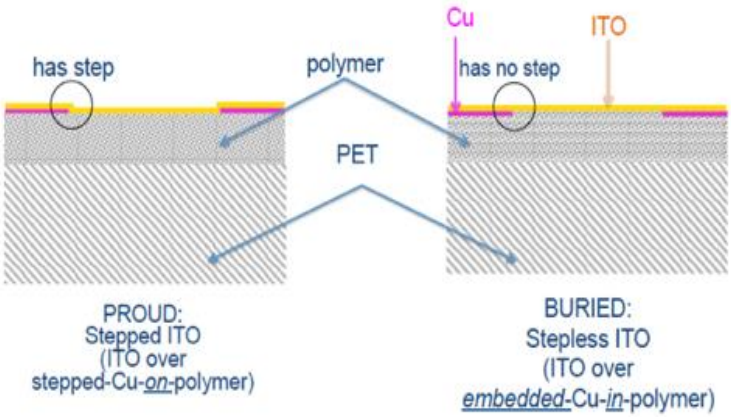

Figure 2.14: Schematic for Buried vs Proud Cu mesh on PET.

I. Proud Mesh

Step height of Cu mesh (Thick or thin) with or without ITO on PET substrate as quantified in ***Table 2.6*** is shown in ***Figure 2.15***. Approximately 100 nm step for each substrate type indicates that the OLED stacked on such structure is prone to shorts due to larger step. Reducing step size favoring OLED stacking to make it less susceptible to shorts is the next approach.

Table 2.6: Step height of Cu mesh with/without ITO on PET

Cu mesh (width)	*Step height of Cu mesh on planar PET*	
	ITO (nm)	*Without ITO (nm)*
Thick (34 μm)	70	120
Thin (7 μm)	95	115

The effort made on the reduction of the Cu mesh height/protrusion is provided on ***Figure 2.16.*** The step height is reduced to ~ 40 nm. The width and the length of the Cu mesh for this sample is ~ 4 μm and 65 μm respectively.

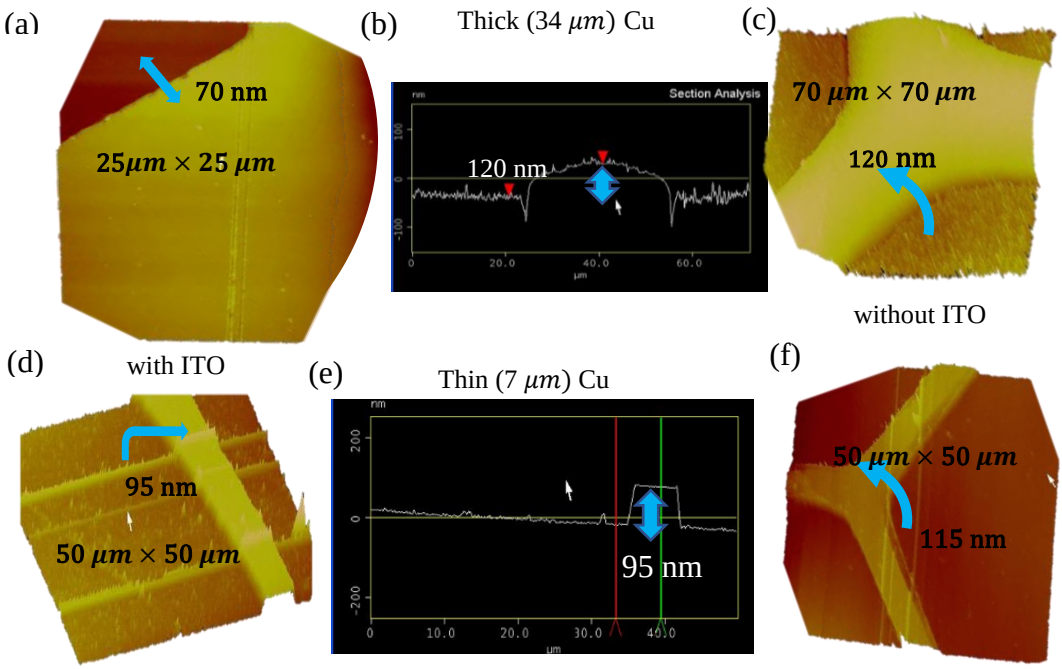

Figure 2.15: Planar PET substrate with (a) Thick Cu mesh with ITO, (b) Step height for thick Cu mesh without ITO, (c) Thick Cu mesh without ITO, (d) Thin Cu mesh with ITO, (e) Step height for thin Cu mesh without ITO and (f) Thin Cu mesh without ITO.

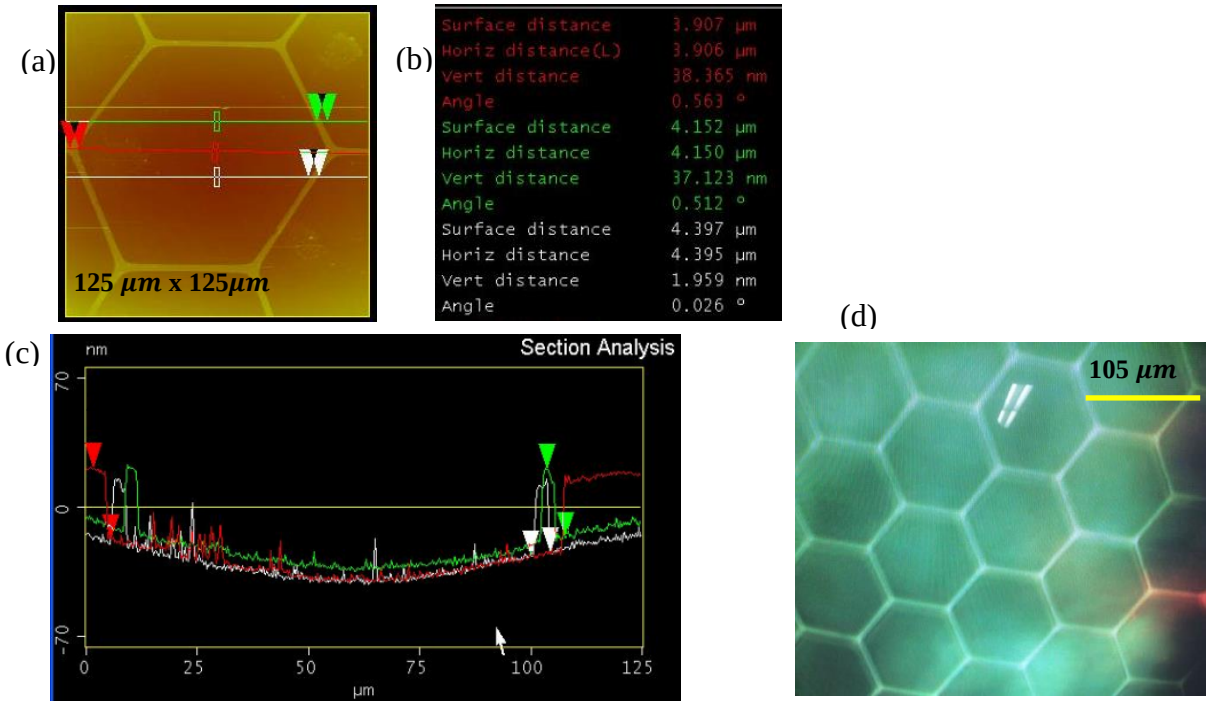

Figure 2.16: Cu mesh on PET (125μm × 125 μm) (a) AFM image, (b) Height/width of mesh, (c) Surface profile and (d) Optical Microscope image of the thin Cu mesh on PET. Red spot is the laser spot from AFM.

II. Buried Mesh

MCI approach of buried mesh is more favorable for OLED stacking. This structure being planar is nonintrusive and thus produces less shorts. AFM probed on this sample is indicative of planar surface ~ 10 nm rough as shown in ***Figure 2.17(b).***

(a) (b)

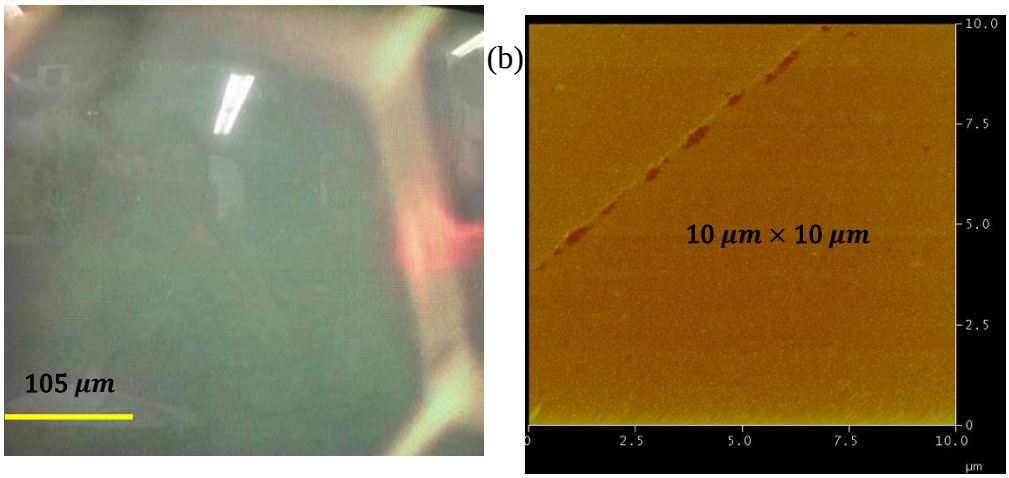

Figure 2.17: (a) Optical Microscope image on buried mesh. Red spot is the laser spot and (b) AFM image for same sample showing planar structure (Roughness ~ 10 nm)

2.3.7 Cu mesh with continuous ITO on Corrugated PET

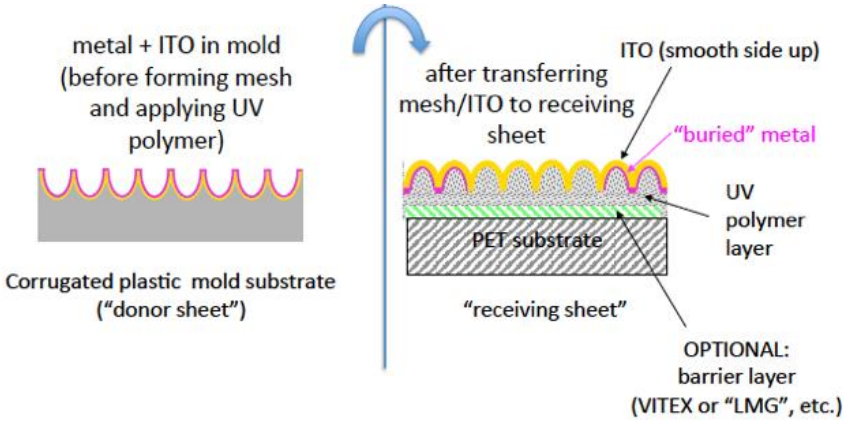

Figure 2.18: Schematic of Cu mesh with ITO on corrugated PET.

The schematic for the MCI's development of Cu mesh with ITO on corrugated surface is depicted on ***Figure 2.18***. AFM study carried for this class of substrate are with NREL, NIM 58, NIM 59 pattern. Cu mesh is proud for all these substrates. ***Table 2.7*** summarizes the corrugation attributes for the NIM 58 and NIM 59 pattern. The section analysis as well as the surface for these two patterns are shown in ***Figure 2.19(a)*** and ***Figure 2.19(b)*** respectively.

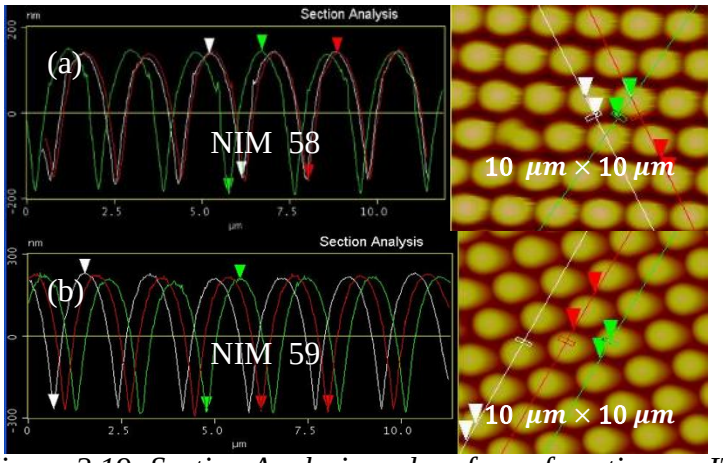

Table 2.7: NIM 58 & 59 surface

Pattern	*Pitch (μm)*	*Height (nm)*
NIM59	1.8	~ 500
NIM58	1.8	~300

Figure 2.19: Section Analysis and surface of continuous ITO and Cu mesh on NIM 58 and NIM 59 respectively.

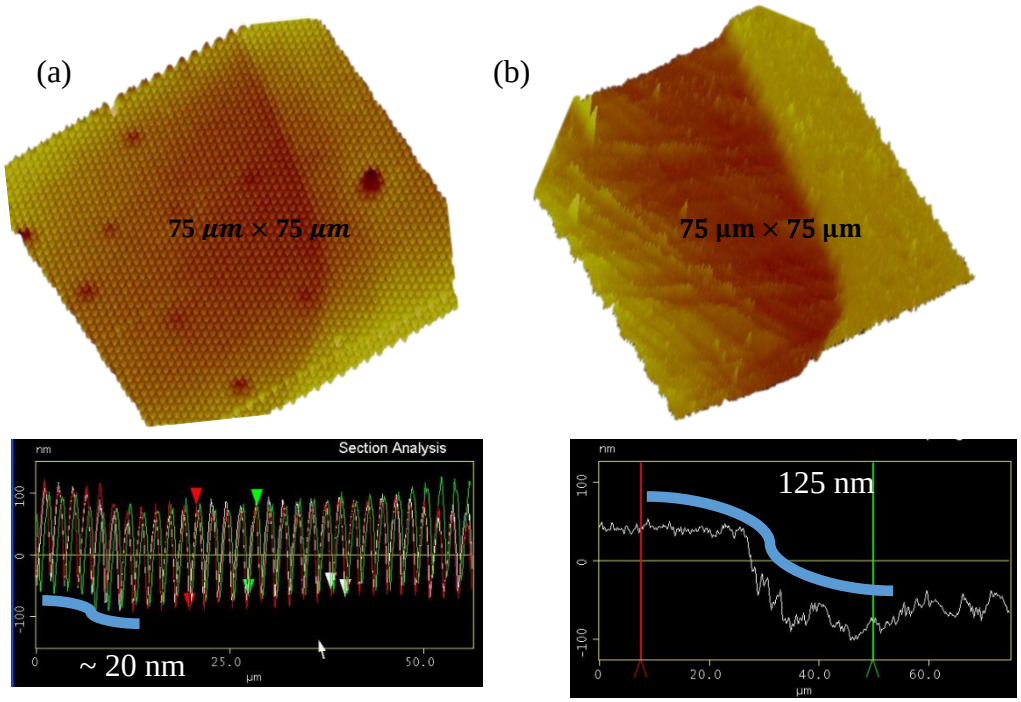

Figure 2.20: (a) Protruded Cu on NIM 58 with ~ 20 nm step and (b) Protruded Cu on NREL with ~ 125 nm step. Both scans are performed on (75 μm × 75 μm).

Figure 2.20 which show Cu protrusion are the AFM images of NIM 58 and NREL scanned on ($75\ \mu m \times\ 75\ \mu m$). The step however is much more prominent on NREL ($\times\ 5$) to that of NIM 58. The well resolved feature for NIM 58 is due to its wider period (~1.8 μm) which is nearly three times that of NREL($\sim 0.75\ \mu m$).

2.3.8 Micro lens Array

The substrate modes in OLEDs are those being trappped due to the refractive index mismatch between the substrate and and air [30]. MCI structure SAIC (+) (h~1.4 μm ; a~ 3 μm**)** as shown in ***Figure 2.21*** have been successful on extraction of the substrate mode.

MCI is currently optimizing design for microlens array. Such design will enhance substrate modes extraction contributing to larger outcoupling.

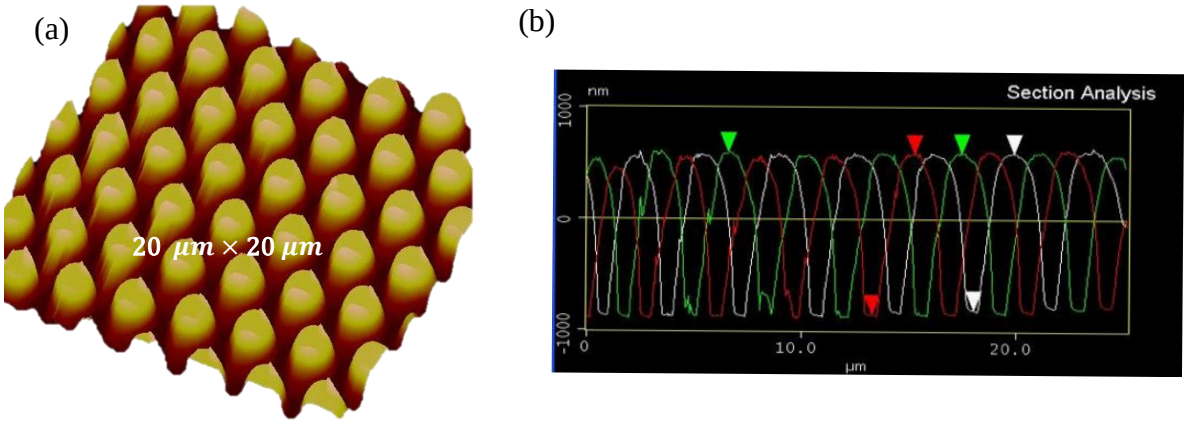

Figure 2.21: (a) Microlens (SAIC (+)) and (b) its surface profile.

2.3.9 Barrier Coating layer

AFM image on ***Figure 2.22*** is the structure of the barrier coating layer that team explored in the project. Barrier layer inclusion in the integrated OLED substrate is imperative for the stability of the OLED structure. Oxygen and moisture are the primary reason for the degradation of OLED and hence incorporating such layer is important.

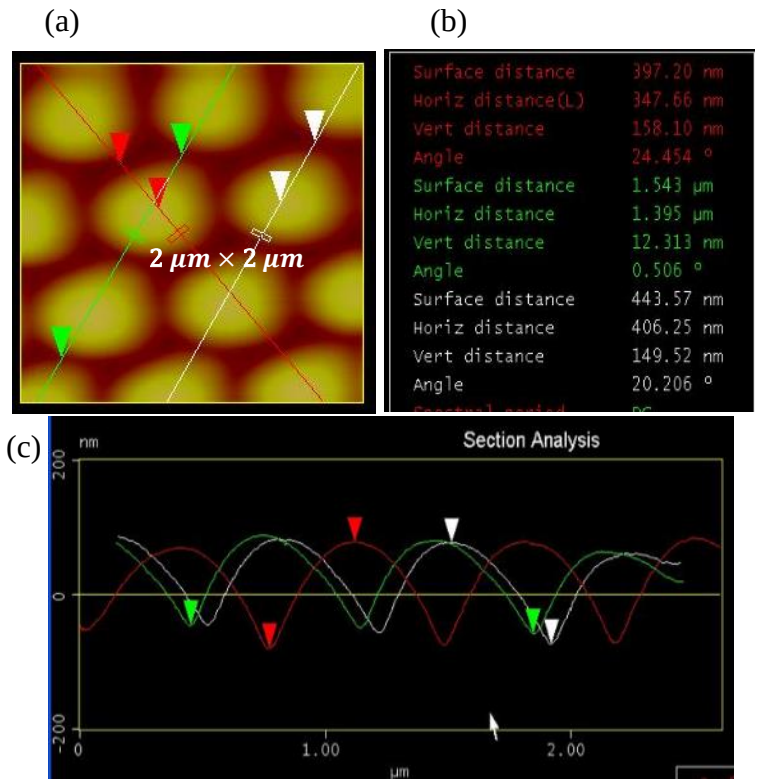

Figure 2.22: AFM (a) surface of barrier layer, (b) Profile attributes, and (c) surface profile.

2.4 Conclusions and Future work

This study provided a comprehensive examination of the planar as well as patterned plastic substrates of concave as well as convex geometry ranging from the period of few hundred nanometer to several microns. Besides, establishing quantitative merit of these substrate some of the challenges are also identified.

Regarding ITO on patterned substrates two key challenges are 1. *Quality of ITO*: The room temperature sputtering of ITO results on the amorphous ITO. Hence it is imperative that the ITO is sputtered on higher temperature to have polycrystalline ITO that could significantly improve its conductivity and the quality. 2. *ITO surface*: ITO on some of the patterned surface

were with sharp points. These surfaces need to be smoothened for uniform stacking of the OLED.

Cu mesh is important for boosting anode conductivity. However, its step/protrusion over the surface need to be optimized. Larger step result is shorting of the device due to nonuniform stacking over such surface.

Optimal design of microlens as well as barrier layer for encapsulation are also equally important.

This study was the precursor for the rest of the work in this dissertation. More qualitative approach of substrate design in conjunction with the OLEDs' characterization on some of these substrates are provide in chapter two.

2.4.1 Experimental procedure

2.4.1.1 Sample Preparation

10 mm × 10 mm plastic samples were carefully cut. It was blown up with Nitrogen to get rid of any contaminants. The sample was then mounted on 8 mm circular ferromagnetic metal puck with a help of double sided kepton tape.

2.4.1.2 Scanner and Cantilever/Tip characterization

Veeco Metrology Scanning Probe Microscopy was the scanner for acquiring image. AFM tip (Model TESPA-V2) used for scanning was purchased from Bruker Co. (brukerafmprobes.com). Cantilever/Tip is made up of Antimony (n) doped Si with a resistivity of 0.01-0.025 Ohm-cm. Its resonance frequency and spring constant is 320 kHz and 42 N/m respectively. The cantilever is 125 μm long and 40 μm wide without any coating on the front side whereas backside had 50 +/-10nm Al. Tip is 12.5 μm high [31].

2.4.1.3 Data Analysis

Nanoscope software was used for generating an image in topographical configuration. The Section Analysis tool was used for determining height and pitch of the pattern. The 3D image profile of the pattern was generated by changing viewing angle with respect to light angle.

2.5 References

[1] Kim, Sunkook, Kwon, Hyuk-Jun, Lee, Sunghun, Shim, Hongshik, Chun, Youngtea, Choi, Woong, Kwack, Jinho, Han, Dongwon, Song, Myoungseop, Kim, Sungchul, Mohammadi, Saeed, Kee, Inseo, and Lee, Sang Yoon. (2011). Low-power flexible organic light-emitting diode display device. *Advanced Materials (Deerfield Beach, Fla.), 23*(31), 3511-3516.

[2] Park, Mh, Han, Th, Kim, Yh, Jeong, Sh, Lee, Y, Seo, Hk, Cho, H, and Lee, Tw. (2015). Flexible organic light-emitting diodes for solid-state lighting. *Journal of Photonics for Energy, 5*(1), 053599-053599.

[3] Ni, H., Liu, J., Wang, Z., & Yang, S. (2015). A review on colorless and optically transparent polyimide films: Chemistry, process and engineering applications. *Journal of Industrial and Engineering Chemistry, 28*, 16-27.

[4] Xu, R., Li, Y., & Tang, J. (2016). Recent advances in flexible organic light-emitting diodes. *Journal of Materials Chemistry C, 4*(39), 9116-9142.

[5] Bender, V., Marchesan, T., & Alonso, J. (2015). Solid-State Lighting: A Concise Review of the State of the Art on LED and OLED Modeling. *IEEE Industrial Electronics Magazine, 9*(2), 6-16.

[6] Kaltenbrunner, M., White, M., Głowacki, E., Sekitani, T., Someya, T., Sariciftci, N., & Bauer, S. (2012). Ultrathin and lightweight organic solar cells with high flexibility. *Nature Communications, 3*(1), 770.

[7] Wang, D., Hauptmann, J., & May, C. (2019). OLED Manufacturing on Flexible Substrates Towards Roll-to-Roll. *MRS Advances, 4*(24), 1367-1375.

[8] https://microcontinuum.com/

[9] Hippola, Chamika, Kaudal, Rajiv, Manna, Eeshita, Xiao, Teng, Peer, Akshit, Biswas, Rana, Slafer, Warren Dennis, Trovato, Tom, Shinar, Joseph, and Shinar, Ruth. (2018). Enhanced Light Extraction from OLEDs Fabricated on Patterned Plastic Substrates. *Advanced Optical Materials, 6(*4), 1-11.

[10] Park, Jm, Gan, Zq, Leung, Wy, Liu, R, Ye, Z, Constant, K, Shinar, J, Shinar, R, and Ho, Km. (2011). Soft holographic interference lithography microlens for enhanced organic light emitting diode light extraction. *Optics Express, 19*(14), A786-A792.

[11] https://www.oledworks.com/wp-content/uploads/2016/08/Boroson-OLEDWorks-Flexible-OLEDs-final.pdf

[12] Meyers, G., & Grubb, David T. (2008). *Polymer microscopy.* (3rd ed. / L.C. Sawyer, David Grubb, Gregory F. Meyers. ed.). New York; London: Springer

[13] Vancso, G., & Schönherr, H. (2009). *Scanning force microscopy of polymers / by G. Julius Vancso, Holger Schönherr.* (Springer laboratory). Berlin; London: Springer.

[14] Voigtländer, B. (2015). *Scanning Probe Microscopy Atomic Force Microscopy and Scanning Tunneling Microscopy / by Bert Voigtländer.* (1st ed. 2015. ed., NanoScience and Technology).

[15] Echlin, P. (2009). *Handbook of sample preparation for scanning electron microscopy and x-ray microanalysis / Patrick Echlin.* New York: Springer.

[16] https://www.toray.com/network/business_jp/bus_003.html

[17] http://www.zeon.co.jp/business_e/enterprise/speplast/ndex.html

[18] https://modernplastics.com/supplier/bayer-sheffield-plastics-inc/

[19] https://www.tekra.com/products/brands/dupont-teijin-films/mylar

[20] https://www.azom.com/article.aspx?ArticleID=384

[21] https://en.wikipedia.org/wiki/Black_silicon

[22] Cowen, J.J., & Slafer, D.(1987). The Recording and replication of Holographic micropatterns for the ordering of Photographic Emusion Grains in Film systems., *Journal of Imaging Science, 31*(3)

[23] https://tfdinc.com/products/ito/

[24] Son, P., Choi, K., & Kim, S. (2012). Indium tin oxide exhibiting high poly-crystallinity on oxygen plasma-treated polyethylene terephthalate surface. *Nanoscale Research Letters, 7*(1), 1-4

[25] http://www.semicore.com/news/92-what-is-rf-sputtering

[26] https://www.norlandprod.com/adhesives/NOA170.html

[27] Qu, Y., Slootsky, M., & Forrest, S. (2015). Enhanced light extraction from organic light-emitting devices using a sub-anode grid. *Nature Photonics, 9*(11), 758.

[28] Tak, Yoon-Heung, Kim, Ki-Beom, Park, Hyoung-Guen, Lee, Kwang-Ho, & Lee, Jong-Ram. (2002). Criteria for ITO (indium–tin-oxide) thin film as the bottom electrode of an organic light emitting diode. *Thin Solid Films, 411*(1), 12-16

[29] Kim, Won-Kyung, Lee, Seunghun, Hee Lee, Duck, Hee Park, In, Seong Bae, Jong, Woo Lee, Tae, Kim, Ji-Young, Hun Park, Ji, Chan Cho, Yong, Ryong Cho, Chae, Jeong, Se-Young. (2015). Cu mesh for flexible transparent conductive electrodes. *Scientific Reports, 5*(1), 10715

[30] Gather, M., & Reineke, S. (2015). Recent advances in light outcoupling from white organic light-emitting diodes. *Journal of Photonics for Energy, 5*(1), 057607-057607.

[31] https://www.brukerafmprobes.com/images/product/specPDF/3844.pdf

CHAPTER 3. TUNING THE DESIGN OF CORRUGATED/PATTERNED PLASTIC SUBSTRATES FOR EFFICIENT OLEDs

3.1 Abstract

Successful corrugation design on the substrate is the precursor for efficient OLEDs. As substrate corrugation is the physical domain on which an OLED resides, its merit such as period and height, and subsequently their ratio, needs thorough examination. Probing intermittent contact mode atomic force microscopy (AFM) on various corrugated substrate design, key aspects viz., its smoothness, symmetry and consistency in the feature are described and discussed. In addition, white phosphorescent OLEDs fabricated on some of these designs are evaluated in light of their substrate attributes. The importance of the conformality of the ITO on corrugated substrate is also discussed. Few common defects on the patterned substrates are also shown.

3.2 Introduction

The efficiency of the OLEDs built on the conventional planar substrate like ITO/glass is ~ 20% [1]. This limitation arises from various loss mechanisms amongst which internal waveguiding, surface plasmon excitations, and substrate waveguiding are the major ones [1,2]. The first two loss mechanisms take place within the active layer of the OLEDs and can be minimized employing internal extraction means [1,4]. The third loss mechanism can be mitigated by the use of a microlens array, hemispherical lens, etc., on the air side of the substrate. [1,2,5].

Plastic substrates have a flexible form factor making them suitable candidates for stretchable/flexible Electronics [5,6]. This is important for industry as plastic substrates are amenable to roll-to-roll manufacturing [7]. Plastics, in addition to being transparent, have a refractive index ~ 1.6, closer to that of ITO (n ~ 2.0) and PEDOT: PSS (n ~ 1.6), which are common anode layer, than glass (n ~ 1.5).

Various studies have been done on using internal extraction means for the successful mitigation of the internal waveguiding and surface plasmon excitation loss from the cathode [4]. The Forrest group, devising low index grids (LIGs) successfully extracted 60% of the waveguided photons and substrate modes [2]. In a later study they used the multiwavelength scale dielectric grid between anode and substrate, successfully extracting the waveguided light [3]. Chang et al. used a simple solution processing method to fabricate nanocomposite thin films, with an internal scattering layer, to obtain a twofold enhancement in outcoupling efficiency [8]. With the use of a high refractive index glass substrate along with a macro extractor (e.g., a hemispherical lens) the Leo group eliminated the waveguide modes, reporting an EQE of 45% [9,10].

Like corrugated photonic crystals, substrate corrugation also enhances light outcoupling due to Bragg diffraction. Ishihara et. al fabricated OLEDs on the glass substrate with periodic corrugated structure (~ 300 nm) using nanoimprint lithography that produced 1.5-fold enhancement in light outcoupling [11]. Koo et al. reported 120% enhancement in current efficiency in green fluorescent OLEDs fabricated on a quasi-periodic/buckling structure [12]. The same group, using rapid convective deposition technique, made a quasi-periodic structure (~ 500 nm) of hexagonal-close-packed (HCP) silica arrays embedded into a thin film of polystyrene (PS) on the glass substrate which generated the extraction enhancement in current and power efficiency of 70% and 90% respectively [13].

This chapter describes using intermittent contact mode atomic force microscopy (AFM) to identify key elements necessary for effective substrate design on plastic for mitigating internal waveguiding as well as surface plasmon excitations at the organic/metal cathode interface.

3.3 Results and Discussions:

The true representation of any periodic pattern with aspect ratio (period to height ratio a/h) of 1:1 requires equal spacing along vertical and horizontal axis. This however would not be practical for two reasons: (1) when the pattern's period is much larger than its height, and (2) when multiple periods are to be presented. AFM image analysis overcomes these limitations by squeezing the horizontal scale. As all of the patterns in our study possess periods larger than their height, the projected height is always scaled up. To elucidate this, let us compare two type of patterns: a motheye (a~ 300 nm; h ~70 nm) and NIM 56 (a ~ 30 μm; h~ 1.4 μm) as shown in ***Figure 3.1.***

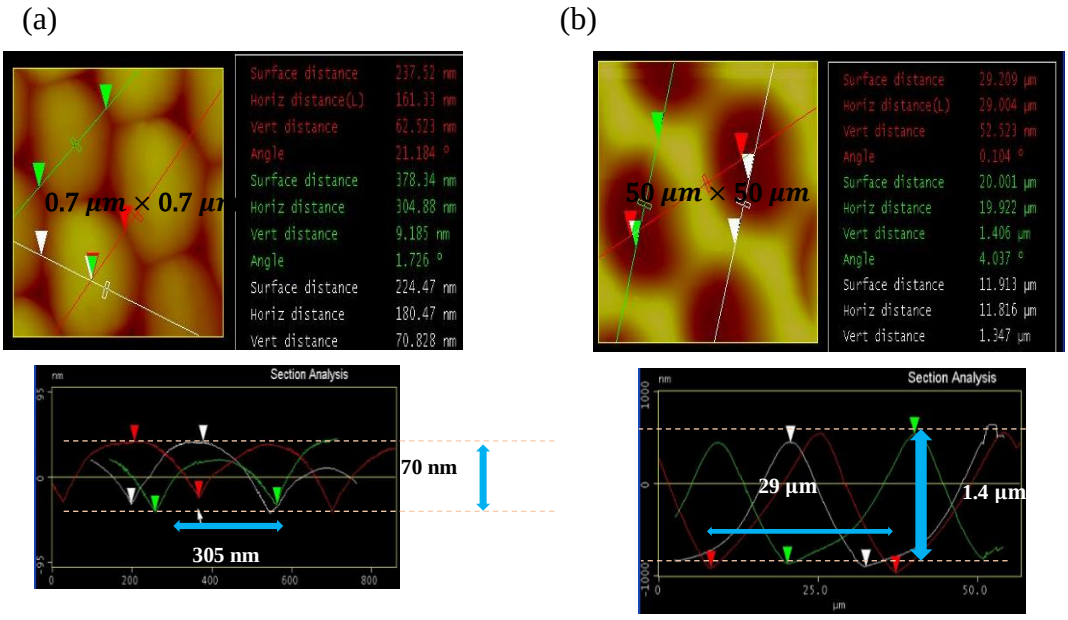

Figure 3.1: AFM images and surface profile.(a) Motheye patterned PC (*a*~ 300 nm; *h* ~70 nm) *on scan area* (0.7 μm × 0.7 μm) *and (b) NIM 56 patterned PET/CAB* (*a* ~ 30 μm; *h* ~ 1.4 μm)on scan area (50 μm × 50 μm).

Motheye pattern on ***Figure 3.1*** (a) (*a* ~ 305 nm ; *h* ~ 70 nm) has an aspect ratio of ~3:1 whereas NIM 56 (*a* ~ 29 μm, *h* ~ 1.4 μm) pattern on Figure 3.1(b) has an aspect ratio of ~20:1. If the scale was identically scaled both in vertical and horizontal axis, the period would be 3 and 20 times larger than the height for the former and latter, respectively. It is apparent however from

the images that the vertical scale is exaggerated 3 and 20 times for the motheye and NIM 56, respectively, compared to their horizontal scale. Hence while interpreting the image profile the aspect ratio must be taken into account. Despite this issue, AFM images convey valuable information on both the qualitative and quantitative merit of the substrate design. The key merits which AFM provides are as follows:

I. ***Surface Smoothness:*** Profiles which have sharp inflection points have enormous curvature. As OLEDs are field driven devices there will be very high electric field at such points. Hence smooth profile with gentle curvature is optimal for the OLED stacking. The layers on such profiles tend to be of uniform thickness.

II. ***Symmetry/Consistency*****:** AFM provides information on the symmetry of the feature as well as the arrays of features through the section analysis tool. It can also give information on the consistency of the feature size along various directions.

These two aspects of AFM will be reiterated throughout this chapter that is divided into four sections:

i. Section 1 tabulates the aspect ratio for the plastic patterns introduced in Chapter 2, which are on PC and PET/CAB substrates. Aspect ratio is useful in assessing the actual surface of the pattern.

ii. In Section 2 white PhOLEDs fabricated on representative patterns of both PC and PET/CAB, is discussed. The relation between substrate design and OLED performance is established.

iii. In Section 3 conformal ITO coating as an anode on the wider period substrate is envisioned.

iv. Some of the common defects on the substrate pattern are presented in section 4.

3.3.1 Aspect ratio

3.3.1.1 PC patterns

NREL, NILT and SAIC pattern as introduced on chapter 1 of this dissertation are the most common pattern for the PC substrates. ***Figure 3.2*** below provides the AFM images of those surfaces and their corresponding profiles. The convex and concave profiles for each of these pattern are mirror images of each other within reasonable approximation.

The approximate aspect ratio of these patterns are presented on ***Table 3.1*** (for height and period please refer to ***Table 2.2***). The range in the aspect ratio for NREL and NILT pattern takes in account of the shorter and taller version of these patterns.

Table 3.1: Aspect ratio of patterned PC substrates

Pattern	*Approx. Aspect Ratio (Period/Height)*
Moth eye	3:1
NREL LCC (convex and concave)	2:1-5:1
NREL-ZEONOR	10:1
NILT (convex and concave)	4:1-4:3
SAIC-1 LCC & PMMA (convex and concave)	4:1

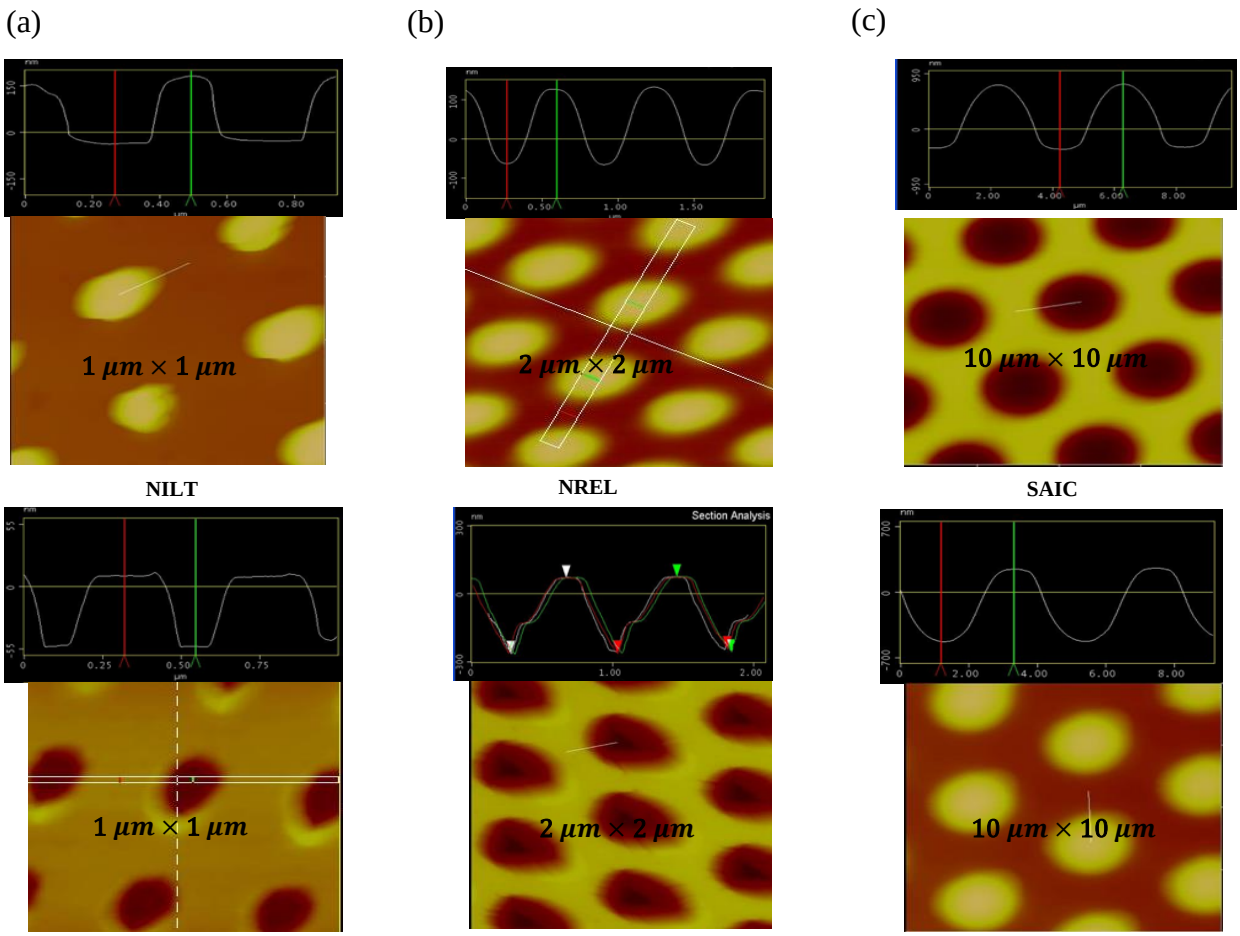

Figure 3.2:Patterned PCs and their section analysis of (a) NILT, (b) NREL and (c) SAIC

3.3.1.2 PET/CAB patterns

PET/CAB patterns are mostly concave pattern (UV on PET being an exception). In total, 10 different patterns are studied. NIM 14 is of two verisons; shallow and deep. NIM 56 is the widest as well as the deepest. NIM 16 and UV on PET are the 1-D (Burrow like) pattern. ***Figure 3.3*** & ***Figure 3.4*** below provides the AFM images of those surfaces and their corresponding profiles.

Table 3.2: Aspect ratio of patterned PET/CAB substrates

Pattern	*Approx. Aspect Ratio (Period/Height)*
NIM 14 - Deep Gaussian	3:1
NIM 14 -Shallow Gaussian	5:1
NIM 16	5:2
NIM 30	2:1
NIM 31	25:1
NIM 53	6:1
NIM 56	20:1
NIM 22	5:2
NIM 58	6:1
NIM59	4:1
UV on PET (LTZ156B)	2:1

These ratio as a metric is useful for optimal substrate design.

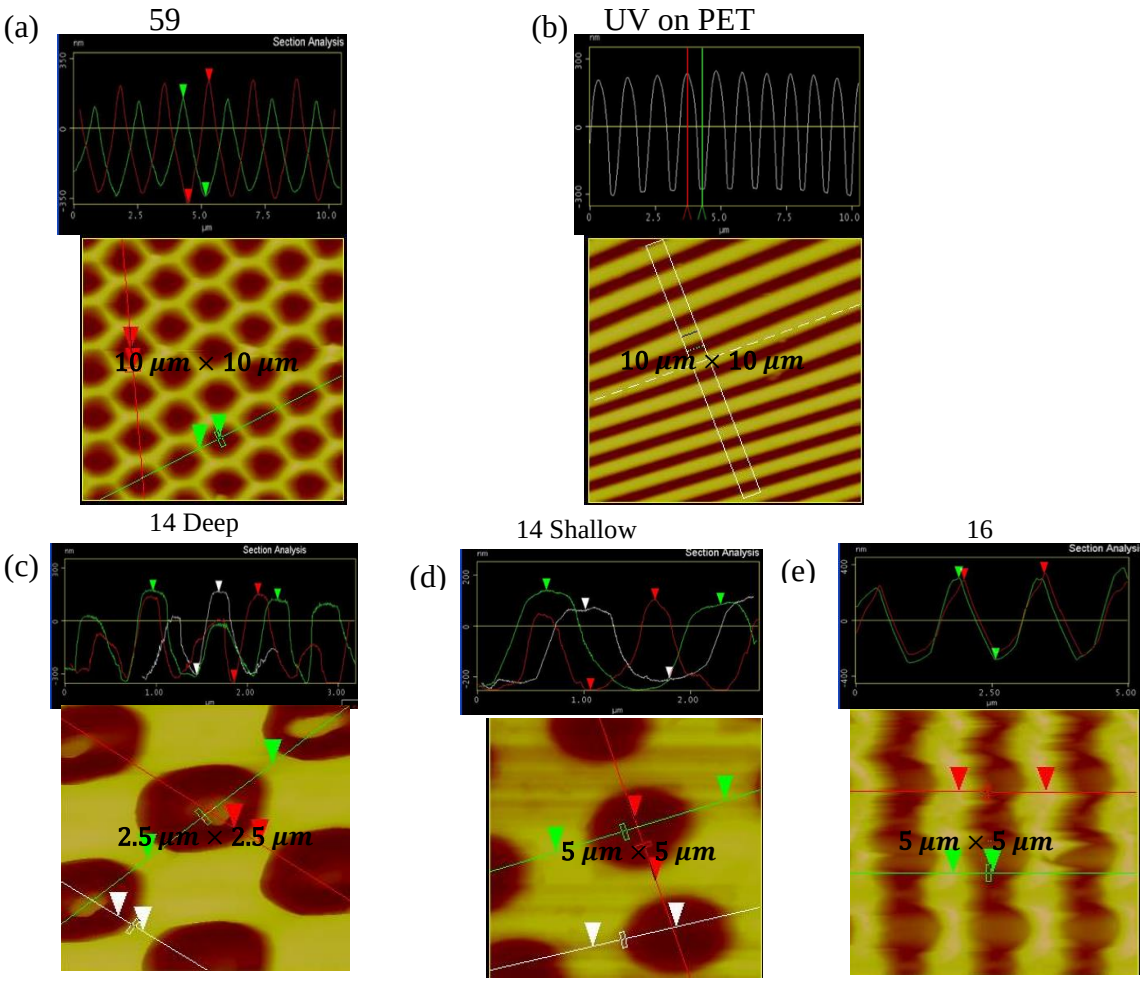

Figure 3.3: Patterned PET/CAB (NIM) substrates; (a) 59 and (b) UV on PET(LTZ156B) :(c) 14 Deep, (d) 14 Shallow, (e) 16

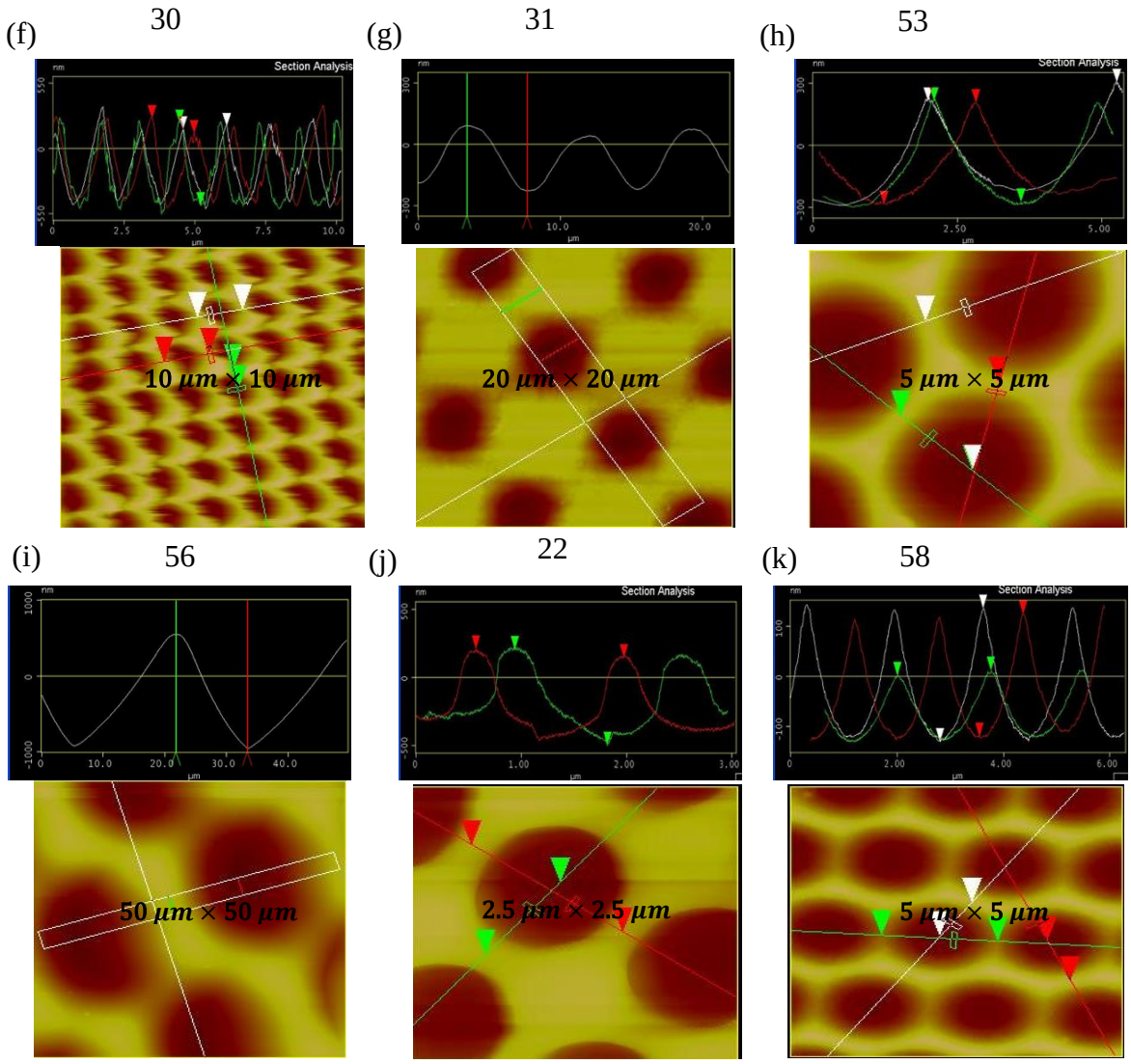

Figure 3.4: Patterned PET/CAB (NIM) substrates continue; (f) 30, (g) 31, (h) 53, (i) 56, (j) 22 and (k) 58

The aspect ratio of these patterns is presented on ***Table 3.2*** (For height and period of these patterns, please refer to ***Table 2.3***)

3.3.2 OLED Results

In this section, white phosphoroscent OLEDs fabricated on three set of substrates are separetely discussed. The goal is to understand what role does pattern design have on the OLED performance. White PhOLED is *(PEDOT:PSS (single layer)/HAT-CN (5nm)/**10% MoOx: TAPC***

(X)*/HAT-CN (5nm)/TAPC (20nm)/8% FIrpic:mCP (19nm)/6% PO-01:mCP (1nm)/TmPYPB (20nm)/20% CsF:TmPYPB (40nm)/LiF (1nm)/Al (100nm));* ***X*** *is the thickness in nm.*

PEDOT:PSS is poly(3,4-ethylenedioxythiophene), HAT-CN is (1,4,5,8,9,11-hexaazatri-phenylenehexacarbonitrile), TAPC is (1,1-bis[(di-4-tolylamino)phenyl]cyclohexane), FIrpic is bis[2-(4,6-difluorophenyl)pyridinato-C2,N](picolinato)iridium, mCP is 1,3-bis(N-carbazolyl)benzene, PO-01 is (thieno-pyridine framework organo-iridium complex) & TmPyPB is 1,3,5-tri(m-pyridin-3-ylphenyl)benzene.

3.3.2.1 White PhOLED on Sinusoidal/ Smooth PC substrate

White PhOLED was fabricated on patterned NREL PC (Taller version: a~ 750 nm; h~300 nm) as well as flat PC. Patterned PC is MOBAY type which is thicker (380 μm) and thus less prone to oxygen and moisture than other PCs. The thick doped HTL, (***10 % MoO_x: TAPC (120 nm)*** is used in the stack for taller corrugation. WPhOLED on patterned PC is $\times$ **1.7** enhanced to the flat. The EQE plot as shown in ***Figure 3.5*** depicted that the enhancement are at very high brightness. Onset of roll off at higher brightness suggest that the OLED is stable.

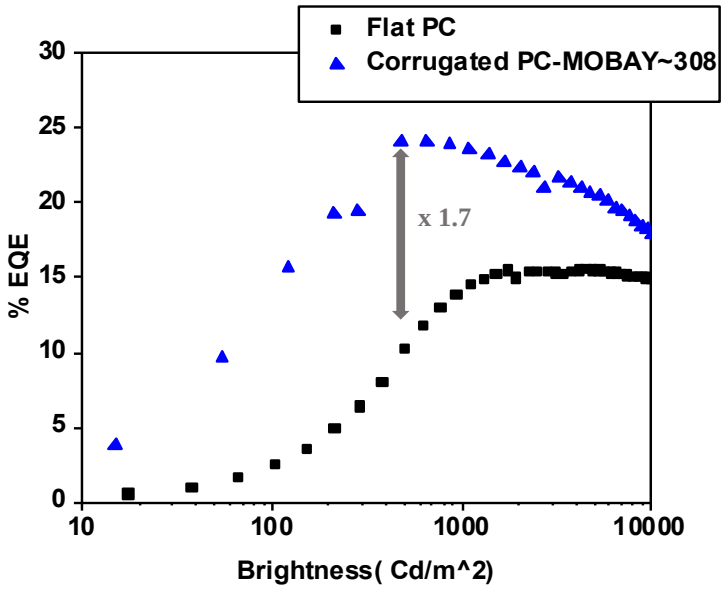

Figure 3.5: EQE of Efficient White PhOLED stacked on patterned MOBAY PC (a~ 750nm; h~300 nm).

AFM characterization of the substrate as shown in ***Figure 3.6***. Feature height of the pattern is~ 300 nm and its period ~ 750 nm.

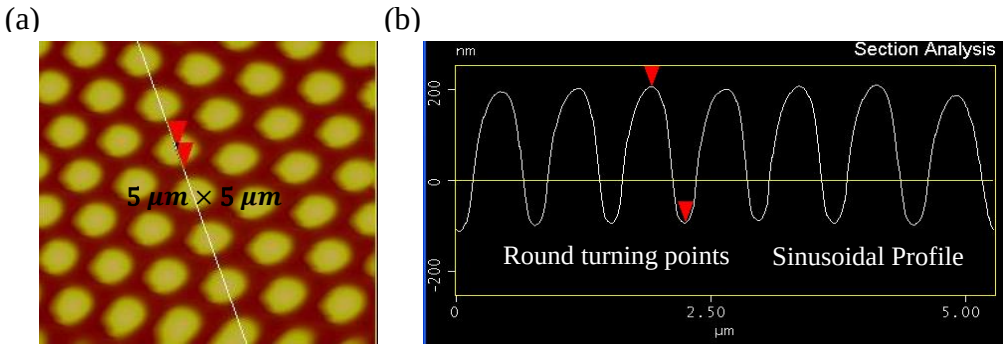

Figure 3.6: (a) NREL Patterned PC-MOBAY (5 μm × 5 μm) and (b) Pattern Profile, its attributes highlighted.

(i) **Round turning points** in the profile is suitable for OLED. The sharp edges are detrimental to OLEDs due to high electric field on those points. (ii) The **sinusoidal** curve is neither convex or concave. Such curve provides ideal surface for uniform stacking of the OLED layers.

3.3.2.2 White PhOLEDs on uniform patterns with PEDOT:PSS smoothening

In this set two type of patterned PCs; shallow NREL (a~ 750 nm; h <200 nm) and shallow NILT (a~ 400 nm; h< 200 nm) is used. Thin doped HTL (***10 % MoO_x: TAPC (40 nm))***

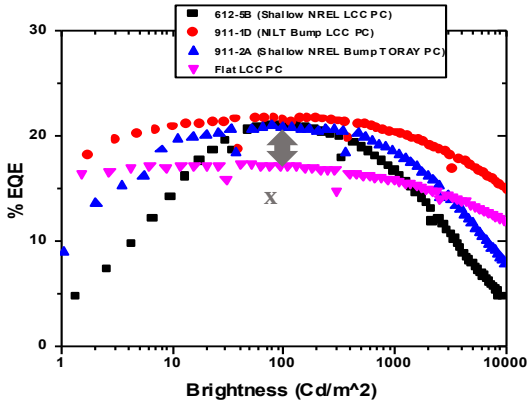

Figure 3.7: EQE of Efficient White PhOLEDs on patterned PCs; shallow NREL and shallow NILT.

layer is used as the corrugation height is shallower for this set.White PhOLEDs on both patterned substrate is enhanced $\times$ $\mathbf{1.5}$ to the control device as inferred from the EQE plot in ***Figure 3.7.*** The roll off these devices also strats at the high brightness suggesting that the device were stable.

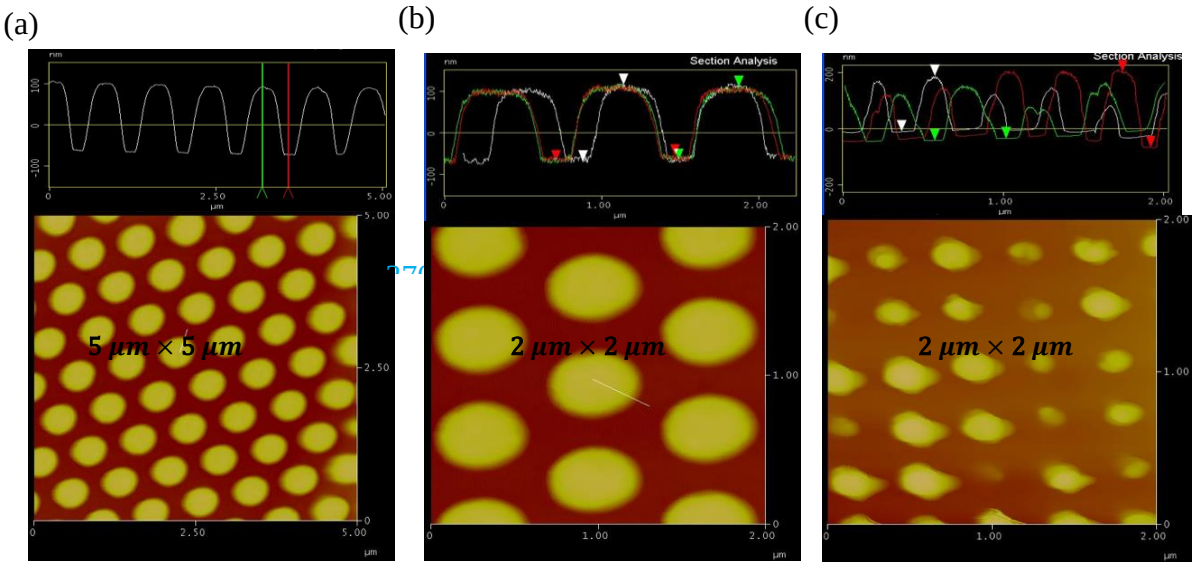

Figure 3.8: Shallow Patterned PCs (a) NREL on LCC PC, (b) NREL on TORAY PC and (c) NILT on LCC PC.

Based on the color distribution in the AFM images as shown in ***Figure 3.8***, the high degree of surface homogeneity can be inferred for the substrates used. The corrugation attributes for these substrates are tabulated on ***Table 3.3.***

Table 3.3: Corrugation attributes of Patterned PC substrates

Patterned PC (Shallow/Convex)	*Period (nm)*	*Height (nm)*
NREL on LCC	~ 753	164, 177
NILT on LCC	~ 371	186, 188
NREL on TORAY	~ 758	176, 184

Besides substrate quality, the **smoothening** of the turning points as a result of the solution processed anode could be the subordinate factor for increased efficiency.Thin layer of PEDOT:PSS is used as an anode. ***Figure 3.9*** shows such smoothening effect for both patterns.

(a) (b)

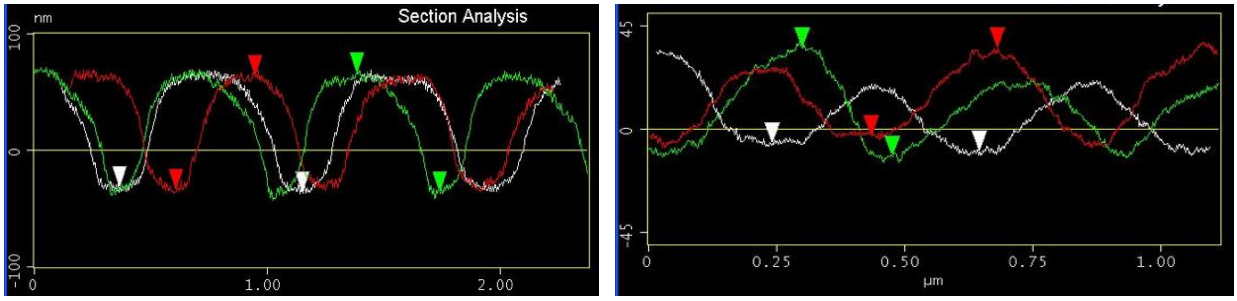

Figure 3.9: Surface profile after PEDOT: PSS treatment on the substrates: (a) Shallow NREL PC and (b) NILT PC.

3.3.2.3 White PhOLED on ITO coated PET/CAB micropatterns with non unifrom surface

ITO on NIM 58 and NIM 59 are the substrates for this set. Period for both of these pattern is ~ 1.8 μm. White PhOLED with thick doped HTL (***10 % MoO_x: TAPC (120 nm)***. From the EQE curve of ***Figure 3.10*** it can be inferred (i) OLED on NIM 58 is similar to the control devices. (ii) OLED on NIM 59 is poorer compared to the control devices.

The difference on the OLED performance on the two NIM patterns can be attributed to their substrate properties. ITO surface on NIM 58 is more favorable to OLED stacking than to NIM 59.

This could be inferred from taking closer look at the surface profile of these two patterns as shown in ***Figure 3.11***. The blue arrow for the ITO on NIM 59 pattern represents the difference in the height while running the cursor in two different directions. The red line for both patterns traverses through the nearest neighbor/adjacent feature.

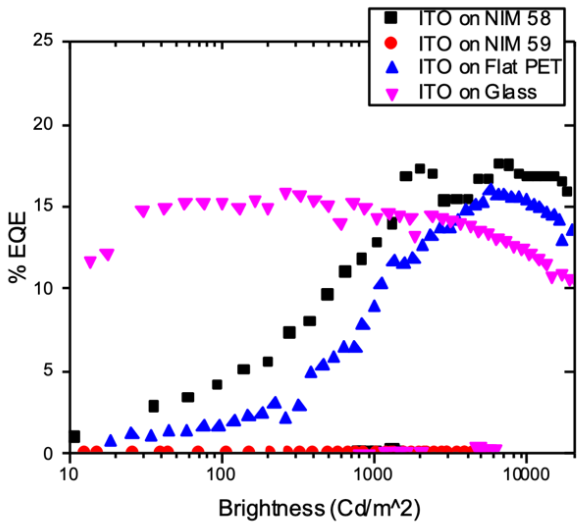

Figure 3.10: EQE plot for the ITO on PET/CAB substrates (NIM 58 and NIM 59) and the reference devices.

(a) ITO on NIM 59 (b) ITO on NIM 58

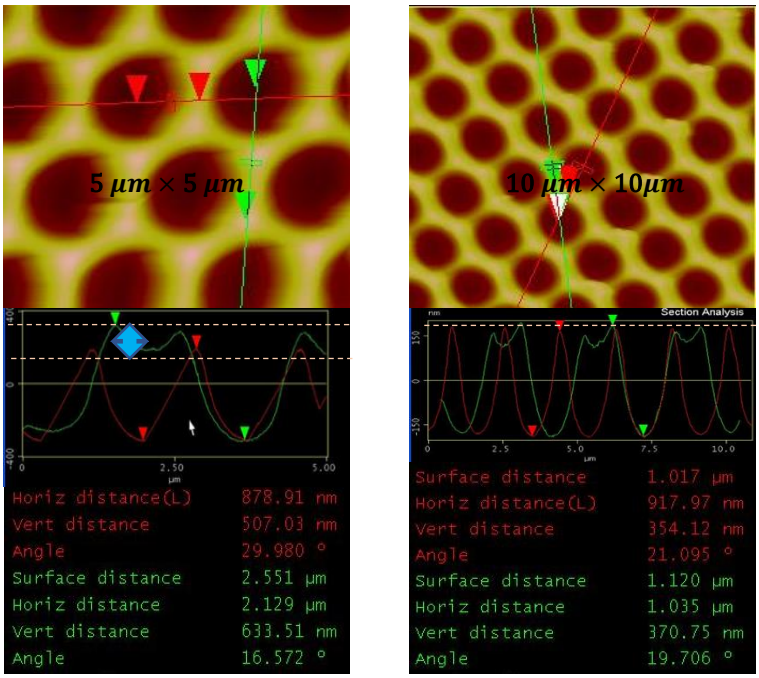

Figure 3.11: ITO on PET/CAB Substrates (a) NIM 59 and (b) NIM 59.

The dotted profile indicates the difference in the height. See the green and the red line on the surface.

The green line on other hand traverses through the second nearest neighbor. Height as per green and red profile for NIM 58 are 371 nm and 354 nm respectively with their difference being

~ 20 nm. For NIM 59; green and red profile measures 634 nm and 507 nm with their difference as ~ 127 nm. Thus, the difference in height for NIM 59 is seven fold that of NIM 58. This could potentially lead to non uniformity in the OLED stacking on NIM 59 comapred to those on the NIM 58 and hence to the poor device performance.

3.3.3 Conformal ITO anode

The corrugation approach relies on the conformal coating of each layer from anode to the cathode [12]. Even though the aspect ratio of the corrugation plays an important role in conformal stacking of each layer it is imperative that the corrugation reach up to the metal cathode [4]. Only then the disruption of the internal waveguiding as well as reduction in the surface plasmon excitations occurs, contributing to better efficiencies.

The anode layer in bottom emitting OLEDs resides between the corrugated substrate and the organic layers.This layer requires careful processing whether it is sputtered or solution processed. Inferior anode quality aggravates device performance since charge injection suffers which in turn tips off charge balance, one of the key factors contibuting to *EQE* [15].

In the course of this disseration work successful devices with strong enhancement are reported in subsequent chapters where the anode layer is PEDOT:PSS.

Even though both ITO and PEDOT:PSS are used as an anode for OLEDs, ITO coating is a more viable approach for the industry. The solution processed anode like PEDOT:PSS is not optimal for the large scale coating even though it has a lower refractive index ($\eta_{PEDOT:PSS}$~1.8) matching more closely with refractive index of plastic ($\eta_{plastic}$~ 1.6) than ITO (η_{ITO}~ 2).

In this dissertation several ITO patterned substrates on various periods are probed (See Table 4, Chapter 2). ITO coating over the wider period pattern are more conformal than the narrower period pattern. NIM 31 pattern as a bare substrate embodies the feature cavity (a ~ 7.8

μm; h~ 320 nm) with aspect ratio of ~ 25:1, is an optimal structure for ITO sputtering. This is evident from the height measurement of the ITO coated NIM 31 pattern (a~ 7.8 μm; h~ 330 nm) as shown in ***Figure 3.12***. The retention of the height shows that this structure is highly conformal even after ITO coating. The dotted line as depicted on the profile of ***Figure 3.12*** also indicates that the structure is isotropic in terms of height unlike ITO on NIM 59 substrate of the previous section. This suggest that NIM 31 pattern is suitable pattern for the ITO coating.

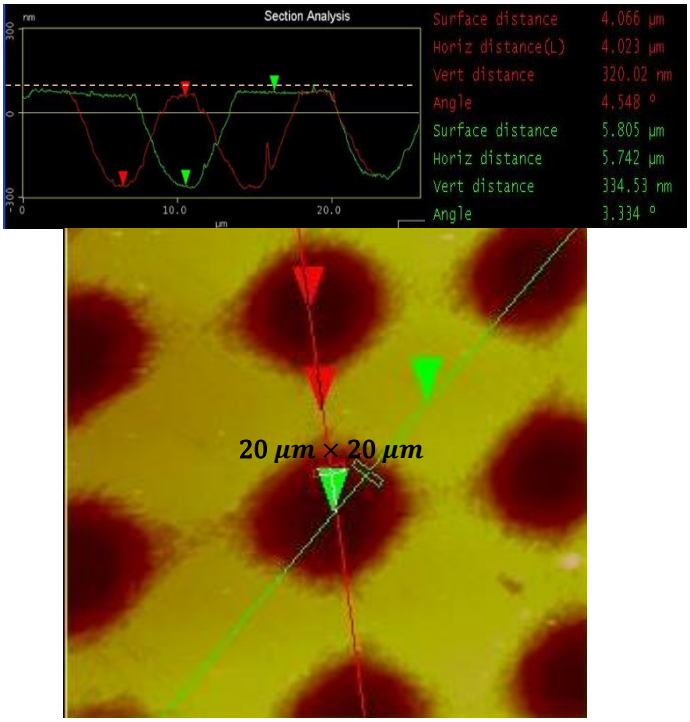

Figure 3.12: ITO on NIM 31 substrate (h~ 330 nm, a~ 7.8 µm) surface and its profile

3.3.4 Defect

Substrate pattern is the physical domanin for the OLED stack and hence its quality plays crucial role on the device performance. Even so, it is non realistic to have defect free substrate. AFM on few occasions revealed defects on the substrate pattern.The sources of these defects could be the stamping tool, handling or packaging issues. ***Figure 3.13*** shows the image with

random defects likely from the stamping tool. The encircled area within the image highlights the defect areas. The blue arrow points to the patch where features are missing.

Figure 3.14 shows another example of the defect in smaller and larger area for the same substrate. ***Figure 3.14(a)*** of ($5\ \mu m\ \times\ 5\ \mu m$) scan shows resolved image of defect with inhomogenous feature arrays. On the larger size scan of ***Figure 3.14(b)*** ($25\ \mu m\ \times\ 25\ \mu m$) fault like defects traversing throughout the pattern is clearly visible.

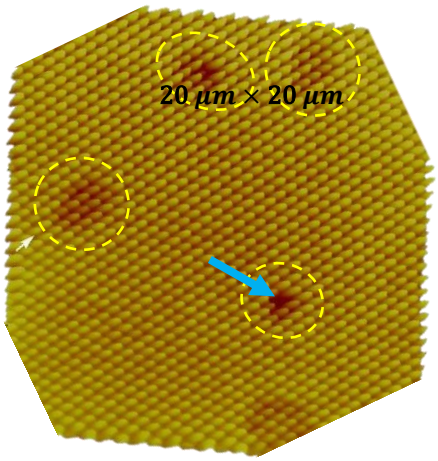

Figure 3.13:Random defects on patterned PC substrate as encircled. Arrow represent area of missing features.

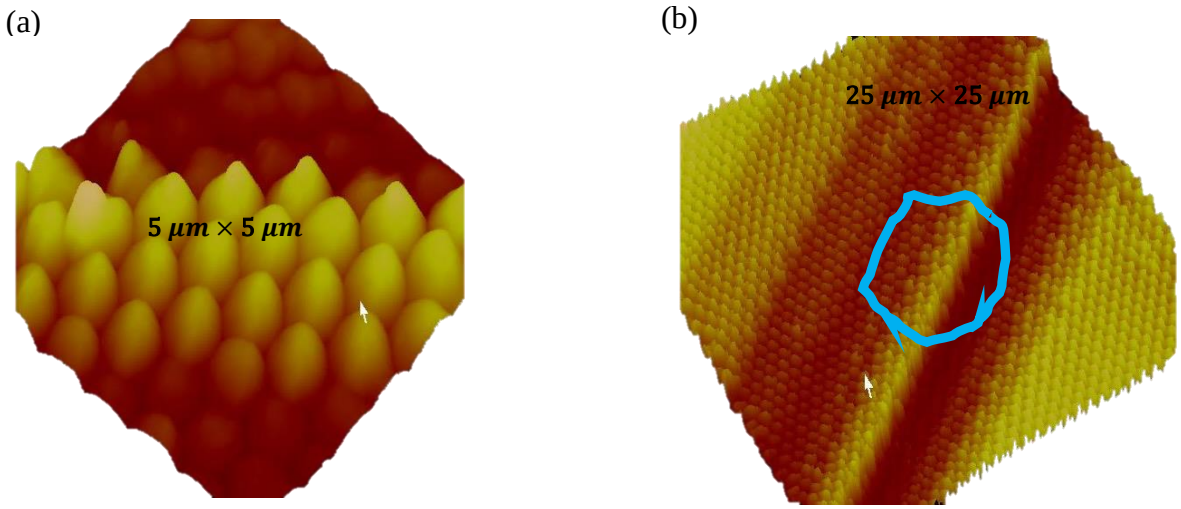

Figure 3.14: Damaged patterned PC substrate on smaller and larger scan size. (a) ($5\ \mu m\ \times\ 5\ \mu m$) *and (b)* ($25\ \mu m\ \times\ 25\ \mu m$) *Highlighted area in blue color on (b) is the area of the image for (a).*

3.3.5 Limitations of AFM

Although AFM as a probe provides valuable information on the various design aspects of the substrate there are limitations:

1. AFM is not suitable for mapping large areas such as the 1.5 mm diameter OLED pixels fabricated on these nano/micropatterns in this study, as it is several orders of magnitude larger than the images shown here. Often these substrate have meso-size defects and irregularities which are not seen in the small scan size.
2. AFM is not optimal for probing features with deep cavity.

3.4 Conclusion and Future Works

1. Qualitative aspects of PC and PET/CAB substrates are established with aspect ratio as the primary metric. It is particularly useful when the height and period differ substantially for any pattern.
2. AFM as a metrology tool conspiciously traces the contour of the turning points of the surface providing information on the roughness of the surface. In addition, it is deducive about the symmetry of the feature, which in turn quantifies the uniformity of the surface in various directions.
3. OLED performance and the substrate on which it is stacked is interrelated. White PhOLEDs fabricated on three different set of substrates confirm this conclusion.
4. Conformal OLEDs require conformal anode. ITO on wider period substrates is more viable for industry as opposed to solution processed anode like PEDOT:PSS.
5. In subsequent chapters the strong *EQE* enhancement observed in the OLEDs stacked on two different patterned plastics, PC and PET/CAB is presented. Chapter 4 details the two fold enhancement from green PhOLEDs on nanodome patterns on PC. Chapter 5 is on 2-

fold enhancement observed on white PhOLEDs fabricated on microarrays on PET/CAB substrates.

3.5 Experimental procedure

3.5.1 Sample Preparation

PC and PET samples were 10 mm × 10 mm. They were mounted on 8 mm diameter circular ferromagnetic metal pucks using double sided tape.

3.5.2 Scanner and Cantilever/Tip characterization

Veeco Metrology Scanning Probe Microscopy was the scanner; the Sb-doped Si AFM tips of TESPA-V2 model of (resistivity 0.01-0.025 Ωcm) were from Bruker (brukerafmprobes.com). Tip was with resonant frequency of 320 kHz and spring constant of 42 N/m. It was 125 μm long and 40 μm wide without any coating on the front side, whereas the backside had 50+/-10nm Al.

3.5.3 Data Analysis

Nanoscope software was used for generating an image in topographical configuration. The Section Analysis tool was used for determining height and pitch of the pattern. The 3D image profile of the pattern was generated by changing the viewing angle with respect to lighting angle.

3.5.4 OLED fabrication and characterization

OLEDs were fabricated on the ITO/PEDOT: PSS-coated corrugated and flat plastic substrates as well as on glass/ITO substrates for reference. The Al cathode and all organic materials were deposited by thermal evaporation inside a chamber (base pressure of $< 10^{-6}$ mbar) within a glovebox. The Al cathode was deposited through a 2”x2” shadow mask containing an array of 1.5 mm diameter circular holes. Characterization of the OLEDs was done using a

Keithley 2400 source meter. The brightness was measured by a Minolta LS110 luminance meter and the EL spectra were obtained using an Ocean Optics PC2000-ISA spectrometer. The raw spectra were obtained in the "SCOPE" mode but were corrected to the radiometrically calibrated mode; the spectra shown are the corrected spectra. Labview software was used to calculate the efficiencies from the experimental data.

3.5.5 Materials

The flat and patterned PC and PET/CAB substrates with various pattern designs, heights, and pitches were fabricated by MicroContinuum, Inc. PEDOT: PSS was from Heraues Clevios, LiF from Sigma-Aldrich, MoO_3 from Sterm Chemicals, and HAT-CN, TAPC, TmPyPB, mCP, FIrpic, $Ir(ppy)_3$, and PO-01 were from Luminescence Technology (Lumtec) Corporation.

3.6 References

[1] Hippola, Chamika, Kaudal, Rajiv, Manna, Eeshita, Xiao, Teng, Peer, Akshit, Biswas, Rana, Slafer, Warren Dennis, Trovato, Tom, Shinar, Joseph, Shinar, Ruth. (2018). Enhanced Light Extraction from OLEDs Fabricated on Patterned Plastic Substrates. *Advanced Optical Materials, 6*(4), 1-11.

[2] Sun, Y., & Forrest, S. (2008). Enhanced light out-coupling of organic light-emitting devices using embedded low-index grids. *Nature Photonics, 2*(8), 483-487.

[3] Qu, Y., Slootsky, M., & Forrest, S. (2015). Enhanced light extraction from organic light-emitting devices using a sub-anode grid. *Nature Photonics, 9*(11), 758-763.

[4] Salehi, A., Fu, X., Shin, D., & So, F. (2019). Recent Advances in OLED Optical Design. *Advanced Functional Materials, 29*(15), 1-21.

[5] Kim, Sunkook, Kwon, Hyuk-Jun, Lee, Sunghun, Shim, Hongshik, Chun, Youngtea, Choi, Woong, Kwack, Jinho, Han, Dongwon, Song, Myoungseop, Kim, Sungchul, Mohammadi, Saeed, Kee, Inseo, Lee, Sang Yoon. (2011). Low-power flexible organic light-emitting diode display device. *Advanced Materials (Deerfield Beach, Fla.), 23*(31), 3511-3516

[6] Park, Min-Ho, Han, Tae-Hee, Kim, Young-Hoon, Jeong, Su-Hun, Lee, Yeongjun, Seo, Hong-Kyu, Cho, Himchan, Lee, Tae-Woo. (2015). Flexible organic light-emitting diodes for solid-state lighting. *Journal of Photonics for Energy, 5*(1), 053599-053599.

[7] Wang, Dongxiang, Jacqueline Hauptmann, and Christian May. "OLED Manufacturing on Flexible Substrates Towards Roll-to-Roll." *MRS Advances* 4.24 (2019): 1367-375. Web.

[8] Chang, Hong-Wei, Tien, Kun-Cheng, Hsu, Min-Hung, Huang, Yi-Hsiang, Lin, Ming-Shiang, Tsai, Chih-Hung, Tsai, Yu-Tang, Wu, Chung-Chih. (2011). Organic light-emitting devices integrated with internal scattering layers for enhancing optical out-coupling. *Journal of the Society for Information Display, 19*(2), 196-204.

[9] Reineke, S., Lindner, F., Schwartz, G., Seidler, N., Walzer, K., Lüssem, B., & Leo, K. (2009). White organic light-emitting diodes with fluorescent tube efficiency. *Nature, 459*(7244), 234-238.

[10] Riedel, B., Hauss, Geyer, Guetlein, Lemmer, & Gerken. (2010). Enhancing outcoupling efficiency of indium-tin-oxide-free organic light-emitting diodes via nanostructured high index layers. *Applied Physics Letters, 96*(24), Applied Physics Letters, 14 June 2010, Vol.96(24).

[11] Ishihara, K., Fujita, Matsubara, Asano, Noda, Ohata, Hirasawa, Nakada, Shimoji. (2007). Organic light-emitting diodes with photonic crystals on glass substrate fabricated by nanoimprint lithography. *Applied Physics Letters, 90*(11), Applied Physics Letters, 12 March 2007, Vol.90(11).

[12] Koo, W., Jeong, S., Araoka, F., Ishikawa, K., Nishimura, S., Toyooka, T., & Takezoe, H. (2010). Light extraction from organic light-emitting diodes enhanced by spontaneously formed buckles. *Nature Photonics, 4*(4), 222-226.

[13] Light Extraction of Organic Light Emitting Diodes by Defective Hexagonal-Close-Packed Array. (Report). (2012). *Advanced Functional Materials, 22*(16), 3454-3459.

[14] https://microcontinuum.com/

[15] National Research Council. Committee on Assessment of Solid-State Lighting. (2017). *Assessment of solid-state lighting, phase two / Committee on Assessment of Solid-State Lighting, Phase 2, Board on Energy and Environmental Systems, Division on Engineering and Physical Sciences.*

CHAPTER 4. ENHANCED LIGHT EXTRACTION FROM GREEN PHOSPHOROSCENT OLEDS USING SHALLOW NANOCONES ON POLYCARBONATE SUBSTRATE

4.1 Abstract

Green PhOLEDs stacked on convex conical arrays with aspect ratio of ~4:1 (period a ~ 750 nm, height h ~ 170 nm) on PC substrate demonstrate two-fold light extraction enhancement compared to its control device. As peak efficiencies of the enhanced OLEDs are at higher brightness, they pertain to display and lighting applications. Intermittent contact/tapping mode atomic force microscopy (AFM) is used to characterize bare substrates as well as substrates coated with the solution processed PEDOT: PSS anode. AFM also successfully shows the remnant corrugation on organic/cathode interface providing direct physical evidence on its effectiveness on mitigating losses through internal waveguiding and surface plasmons. The conformality was evaluated using Focused Ion beam (FIB). Scanning Electron Microscopy (SEM) also reveals the remnant corrugation on the OLED both at organic/cathode interface as well as on top of the cathode, confirming the findings made by AFM.

4.2 Introduction

OLEDs are already a mature technology underpinning consumer electronics. They are found in smartphone displays, watches, and TVs since they provide thinner, brighter displays with vibrant colors and infinite contrast. Despite several attractive attributes of OLED technology, the effective light outcoupling from it still remains a major technological challenge. In the conventional bottom emitting OLED, the light outcoupling η_{out} (the ratio of the number of photons making their way out in the forward hemisphere to the number of photons generated

with in the emissive layer of the OLED) is limited to ~ 20 %. The current DOE target for 2020 is η_{out} = 70% [1].

Direct measurement of η_{out} is not possible; it can only be estimated from the External Quantum Efficiency η_{EQE} which is the ratio of the number of photons emitted into the forward hemisphere to the number of electrons injected into the OLED [2,3]. Clearly

$$\eta_{EQE} = \eta_{out} \cdot \eta_{IQE} \quad \text{4.1}$$

where the internal quantum efficiency η_{IQE} is the ratio of number of photons generated within the OLED to the number of electrons injected into it. η_{IQE} is given by,

$$\eta_{IQE} = \gamma \cdot \varphi_{PL} \cdot r_{ex} \quad \text{4.2}$$

where γ is the charge balance factor, $\varphi_{PL}$is the intrinsic photoluminescence quantum yield, r_{ex} is the radiative exciton recombination factor, which is ~0.25 for conventional fluorescent materials where only singlet excitons can decay radiatively, but ~1 for some phosphorescent materials where both singlet and triplet excitons can decay radiatively.

Recapping, ~100 % η_{IQE} is possible with materials that have good charge balance, high PL quantum yield and phosphorescent emission [4-6]. Thus,

$$\eta_{IQE} \leq 100\ \% \quad \text{4.3}$$

$$\eta_{EQE} \leq \eta_{out} \quad \text{4.4}$$

The two principal loss mechanisms in the OLED are (i) Substrate mode losses ~ 30 % that are due to the interface of the substrate and the anode, (ii) internal losses ~ 50-60 % due to internal waveguiding due to the mismatch of the anode and organic refractive indices (n_{anode} and $n_{cathode}$, respectively) the surface plasmon excitations loss that arises from the metal cathode [7-9].

Various innovative approaches have been developed to mitigate these losses. These include, e.g., the use of colorless polymide with air voids as scattering centers [10], subanode patterns with a scattering grid layer and a microlens array [11,12], and silver nanowire meshes in nano-imprinted PET substrates with aperiodic nanostructures [13]. Besides these, the use of photonic crystals [14], surface buckling structures [15] for mitigating plasmonic losses, etc. are also interesting approaches. More recently the use of vacuum nanohole arrays combined with an external hemispherical lens successfully demonstrated a maximal EQE of 78 % for a white PhOLED with complicated fabrication approach that is not scalable or commercializable [16]. In another work a maximal EQE of 70 % was reported for a green PhOLED (~ 50% for a white PhOLED) using a subanode microlens array with hemispherical structures trenched in glass and planarized by a high index (η ~ 1.8) spacer on which the OLED is fabricated [17]. That work, however, used the index matching fluid interfacing the substrate/photodetector that contributed to higher EQE.

In this work two-fold enhanced light extraction is reported in green PhOLEDs with a PEDOT: PSS anode on inexpensive flexible periodically patterned polycarbonate (PC) substrates with period of ~ 750 nm on shallow feature. We reported similar success on the tall feature earlier [18].

4.3 Results and Discussions:

The first section examines the merits of the bare substrate and the substrate with anode layer. The second section discusses the energetics of the OLED, its layer thicknesses, their functions and the optoelectronic characterization including enhancement phenomena. In the final section the physical basis for the enhancement is established through the remnant corrugation on the organic/cathode interface using AFM, SEM and FIB.

4.3.1 Substrate characterization

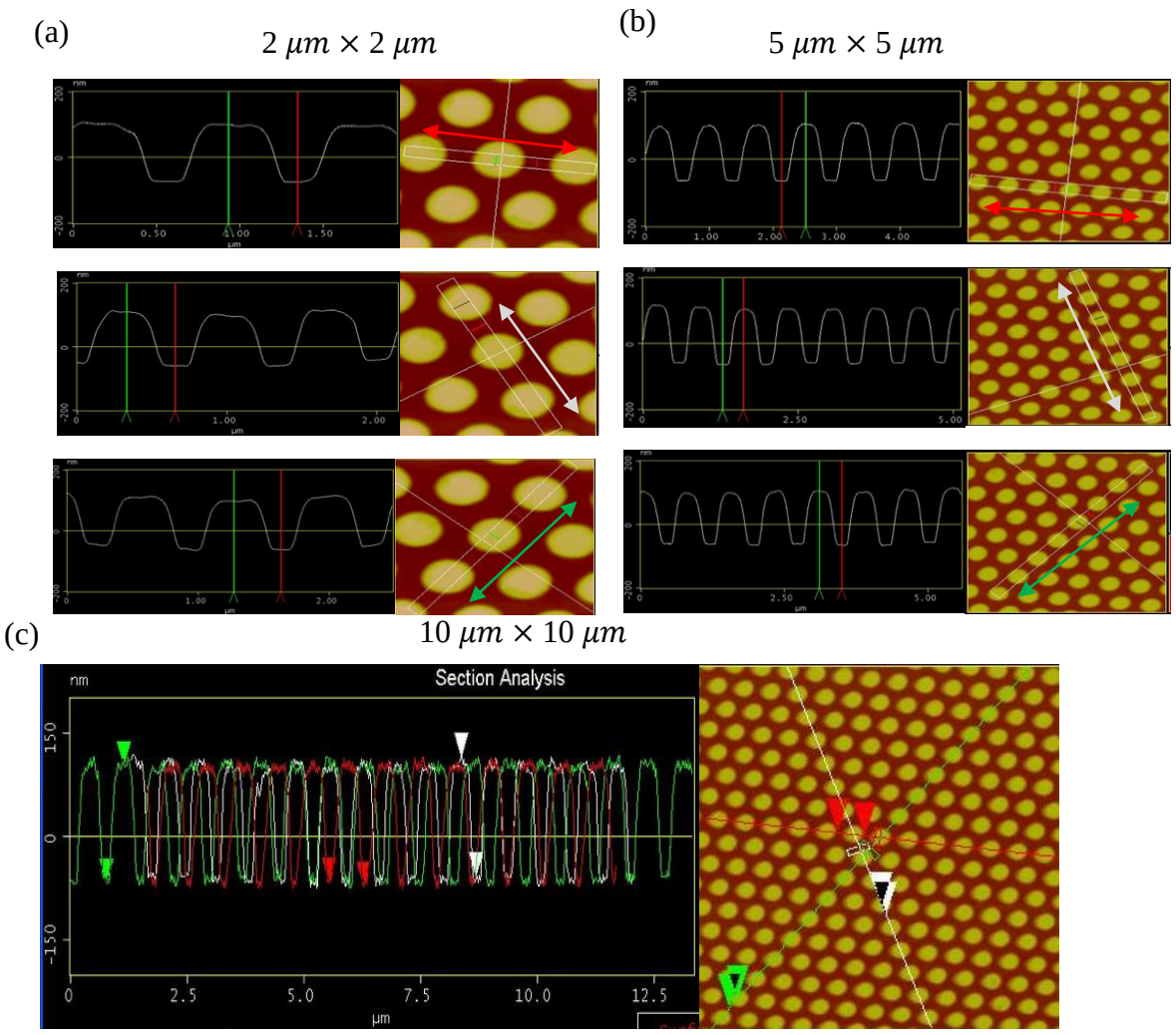

Figure 4.1: Patterned PC substrate (Shallow NREL). (a) profile and the surface on 2 μm × 2 μm, (b) profile and the surface on 5 μm × 5 μm and (c) Profile and the surface on 10 μm × 10 μm. The color of arrow on three directions among three scans are consistently chosen to show the pattern consistency.

The patterned PC substrate as shown in ***Figure 4.1*** was scanned on 2 $\mu m \times 2\ \mu m$, 5 $\mu m \times 5\ \mu m$ and 10 $\mu m \times 10\ \mu m$. Based on these images;

1. Feature as well as their array are consistent on three directions. Arrows as pointing on three different directions amongst all three scans generate surface profile that closely resembles to each other.
2. Surface as inferred from the color map is homogenous.

The corrugation attributes based on these images are summarized on ***Table 4.1***.

Table 4.1: Corrugation attributes of patterned Substrate

Scan size ($\mu m \times \mu m$)	*Height (nm)*	*Period (nm)*
2	161, 162	~ 750
5	161, 166	~752
10	171, 172	~742

4.3.2 Anode layer characterization

PEDOT: PSS, as a solution processed and spin coated layer, is the anode. From the images in ***Figure 4.2*** it is clear that the surface **smoothens** after its treatment especially on the turning points of the feature. This effect is apparent when compared to the surface of the bare substrate above. Such transformation is beneficial for the OLED stacking at the edges.

The detail corrugation attributes after its treatment is provided in ***Table 4.2***.

Table 4.2: Corrugation attributes after anode layer on patterned substrate

Scan Size ($\mu m \times \mu m$)	*Height (nm)*	*Period (nm)*
2	110, 113	~ 785
5	124, 130	~ 781
10	119, 123	~ 723
25	117, 126	~ 732

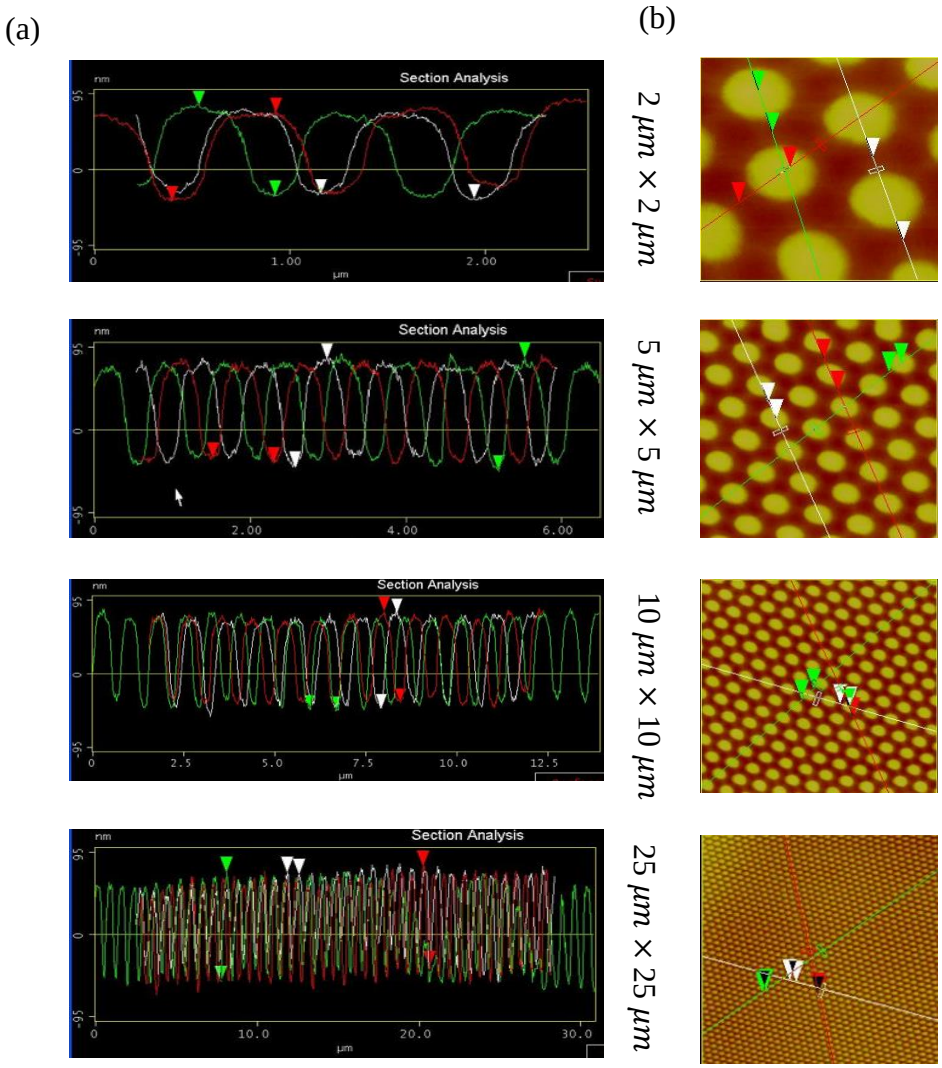

Figure 4.2: Patterned PC after anode treatment (a) Surface profile on various scans and (b) The surface of these profiles

4.3.3 Green PhOLED Energetics

Device is stacked as*: HAT-CN (5 nm)/10% MoO_x: TAPC (60 nm)/ TAPC (20 nm)/ 6%*

$Ir(ppy)_3$: mCP (20 nm)/ TmPyPB (20 nm)/ 20% CsF: TmPyPB (40 nm)/LiF (1 nm)/Al (100 nm)

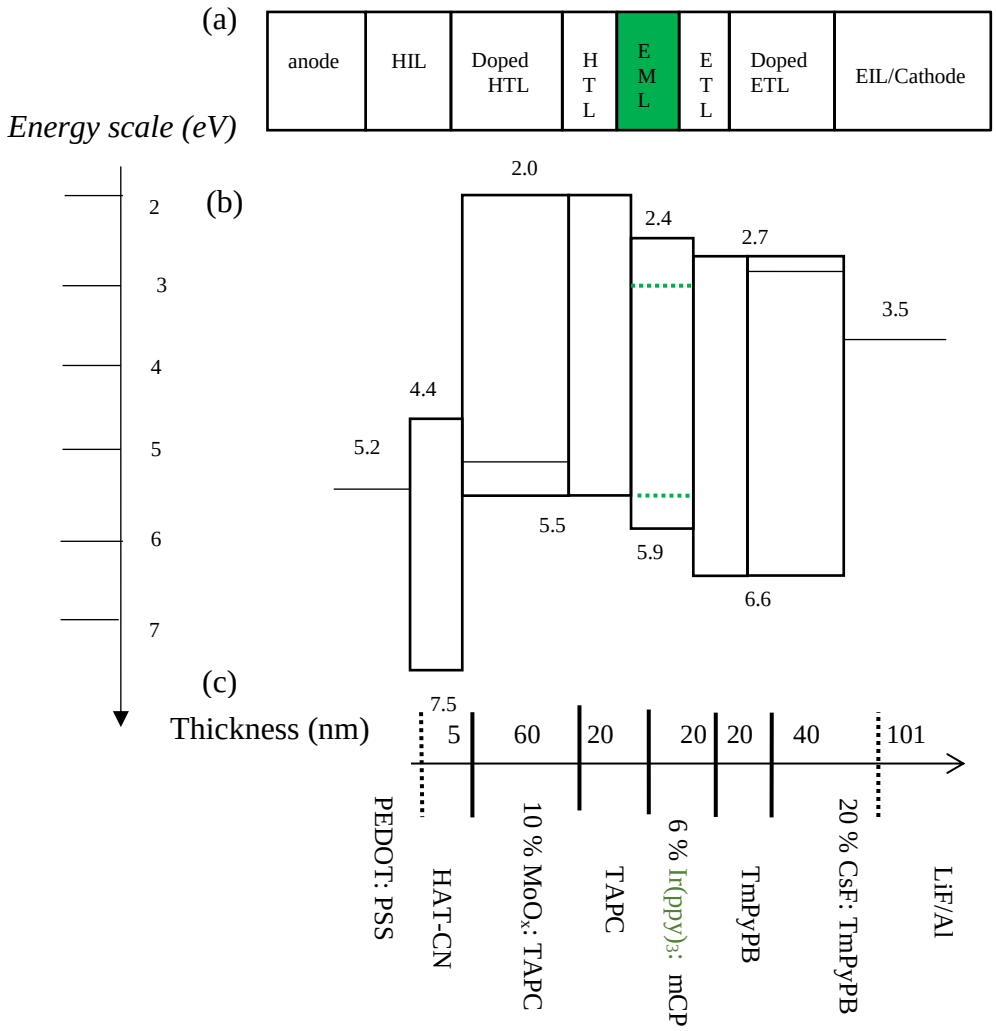

Figure 4.3: Green PhOLED (a) functional role of each layer, (b) Energy band diagram with HOMO/LUMO value (values are negative relative to vacuum which is zero) and (c) the molecules on the stack and their thicknesses.

Energy band gap an intrinsic property of the molecules, is measured in electron Volt (eV) and is negative since it is measured with respect to vacuum which is taken as zero. In organic molecules it is the energy difference between the **L**owest **U**noccupied **M**olecular **O**rbital (LUMO) and the **H**ighest **O**ccupied **M**olecular **O**rbital (HOMO) as shown in ***Figure 4.3*** **(b).**

Hole Injection layer (HIL)**:** 5 nm of 1,4,5,8,9,11- Hexaazatriphenylenehexacarbonitrile (HAT-CN).

Function: To efficiently inject hole from anode towards HTL once field is applied.

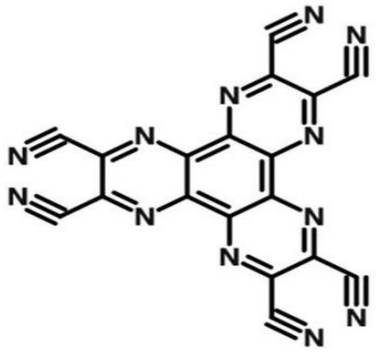

Figure 4.4: HAT-CN molecule [19]

***Doped Hole Transport layer (D.HTL)*:** 60 nm thick molybdenum oxide (MoO_x) doped on 1,1-bis[(di-4-tolylamino) phenyl] cyclohexane (TAPC).

Function: To reduce the resistance to the left of EML of the OLED stack, promote hole mobility towards EML.

Hole Transport layer (HTL): Neat 20 nm thick TAPC layer.

Function: To separate emissive layer (EML) from doped HTL layer. Reduces exciton quenching & also promotes hole mobility towards EML.

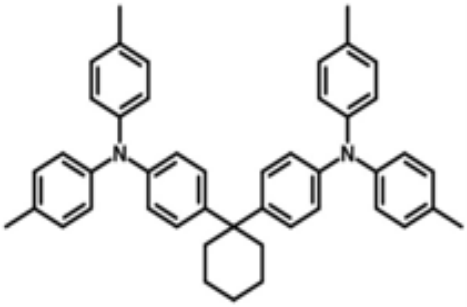

Figure 4.5: TAPC molecule [19]

***Emissive layer (EML)*:** 20 nm of 6% fac-tris(2-phenylpyridine) iridium (III) ($Ir(ppy)_3$) in 1,3-bis(carbazol-9-yl) benzene (mCP).

Function: To provide physical space for the recombination; hole and photon, giving rise to electroluminescence.

(a) (b)

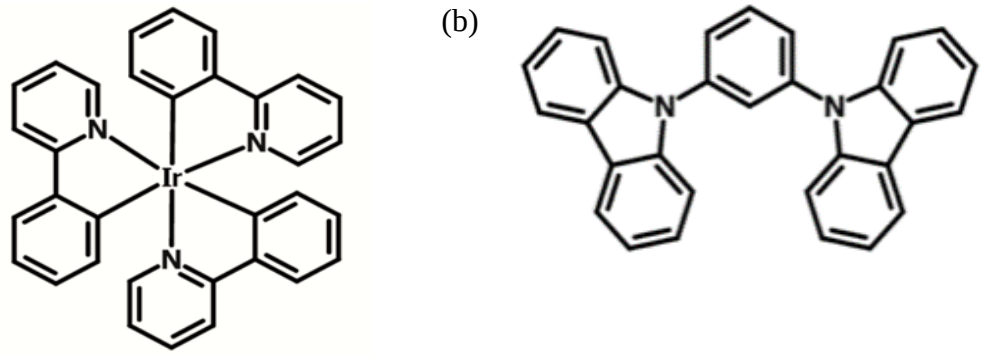

Figure 4.6: (a) $Ir(ppy)_3$ molecule and (b) mCP molecule [19]

Electron Transport layer (ETL): 20 nm of 1,3,5-tri[(3-pyridyl)-phen-3-yl] benzene (TmPyPB).

Function: To promote electron transport toward EML. Also reduces quenching, acts as a spacer layer between the doped ETL and EML.

Doped Electron Transport layer (D.ETL): 40 nm of 20 % Cesium Fluoride (CsF) doped on TmPyPB.

Function: To act as a spatial barrier between the metal cathode and the EML. Reduces plasmon losses and lowers resistance to the right of EML.

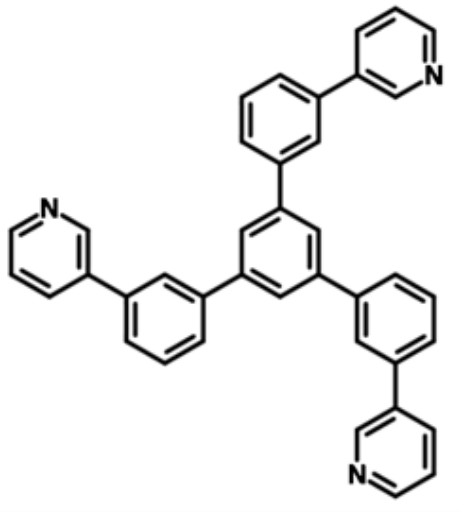

Figure 4.7: TmPyPB molecule [19]

Electron Injection layer (EIL):1 nm of Lithium fluoride. *Function*: To reduce barrier for electron injection from the Al cathode to the ETL.

***Cathode*:** 100 nm of Aluminum

4.3.4 Optoelectronic characterization

4.3.4.1 Current density, Luminance (Brightness), and Voltage (*J*-*L*-*V*) plots

Figure 4.8 shows the current density *J* and the luminance (brightness) *L* of the OLED as a function of the voltage *V*. *J*(*V*) plot is a typical diode curve. This curve is representative of the electrical power that the device consumes. The brightness curve on other hand describes the optical behavior resulting from the generation of photons in the device and their propagation into the forward hemisphere. The *L*(*V*) curve shows a turn on voltage (*V* at which $L = 1$ cd/m^2) ~ 2.9 V demonstrating an OLED with a low ohmic resistance in general, a low trap-limited current in particular, and energy alignment between the layers is suitable for charge transport.

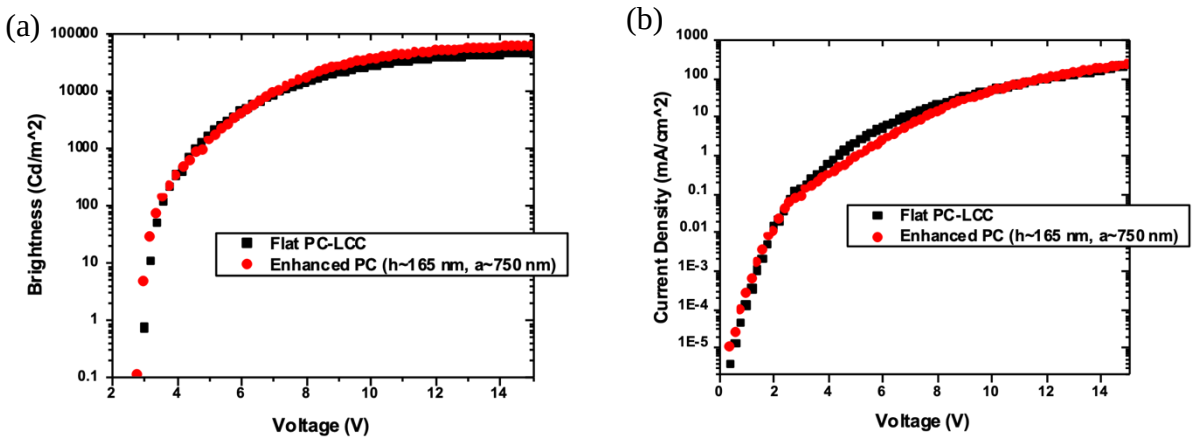

Figure 4.8: Plot (a) Brightness(L) vs Voltage(V), (b) Current density(J) vs. Voltage(V)

4.3.4.2 Luminous (Current) Efficiency (η_L)and Power efficiency (η_P) plots

As per luminous and power efficiencies in ***Figure 4.9*** the corrugated OLED is twice as efficient as its control. Power efficiency plot, more representative of the voltage dependence, implicate that both the devices has minimal resistance issue. As the "roll off" (the decline in the efficiency at higher voltage) onsets at higher brightness, the devices are robust and stable. The luminous efficiency peaks at ~ 3,900 nits for the corrugated and 4,500 nits for flat. Similarly, the power efficiency peaks at ~ 1,000 nits for both the devices.

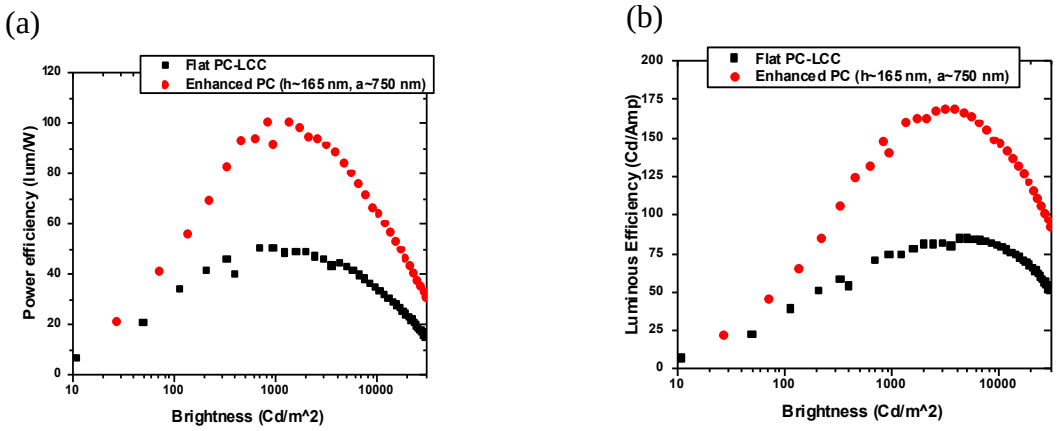

Figure 4.9: Plot (a) Power efficiency (η_P) vs L, (b) Luminous efficiency (η_L) vs L

4.3.4.3 EL Spectra and EQE plots.

EQE as calculated by ***Eqn 4.5*** shows 2-fold enhancement with respect to its control as shown in ***Figure 4.10*** (b). Based on ***Eqn 4.3 & 4.4*** it can be inferred that the light outcoupling from the enhanced OLED exceeds 48%. The EL spectrum of the OLEDs peaks at 512 nm as in ***Figure 4.10*** (a), as expected for $Ir(ppy)_3$. EQE is determined from the relation [20]:

$$\eta_{EQE} = \frac{\pi e \eta_L}{k_m h c} \frac{\int g(\lambda)\lambda d\lambda}{\int g(\lambda)k(\lambda)d\lambda} \qquad \text{.....4.5}$$

where

(i) $g(\lambda)$ is the normalized intensity from EL spectrum

(ii) $k(\lambda)$ is the normalized photopic response intensity

(iii) η_L is the Luminous Efficiency

(iv) k_m is a constant with value of 683 [lumen/Watt]

(v) h is Planck constant; c is speed of light and e is the charge of an electron

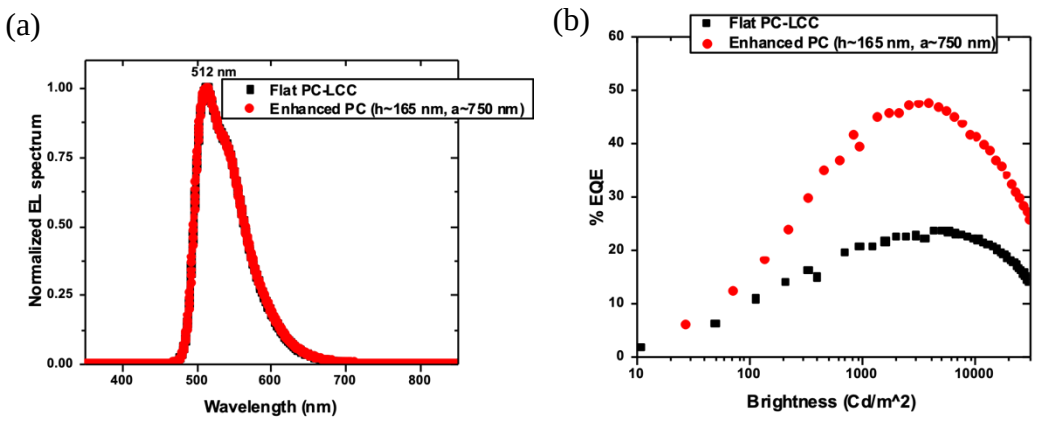

Figure 4.10: Plot (a) Normalized EL vs wavelength (λ) (b) EQE vs. L

Table 4.3: Summary of various efficiencies of enhanced vs. flat OLEDs

Device *Efficiency*	*Patterned (1,000 nits)*	*Flat (1,000 nits)*	*Enhancement (1,000 nits)*	*Patterned (peak nits)*	*Flat (peak nits)*
External Quantum Efficiency (%)	41	21	$\times$ **2.0**	48 (3,882)	24 (4,484)
Luminous Efficiency (Candela/Amp)	150	87	$\times$ **1.7**	170 (3,844)	77 (4,528)
Power Efficiency (lumen/Watt)	101	51	$\times$ **2.0**		

Bold figure is the effciency ratio of patterned to the flat
Peak power efficiency is at ~ 1,000 nits; $1\ nit = 1\ Cd/m^2$

4.3.5 Corrugation approach

Corrugation as an approach for mitigating internal losses within the OLED requires its retention throughout the device stack till organic/cathode interface [20]. The finding of residual corrugation at the organic/cathode interface is the direct physical evidence on the effectiveness of this approach.

4.3.5.1 AFM

Two set of images on ***Figure 4.11*** correspond to the corrugated substrate at three stages. In the array, bottom is the bare substrate followed by the substrate coated with anode and finally the organic/cathode interface in the OLED. This set of images clearly capture the evolution of the corrugation. The corrugation which is subtle in its final stage, still provide the evidence of it reaching till the metal cathode that successfully mitigate the internal losses.

As shown in ***Figure 4.12(a),*** the remnant corrugation is ~ 30 nm on the interface. The period of the pattern is ~ 758 nm. This observation is backed up by the retention of the period ~ 746 nm ($8.212\ \mu m\ \div 11$) from 10 μm × 10 μm as in ***Figure 4.13 (b).***

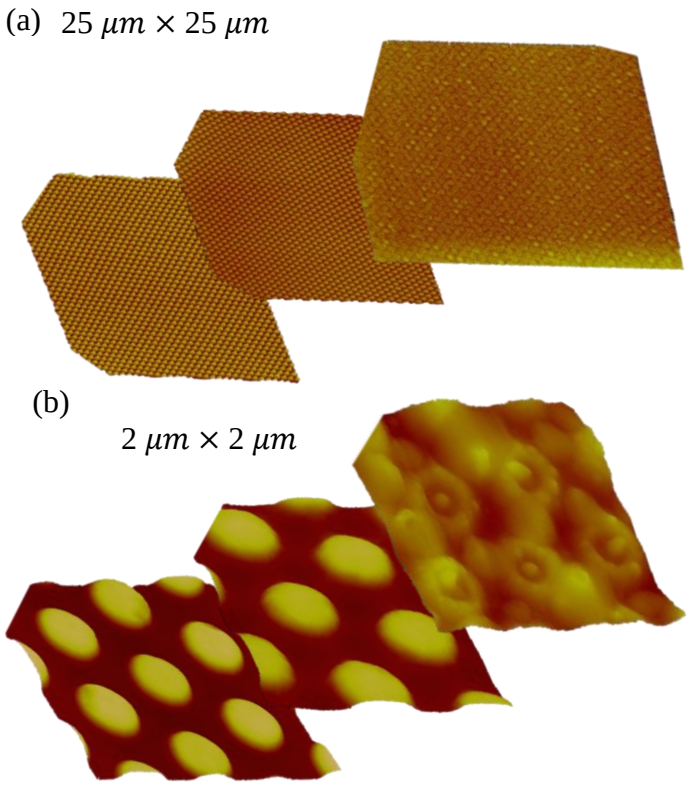

Figure 4.11: AFM images (a) (25 μm × 25 μm) on progressive stage as the corrugated surface: bare substrate, substrate after anode coating; organic/cathode interface(b) (2 μm × 2 μm) on the same order as in (a)

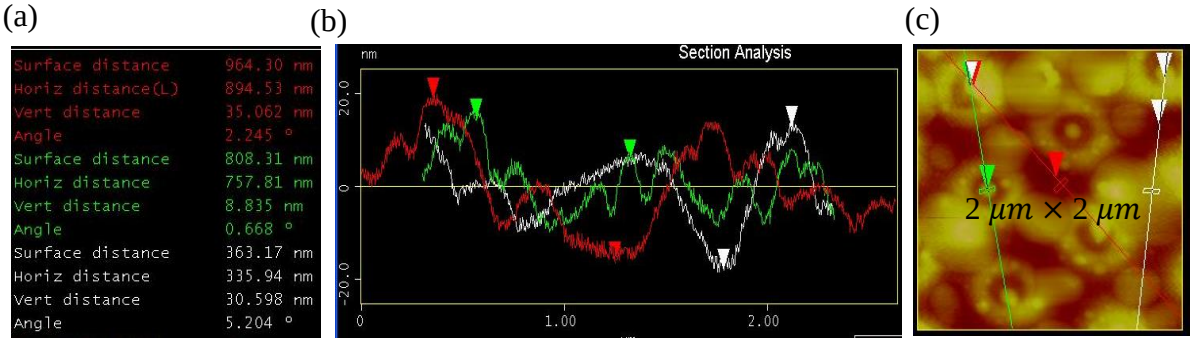

Figure 4.12: AFM image (2 μm × 2 μm)at organic/cathode interface; (a) Height/period measurement, (b) surface profile, (c) surface

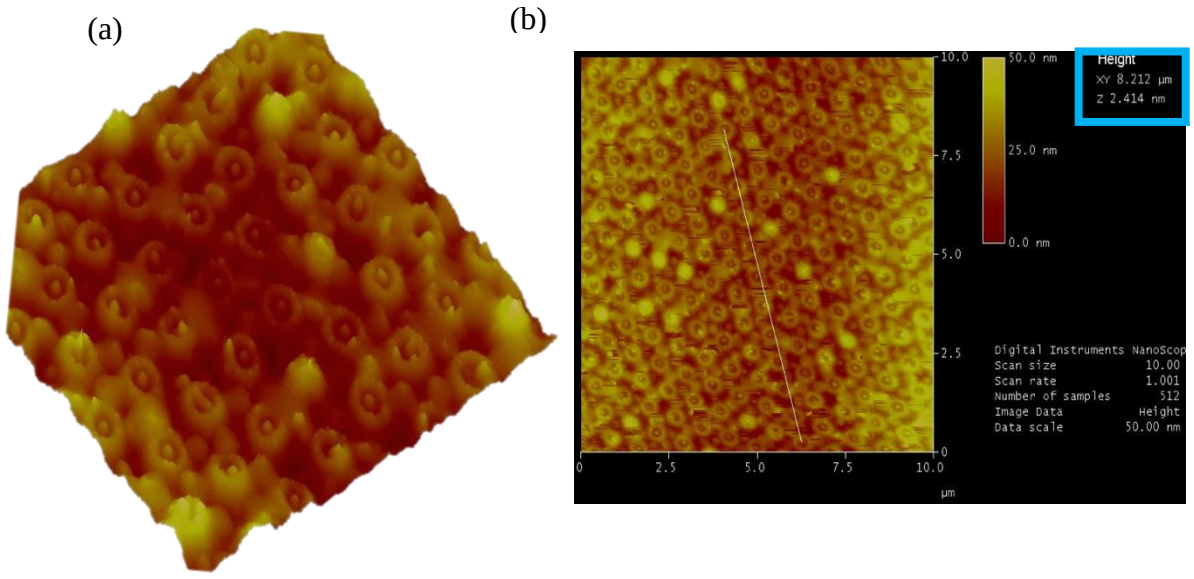

Figure 4.13: Organic/cathode interface; (a) 3D image on 5 µm × 5 µm, (b) surface profile 10 µm × 10 µm white line corresponds to 11 periods.

4.3.5.2 SEM

***Figure 4.14*(a)** corresponds to the organic/cathode interface of the corrugated OLED as probed by secondary electrons SEM. The slight streak in the image is due to the charging of the LiF, which is the topmost layer on the surface.

***Figure 4.14*(b)** is the SEM image for the top surface of the OLED, which is the 100 nm Al cathode. The corrugation is brighter here as the metallic surface is conductive opposed to the insulating surface in ***Figure 4.14*(a).**

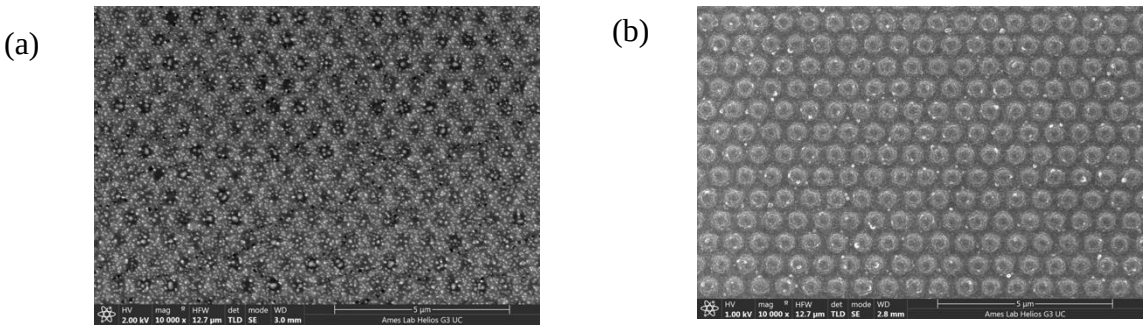

Figure 4.14: SEM image of the (a) organic/cathode interface & (b) Aluminum surface

4.3.5.3 FIB cross section analysis

FIB image as shown in ***Figure 4.15*** provides a cross sectional view of the OLED layers. Another advantage of the FIB image is to see the progress of the corrugation as the stacking of the layer progresses. Conformal layers refer to the retention of the layer thickness in the z (OLED fabrication) direction which is also the direction for the charge flow. Clearly, a conformal stack is a necessary (but not sufficient) condition for uniform current density over the surface of the device. The layers are conformal and as seen on the background the corrugation made its way till cathode.

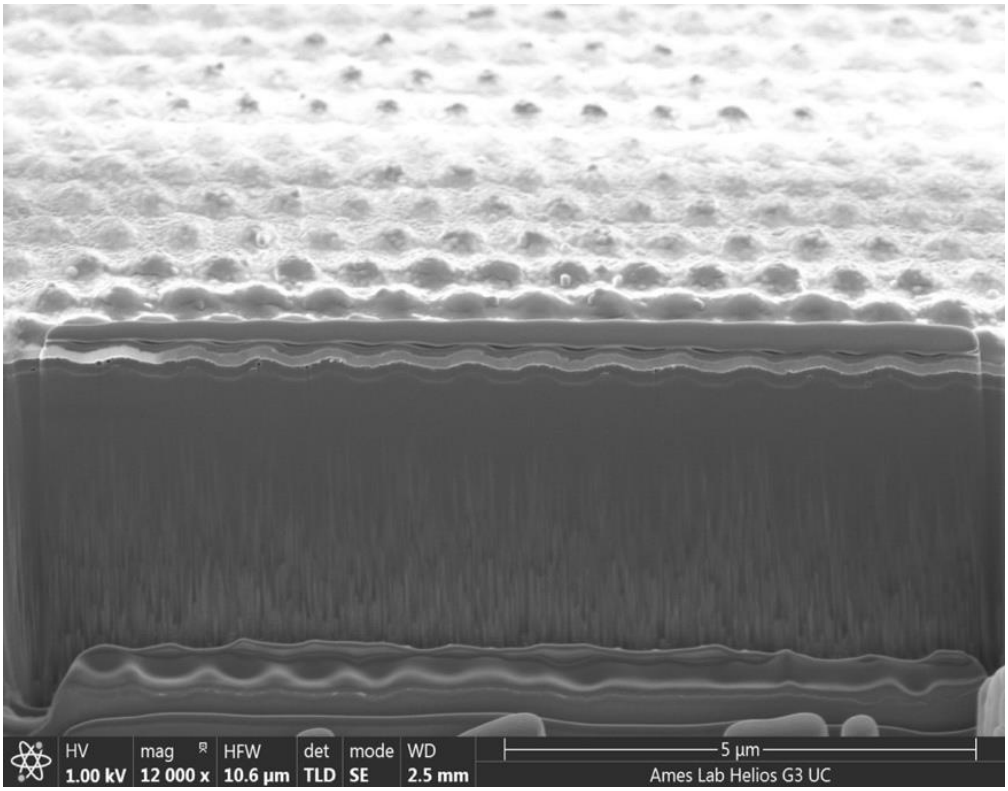

Figure 4.15: FIB image showing conformal OLED stack and top corrugation

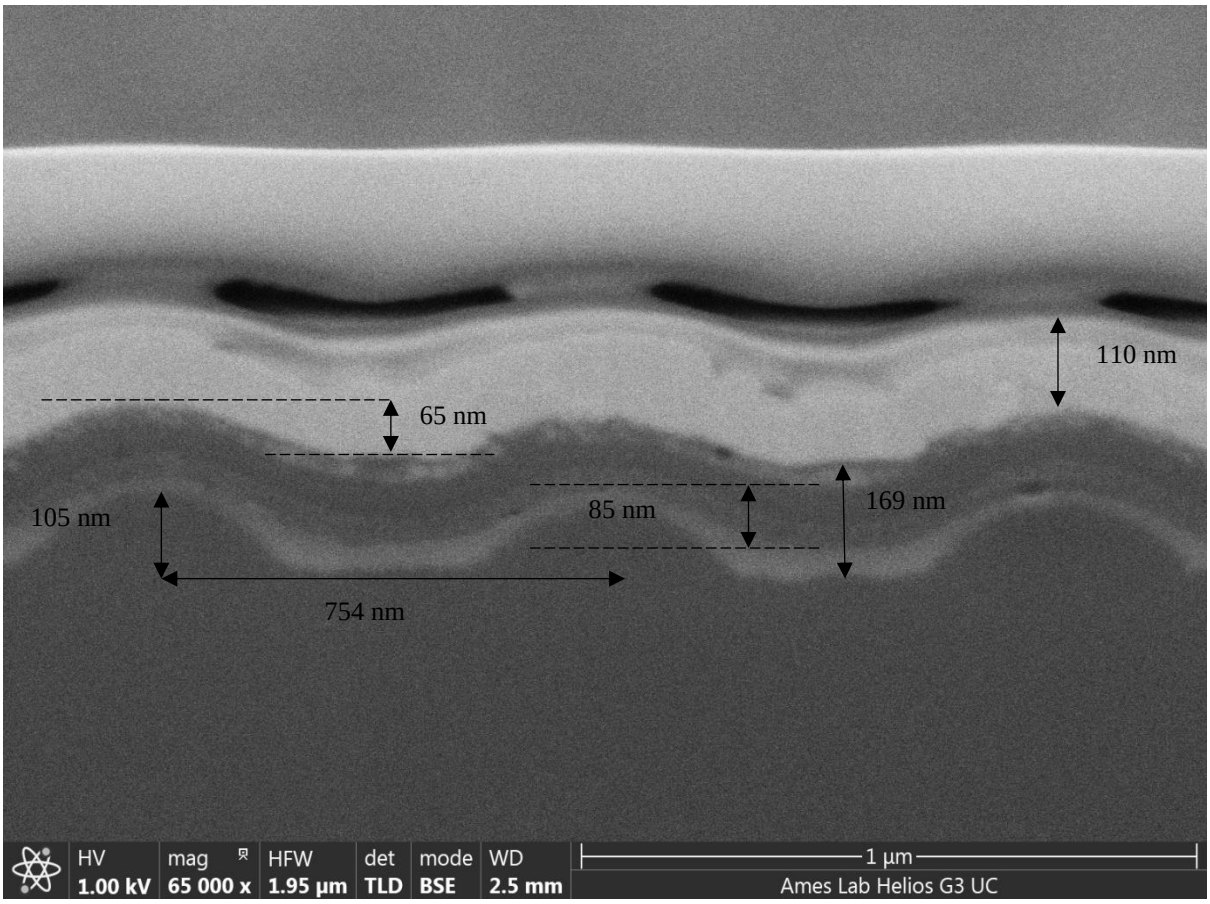

Figure 4.16: FIB cross section analysis. Values depicted are summarized on ***Table 4.4****.*

Table 4.4: Summary of FIB measurement ***(Figure 4.16)***

Physical Attributes	*FIB-Metric (nm)*
Corrugation-Height	105
Corrugation- Pitch	754
Valley of Corrugation to organic/Aluminum Interface	169
Cathode (Aluminum)	110
Residual corrugation on organic/Aluminum Interface	65
Corrugation intact after PEDOT: PSS layer	85

The FIB image analysis as depicted in ***Figure 4.16*** and tabulated on ***Table 4.4*** provide following information:

i. The corrugation height is ~105 nm as opposed to the AFM measurement of ~ 165 nm. This is highly likely due to FIB milling being on the slope of the feature.

ii. The anode layer, the first layer with bright contrast, shows some variation in thickness, especially at the crests and troughs of the surface. The height retained after adding anode layer is ~ 85 nm.

iii. As per the quartz crystal thickness monitor located in the thermal evaporation chamber, which is used to control the layer thickness during device fabrication, the cumulative thickness of organic layers is ~ 166 nm; the measured FIB thickness ~ 130 nm. The discrepancy in the thickness could be ascribed again to FIB milling missing the surface peaks.

iv. The remnant corrugation on the organic/cathode interface is ~ 65 nm.

v. OLED stacking is somewhat conformal, though certainly not rigorously so.

4.4 Conclusions and Future work

Successful devices leading to enhanced light extraction using corrugated surfaces are not a coincidence. There are several factors that yield a successful enhanced device. The primary factors are:

1. ***Substrate****:* The light extracting substrate has to be clean of impurities/defects with a smooth pattern devoid of sharp edges. Defects and imperfections jeopardize charge balance, and sharp structures, are detrimental by generating regions of high electric fields, leading to catastrophic shorts. The substrate features, i.e., the pitch and height, are

similarly important factors, determining the OLED's EQE and the conformality of the complete stack.

2. ***Anode:*** The quality of the anode, surface smoothness and conductivity, is obviously critical for device performance. The anode used in this study was mostly solution-processed PEDOT: PSS. While we obtained significant light outcoupling enhancements using this anode, spin coating is currently not the preferred industrial approach. Spin coating on patterned substrates with low pitch and high features adversely affects the conformality of the OLED stack. Sputtered ITO on corrugated plastic, which is currently under development, is challenging due to the instability of the plastic at high temperatures, which entails low temperature deposition and hence potentially lower quality ITO, deteriorates the device performance. Together with the ongoing development of quality ITO on patterned plastic, future work aims at fabricating an integrated transparent substrate that includes additionally a metal mesh for uniform current spreading as well as a microlens array at the air side of the substrate to extract the substrate mode loss.

3. ***OLED design:*** The energetics of the OLED layers should obviously be optimal, minimizing quenching and other loss mechanisms. This entails optimization; of each layer's material (optimal charge mobility and dopant level) and thickness. As an example, a thick ETL will minimize plasmon excitation loss, however, to minimize the layer's resistance, thick layers should be doped. To minimize exciton quenching by dopants the emissive layer has to be optimally separated from a doped layer as well as at a suitable distance from the electrode.

4. ***OLED fabrication condition:*** A base pressure $< 10^{-6}$ m bar was used for the thermal evaporation of the organic layers. Additionally, all the layers were deposited at an optimized rate. In the case of doped layers, where co-evaporation is required, the rate was carefully adjusted to avoid non-uniformity.

Ongoing studies include fabrication of conformal enhanced white OLEDs needed for solid-state lighting.

4.5 Experimental procedure

4.5.1 Materials

The flat and patterned PC substrates were fabricated by MicroContinuum, Inc. The conductive polymer PEDOT: PSS, used as the anode, was from Heraues, Clevios. LiF was from Sigma-Aldrich. MoO_3 was from Sterm Chemicals, and HAT-CN, TAPC, TmPyPB, mCP, $Ir(ppy)_3$ were from Luminescence Technology Corporation.

4.5.2 AFM characterization

Veeco Metrology Scanning Probe Microscopy is the scanner used. The AFM tip model was TESPA-V2; tips were purchased from Bruker Company (brukerafmprobes.com). These tips are made of Antimony- (n) doped Si with a resistivity of 0.01-0.025 Ohm-cm. They have a resonant frequency of 320 kHz and spring constant of 42 N/m. The tips were 125 μm long and 40 μm wide without any coating on the front side, whereas the backside has 50±10 nm Al.

4.5.3 PEDOT: PSS film fabrication and characterization

The PEDOT: PSS solution was mixed with 6 v% EG and 1 v% Capstone FS35 fluorosurfactant. The mixed solution was filtered using a 0.45 μm syringe filter; it was spin-coated at 6000 rpm for 30 s (optimized). This was followed by annealing the film at 120ºC for 2 h. The morphology of the films was obtained by AFM (TESPAV2) employing tapping mode.

4.5.4 FIB Imaging

For analysis of the OLED structure and stack conformality we used a FEI Helios Dual Beam FIB/SEM system that combines milling, imaging, and analytical capabilities. The system enables very precise ion milling in selected areas as well as high-resolution 3-D microscopy. A beam of gallium ions is used for nm milling and imaging precision, depending on the ion energy and intensity; the Ga^+ ion source can image and machine down to 5 nm resolution levels. Image J software was used for determining features in the FIB image.

4.5.5 OLED fabrication and characterization

OLEDs were fabricated on the PEDOT: PSS-coated corrugated and flat plastic substrates. The Al cathode and all organic materials were deposited by thermal evaporation inside a chamber with a base pressure of $<10^{-6}$ mbar within a glovebox. The Al cathode was deposited through a shadow mask containing 1.5 mm diameter circular holes. Characterization of the OLEDs was done using a Keithley 2400 source meter to apply a voltage and measure the current. The brightness was measured by a Minolta LS110 luminance meter and the EL spectra were obtained using an Ocean Optics PC2000-ISA spectrometer. Labview software was used to calculate the efficiencies from the experimental data.

4.6 References

[1] https://www.energy.gov/sites/prod/files/2019/01/f58/ssl_rd-opportunities_jan2019.pdf

[2] Shinar, J. (2004). *Organic light-emitting devices: A survey / Joseph Shinar, editor.* New York: AIP Press/Springer.

[3] Kim, J., Ho, Greenham, & Friend. (2000). Electroluminescence emission pattern of organic light-emitting diodes: Implications for device efficiency calculations. *Journal of Applied Physics, 88*(2), 1073-1081.

[4] Baldo, M.A., O'Brien, D.F.,You, Y., Shoustikov, A., Sibley, S., Thompson, M.E., Forrest, S.R. (1998). *Nature 395* (151)

[5] Baldo, M.A., Lamansky, S., Burrows, P.E., Thompson, M.E., Forrest,S.R., (1999) *Appl. Phys. Lett. 75* (4).

[6] Tsutsui, T., Yang, M-J., Yahiro, M., Nakamura, K., Watanabe, T., Tsuji, T., Fukuda,Y., Wakimoto, T., Miyaguchi, S., (1999) *Jpn. J. Appl. Phys.* (*38*) L1502.

[7] Madigan, C., Lu, & Sturm. (2000). Improvement of output coupling efficiency of organic light-emitting diodes by backside substrate modification. *Applied Physics Letters, 76*(13), 1650-1652.

[8] Meerheim, R., Furno, Hofmann, Lüssem, & Leo. (2010). Quantification of energy loss mechanisms in organic light-emitting diodes. *Applied Physics Letters, 97*(25), Applied Physics Letters, 20 December 2010, Vol.97(25)

[9] Furno, M., Meerheim, R., Hofmann, S., Lüssem, B., & Leo, K. (2012). Efficiency and rate of spontaneous emission in organic electroluminescent devices. *Physical Review B, 85*(11), Physical Review B, 3/2012, Vol.85(11).

[10] Koh, T., Spechler, J., Lee, K., Arnold, C., & Rand, B. (2015). Enhanced Outcoupling in Organic Light-Emitting Diodes via a High-Index Contrast Scattering Layer. *ACS Photonics, 2*(9), 1366-1372.

[11] Sun, Y., & Forrest, S. (2008). Enhanced light out-coupling of organic light-emitting devices using embedded low-index grids. Nature Photonics, 2(8), 483-487.

[12] Qu, Y., Slootsky, M., & Forrest, S. (2015). Enhanced light extraction from organic light-emitting devices using a sub-anode grid. *Nature Photonics, 9*(11), 758-763.

[13] Zhou, Lei, Xiang, Heng-Yang, Shen, Su, Li, Yan-Qing, Chen, Jing-De, Xie, Hao-Jun, Goldthorpe, Irene A, Chen, Lin-Sen, Lee, Shuit-Tong, and Tang, Jian-Xin. (2014). High-performance flexible organic light-emitting diodes using embedded silver network transparent electrodes. *ACS Nano, 8*(12), 12796-12805

[14] Ishihara K et al (2007) Organic light-emitting diodes with photonic crystals on glass substrate fabricated by nanoimprint lithography. *Appl Phys Lett 90*(11):111114

[15] Koo WH et al (2010) Light extraction from organic light-emitting diodes enhanced by spontaneously formed buckles. *Nat Photonics 4*(4):222–226

[16] Jeon, Sohee, Lee, Sunghun, Han, Kyung-Hoon, Shin, Hyun, Kim, Kwon-Hyeon, Jeong, Jun-Ho, & Kim, Jang-Joo. (2018). High-Quality White OLEDs with Comparable Efficiencies to LEDs. *Advanced Optical Materials, 6*(8), 1-8.

[17] Qu, Y., Kim, J., Coburn, C., & Forrest, S. (2018). Efficient, Nonintrusive Outcoupling in Organic Light Emitting Devices Using Embedded Microlens Arrays. *ACS Photonics*, *5*(6), 2453-2458.

[18] Hippola, Chamika, Kaudal, Rajiv, Manna, Eeshita, Xiao, Teng, Peer, Akshit, Biswas, Rana, Slafer, Warren Dennis, Trovato, Tom, Shinar, Joseph, Shinar, Ruth. (2018). Enhanced Light Extraction from OLEDs Fabricated on Patterned Plastic Substrates. *Advanced Optical Materials*, *6*(4), 1-11.

[19] https://www.ossila.com/pages/oled

[20] Li, Huiying, Zhang, Changhai, Li, Dechang, & Duan, Yu. (2007). Simulation of transform for external quantum efficiency and power efficiency of electroluminescent devices. *Journal of Luminescence*, *122*(1-2), 626-628.

[21] Salehi, A., Fu, X., Shin, D., & So, F. (2019). Recent Advances in OLED Optical Design. *Advanced Functional Materials*, *29*(15), 1-21.

CHAPTER 5. LIGHT EXTRACTION FROM SIMPLE WHITE OLED ON MICROPATTERNED PET SUBSTRATE

5.1 Abstract

This chapter focuses on fabrication of a white OLED (WOLED) on a micro-patterned (rather than nano-patterned) plastic substrate; a new approach of testing a different type of substrates for enhancing OLEDs light outcoupling. A WOLED based on only-orange and blue emitting dyes was fabricated on a flexible polyethylene terephthalate/Cellulose acetate butyrate (PET/CAB) substrate with a large aspect ratio of 25:1 (period~ 7.8 μm; height~ 320 nm). A two-fold enhancement in the EQE with a fully conformal OLED stack was obtained, indicating that high aspect ratio substrates present a viable approach towards enhancing light outcoupling in OLEDs, which is crucial for advancing OLED-based solid-state lighting. The WOLED, as gauged by Focused Ion Beam (FIB), was fully conformal up to the metal cathode. The top OLED surface was probed additionally via Scanning Electron Microscopy (SEM) as well as Tapping Mode Atomic Force Microscopy (AFM), both techniques showing unchanged top corrugation.

5.2 Introduction

Solid state lighting is undergoing a major paradigm shift as lighting nowadays focuses more on advancing quality, compatibility with the environment, and achieving a flexible thin form factor [1,2]. OLED lighting is already in the forefront of this shift that is of great interests for both scientific and industrial communities, especially due to OLEDs' lighting quality. OLED light is devoid of glare, is uniform, and of excellent contrast, hence it is suitable for indoor lighting, including in hospitals and workplaces [3-6]. Being lightweight and ultrathin, OLEDs can be made on plastic or paper and thus are amenable for roll-to-roll (R2R) manufacturing [7].

Ever since the first WOLED was made on by Kido and coworkers in 1993 in Japan, continual effort has been made to generate cheaper as well as more efficient and stable WOLEDs for lighting applications [8]. Various schemes, such as striped WOLEDs, fluorescent/phosphorescent (F/P) WOLEDs, and stacked, or tandem WOLEDs were developed [1,2]. The later design is most effective in achieving longer lifetime and high brightness however, it requires several OLED stacks and hence is not cost-effective [2]. Recent reports on efficient WOLEDs employed costly or complex fabrication process, such as generating a vacuum nanohole array, or a sub-anode microlens array of hemispherical structures trenched in glass and planarized by a high index (n ~ 1.8) spacer; all potentially of high cost for upscaling [9,10].

Generating simple and inexpensive designs that lead to higher efficiency WOLEDs seems challenging, since white color generation typically requires three separate monochrome dyes viz., red, green, and blue, with the blue having a shorter life time, which is a major constraint in such design.

This study resorts to a simpler scheme of mixing orange and blue dyes as reported by Zhou et al. and fabricating an WOLED on a corrugated PET substrate, which can be made using inexpensive R2R [11]. WOLEDs on such a substrate demonstrated two-fold enhanced light extraction compared to a device on a flat PET. This establishes the substrate's micro-corrugation as a viable approach for mitigating losses due to internal waveguiding and surface plasmon excitation in OLEDs [12].

5.3 Results and Discussions:

This section is divided into two parts. The first part deals with the design as well as the characterization of the substrate and the simple WOLED with emphasis on key elements such as,

efficiency and substrate attributes. The second part provides evidence for the success of the substrate patterning approach.

5.3.1 Substrate Characterization

NIM 31 pattern as shown in ***Figure 5.1*** is the surface of concave square array with its profile sinusiodal. The surface is homogenous based on the color map in particular on the larger scan as in ***Figure 5.1(b).*** The corrugation attributes of the pattern is on ***Table 5.1.***

(a)

(b)

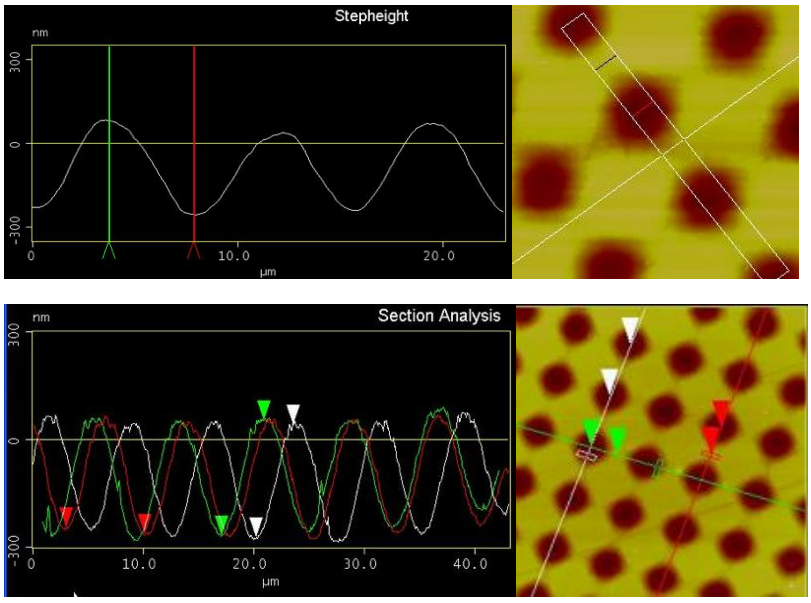

Figure 5.1: NIM 31 substrate, (a) surface profile and the surface (20 µm × 20 µm), (b) surface profile and the surface (40 µm × 40 µm).

Table 5.1: Corrugation attributes of NIM 31 substrate

Scan area (µm × µm)	*Period (µm)*	*Height (nm)*
20	7.8	330
40	7.8	320

5.3.2 Simple Structure

The WOLED structure was: *PEDOT:PSS/HAT-CN (5 nm)/10 % MoO_x:TAPC (120 nm)/TAPC (20 nm)/8% FIrpic:mCP (19 nm)/6% PO-01:mCP (1 nm)/20 % CsF:TmpyPB (40 nm)/TmPyPb (20 nm)/LiF (1 nm)/Al (100 nm).*

WOLEDs were fabricated by mixing orange and blue emitting materials. The blue dye is FIrpic and orange dye is PO-01. The molecular structure of the materials, the energy diagram of the device, and the electroluminescence (EL) spectrum are presented in ***Figure 5.2.***

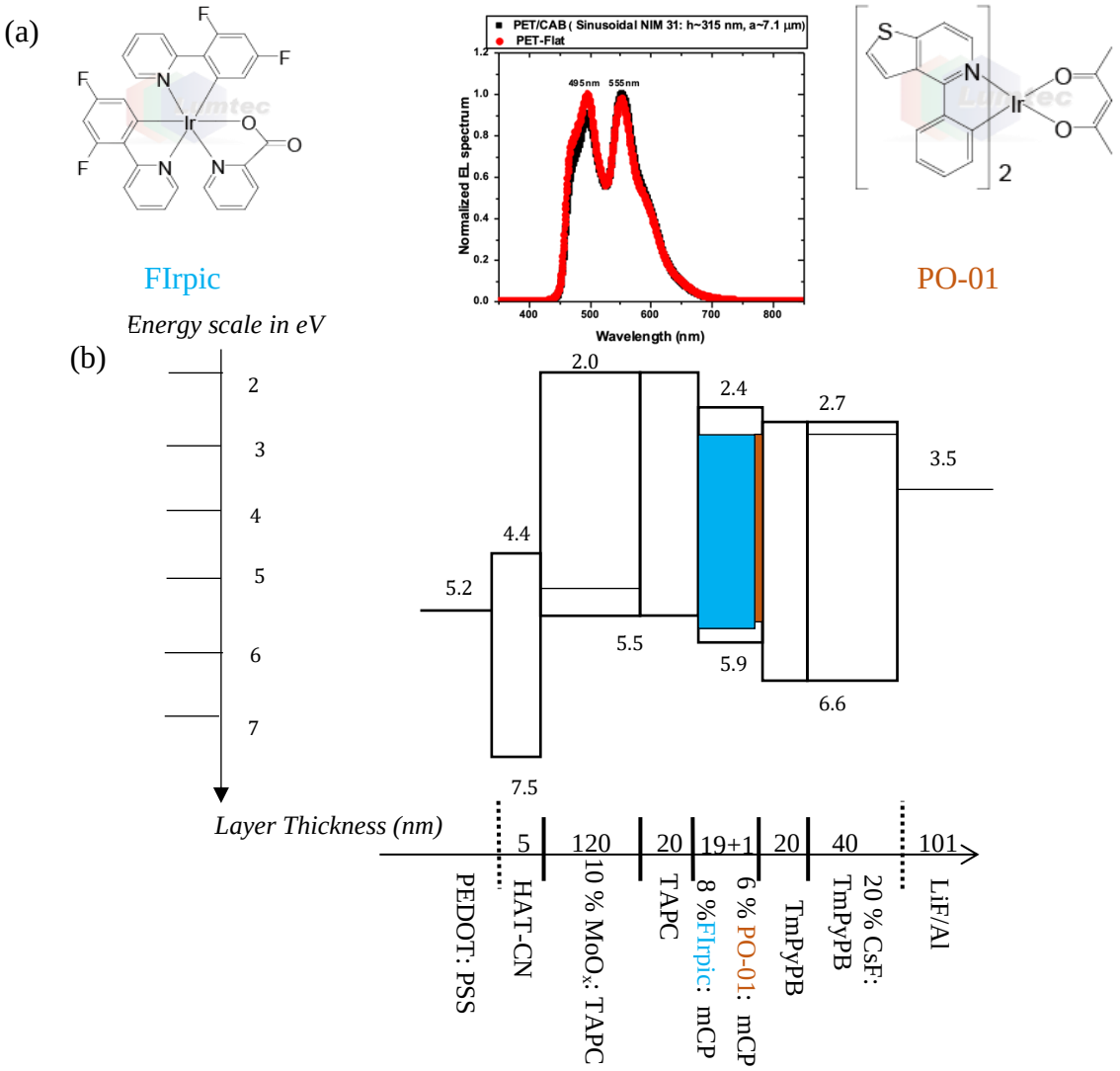

Figure 5.2: WPOLED (a) Normalized EL spectrum with molecular structure of FIrpic and PO-01[13], (b) Energy band diagram with HOMO/LUMO value of organic layers; Energy value is negative with respect to vacuum whose value is taken as zero (c) Layer thicknesses.

5.3.3 Opto-electronic Charactization

Figure 5.3 provides the curve of Current density (*J*) and Luminance/Brightness (*L*) as a function of the Voltage (*V*) applied to the OLED. *J-V* curve is the diode curve. *L-V* curve shows that the OLED on patterned PET is consistently brighter than the refernce device. The turn on voltage (Voltage @ 1Cd/m^2) for the devices is ~2.9 V.

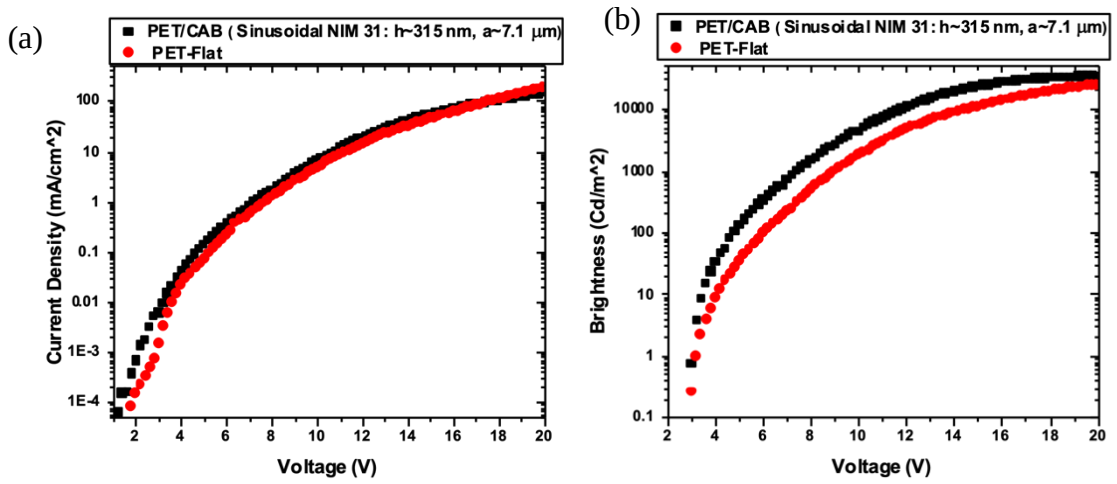

Figure 5.3: (a) J-V curve; (b) L-V curve

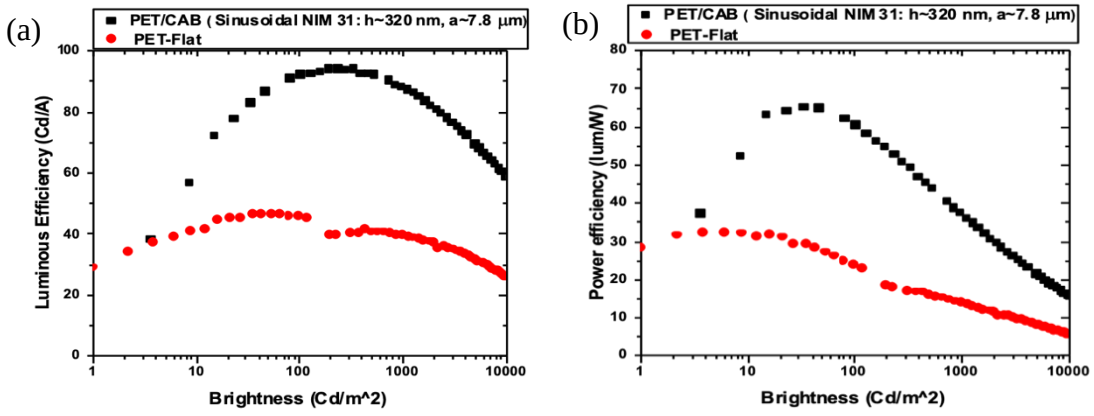

Figure 5.4: (a) η_L- L curve ; (b) η_P- L curve

Both, luminous efficiency (η_L) and power efficiency (η_P) as depicted on ***Figure 5.4*** shows that the OLED on patterned substrate is two times efficient to the reference.

The EQE of the corrugated device is ~32.5%, ~2x increase in comparison to a reference device on flat PET with EQE ~17% as shown in ***Figure 5.5.*** This increment is significant in terms of the light extraction. The merit of these devices is on ***Table 5.2***.

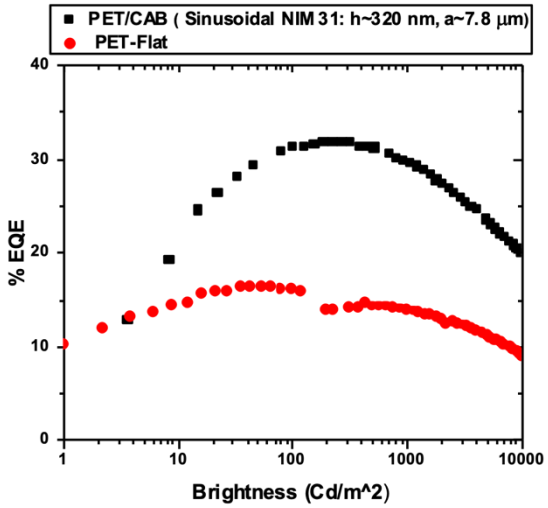

Figure 5.5: EQE vs brightness plot showing a two- fold enhancement for a WOLED on a patterned PET substrate with respect to control device on a flat PET.

Table 5.2: Efficiencies for WOLED on patterned and flat PET

Device / *Efficiency*	*Patterned (1,000 nits)*	*Flat (1,000 nits)*	*Enhancement* (1,000 nits)*	*Patterned (peak nits)*	*Flat (peak nits)*
External Quantum Efficiency (%)	30	14	**x2.1**	32 (326)	16.5 (54)
Luminous Efficiency (Candela/Amp)	88	40	**x2.2**	95 (248)	47 (65)
Power Efficiency (lumen/Watt)	37	14	**x2.6**	66 (35)	32 (17)

**Bold figures are the ratio of patterned to the flat;* $1\ nit = 1\ Cd/m^2$

5.3.4 Corrugation Effect

Patterned OLEDs on corrugated plastic substrates show enhanced light outcoupling in blue, green, and white OLEDs. As supported by simulations, this is due to minimizing internal waveguiding in the organics + anode and surface plasmon excitation at the organic/metal electrode interface [14]. EQE enhancements were observed for OLEDs on two different patterned plastic substrates (polycarbonate & PET) with convex or concave structures of different pitch and height/depth features. The substrates and devices were broadly characterized, including tracking the corrugation from the substrate to the top metal electrode. The following section via imaging techniques viz., FIB, SEM, Optical Microscopy, and AFM, demonstrates the complete conformality of the OLED stack fabricated on the micro-patterned concave PET [15].

5.3.4.1 FIB analysis

Conformal OLED: As shown in ***Figure 5.6,*** the WOLED on the 7.8 μm pitch PET is fully conformal. The layers are stacked uniformly throughout the device, including the cathode.

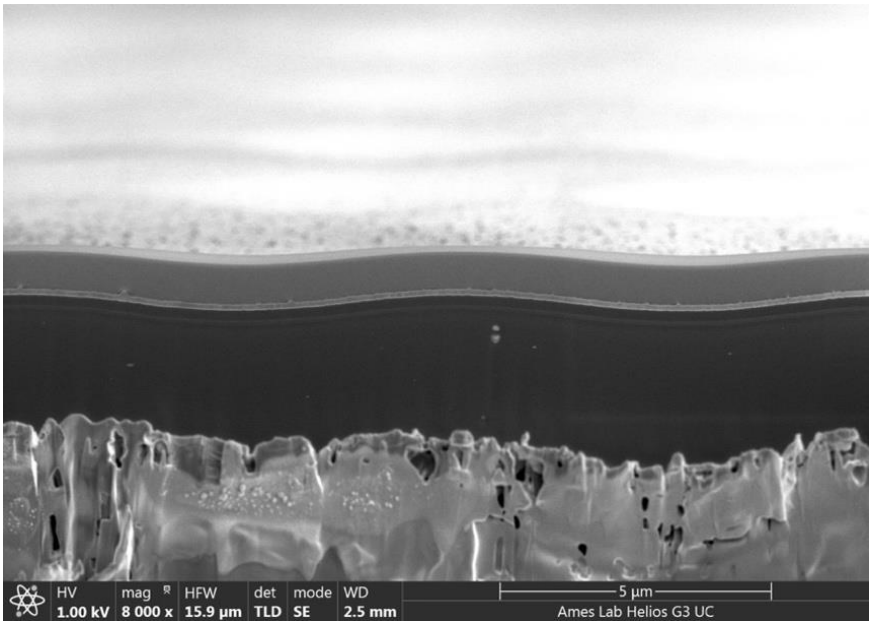

Figure 5.6: FIB image of the conformal WOLED on micro-patterned PET

Layer Thicknesses*:** As evident from ***Figure 5.7, which is a high-resolution image of the stack, the layers retain their uniformity and expected throughout the stack. ***Table 5.3*** compares the thicknesses of the OLED layers based on the FIB image to those obtained during device fabrication based on the crystal monitor reading. As seen, the values are in close agreement.

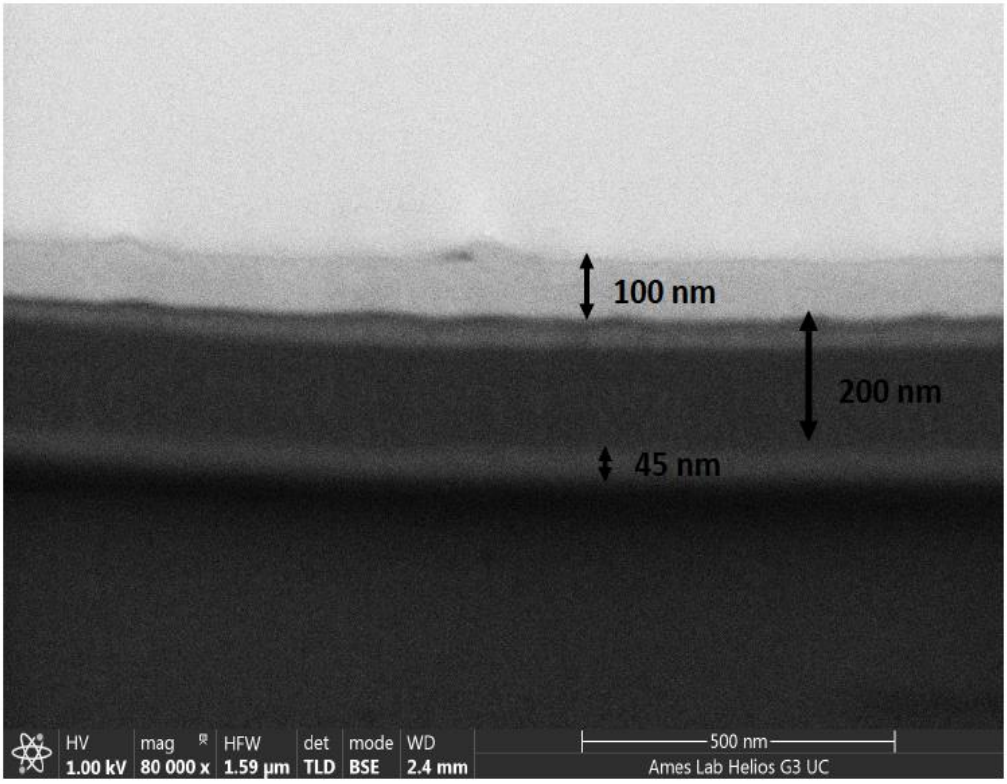

Figure 5.7: FIB cross-section of the Conformal White OLED

Table 5.3: Comparison between FIB and crystal monitor thicknesses

Device Layer	*FIB thickness (nm)*	*Thickness Monitor (nm)*
Anode (PEDOT: PSS)	45	-estimated ~35 [16]
Organic total	~ 200	~ 226
Cathode (Aluminum)	~ 100	~ 100

5.3.4.2 Additional imaging techniques

SEM: The top surface of the WOLED was also probed using SEM. SEM image in ***Figure 5.8*** clearly shows that the corrugation is retained all the way till the top OLED surface. In the image, the top organic surface is on the right and the top cathode (Aluminum) surface is on the left with the interface in the middle.

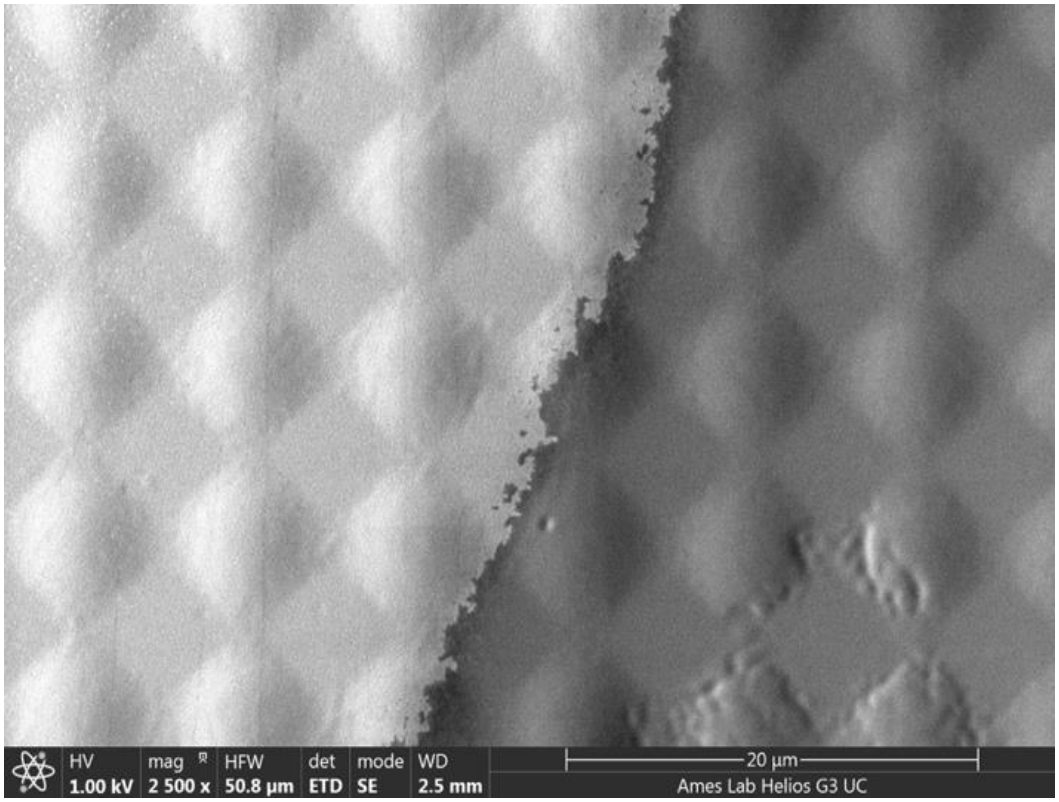

Figure 5.8: SEM image of the top surface of the White OLED; Left to the interface Aluminum surface and to its right top organic surface.

AFM: The optical microscope image on the AFM set up in ***Figure 5.9*** provide image similar to ***Figure 5.8***. The red spot in the image is the laser spot used for the AFM alignement. The interface on the image separates Aluminum surface on the right from the organic surface to the left. Separate contrast between the two surface is due to metallic nature of Aluminum which more is reflective to the light compared to the organic surface.

Figure 5.10 is the AFM image of $80\ \mu m \times 80\ \mu m$ for the WOLED surface. Two distinct surfaces separated by the yellow dotted line corresponds to the cathode surface and the orgnic surface.The shinnier surface towards the upper side of the dotted line is the cathode surface that has +100 nm of Al coating to the organic surface. The lower to the dotted line is the top organic surface.

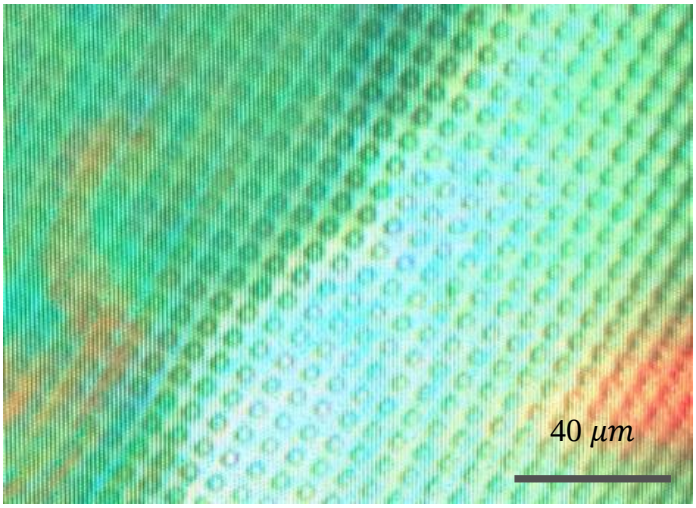

Figure 5.9: Optical microscope image of the WOLED surface.

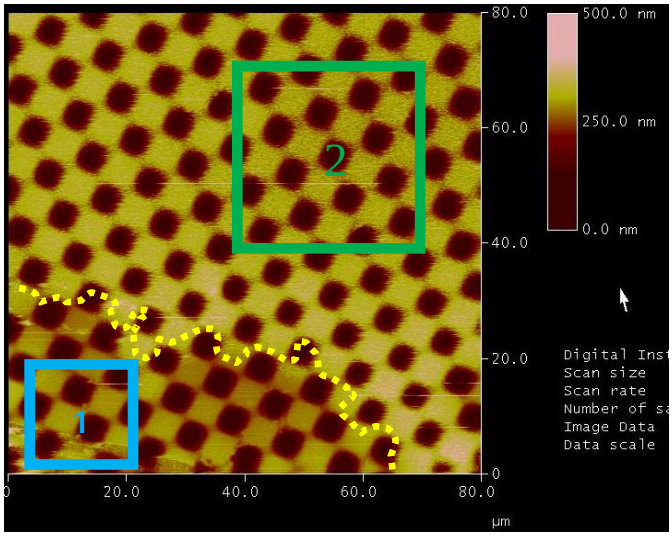

Figure 5.10: (80 μm × 80 μm)The checker board like pattern with two distinct regions separated by the dotted line. The region below dotted yellow line with shady darker squares is the organic top layer, whereas the region above the dotted yellow line with the shinier squares is the Al surface. The Al surface is on a higher plane (+100 nm) than the organic layer as inferred from the color map.

The detail of the surface profile of these two regions are provided on ***Figure 5.11.*** The corrugation h ~ 230 nm on the top OLED surface suggest that the ample amount of corrugation is retained throughout the stacks. The surface profile is sinusoidal closely resembling to the substrate profile of ***Figure 5.1.*** For the full conformal layer, the h~ 230 nm fall short but this could be due to the instrumental limitation.

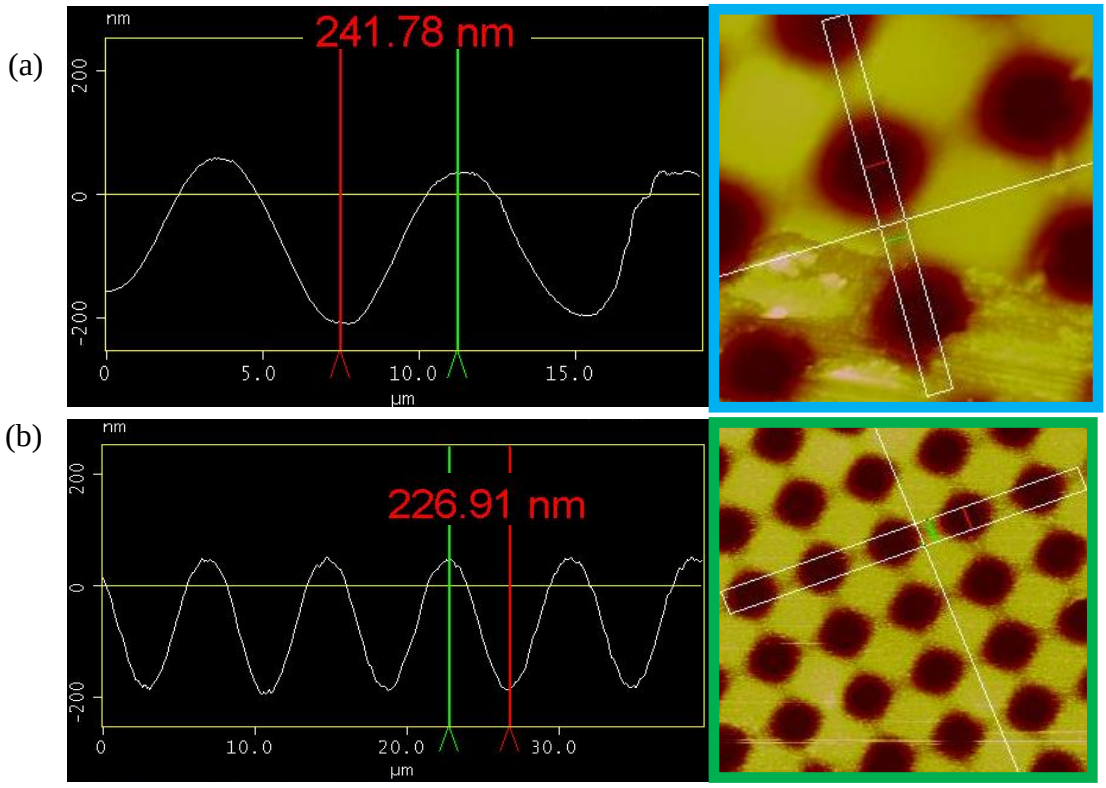

Figure 5.11: (a) $(20\ \mu m\ \times\ 20\ \mu m)$ *surface profile and the top organic surface. (b)* $(40\ \mu m\ \times\ 40\ \mu m)$ *surface and the top Al surface.*

5.4 Concluding Remarks

OLED lighting is still in its formative years, despite having superior light quality in comparison to LEDs in many respects [1,2]. Most of the OLED lighting products are used mostly for aesthetic purpose and are limited to small scale manufacturing [1,2]. The higher

manufacturing cost per unit is one of the major hurdles for its way to mass production. Before realizing its full commercialization potential issues like lower efficiencies and shorter blue emission life time-need to be addressed [1,2].

As shown in this chapter, the use of corrugated plastic substrates addresses the issue of low light outcoupling and presents an approach to reducing cost using R2R fabrication of enhancing substrates.

5.5 Experimental procedure

5.5.1 Materials

The flat and patterned PET/CAB substrates for this work were fabricated by MicroContinuum, Inc. The conductive polymer PEDOT: PSS, used as the anode, was from Heraues Clevios company. LiF was from Sigma-Aldrich. MoO_3 was from Sterm Chemicals, and HAT-CN, TAPC, TmPyPB, mCP, PO-01 and FIrpic from Luminescence Technology Corporation.

5.5.2 AFM characterization

Veeco Metrology Scanning Probe Microscopy is the scanner. AFM tips model TESPA-V2 were purchased from Bruker Company (brukerafmprobes.com). The tips are made up of Antimony (n) doped Si with a resistivity of 0.01-0.025 Ohm-cm. These tips have a resonant frequency of 320 kHz and a spring constant of 42 N/m. The tips were 125 μm long and 40 μm wide without any coating on the front side, whereas the backside had 50±10nm Al.

5.5.3 PEDOT: PSS film fabrication and characterization

The PEDOT: PSS solution was mixed with 6 v% EG and 1 v% Capstone FS35 fluorosurfactant. The mixed solution was filtered using a 0.45 μm syringe filter; it was spin-

coated at 6000 rpm for 30 s (optimized). This was followed by annealing the film at 80oC for 2 hrs.

5.5.4 FIB Imaging

For analysis of the OLED structure and stack conformality we used a FEI Helios Dual Beam FIB/SEM system that combines milling, imaging, and analytical capabilities. The system enables very precise ion milling in selected areas as well as high-resolution 3-D microscopy. A beam of gallium ions is used for nm milling and imaging precision, depending on the ion energy and intensity; the Ga^+ ion source can image and machine down to 5 nm resolution levels. Image J software was used for determining feature in the FIB image.

5.5.5 OLED fabrication and characterization

OLEDs with a PEDOT: PSS anode were fabricated on corrugated and flat plastic substrates. The Al cathode and all organic materials were deposited by thermal evaporation inside a chamber with a base pressure of $<10^{-6}$ mbar within a glovebox. The Al cathode was deposited through a shadow mask containing 1.5 mm diameter circular holes. Characterization of the OLEDs was done using a Keithley 2400 source meter to apply a voltage and measure the current. The brightness was measured by a Minolta LS110 luminance meter and the EL spectra were obtained using an Ocean Optics PC2000-ISA spectrometer. Labview software was used to calculate the efficiencies from the experimental data.

5.6 References

[1] National Research Council. 2013. *Assessment of Advanced Solid-State Lighting*. Washington, DC: The National Academies Press. https://doi.org/10.17226/18279.

[2] National Research Council. Committee on Assessment of Solid-State Lighting.2017. *Assessment of Solid-state Lighting, Phase Two / Committee on Assessment of Solid-State*

Lighting, Phase 2, Board on Energy and Environmental Systems, Division on Engineering and Physical Sciences.

[3] https://www.oledworks.com/about/

[4] Koden, M. (2017). *OLED displays and lighting / Mitsuhiro Koden.* (Wiley series in display technology).

[5] Gaspar, D., & Polikarpov, E. (2015). *OLED fundamentals: Materials, devices, and processing of organic light-emitting diodes / edited Daniel J. Gaspar, Evgueni Polikarpov*

[6] Buckley, A. (2013). *Organic light-emitting diodes (OLEDs): Materials, devices and applications / edited by Alastair Buckley.* (Woodhead Publishing series in electronic and optical materials; no. 36).

[7] Wang, D., Hauptmann, J., & May, C. (2019). OLED Manufacturing on Flexible Substrates Towards Roll-to-Roll. *MRS Advances, 4*(24), 1367-1375. doi:10.1557/adv.2019.62

[8] Kido, J., Hongawa, Okuyama, & Nagai. (1994). White light-emitting organic electroluminescent devices using the poly(N -vinylcarbazole) emitter layer doped with three fluorescent dyes. *Applied Physics Letters, 64*(7), 815-817.

[9] Jeon, Sohee, Lee, Sunghun, Han, Kyung-Hoon, Shin, Hyun, Kim, Kwon-Hyeon, Jeong, Jun-Ho, & Kim, Jang-Joo. (2018). High-Quality White OLEDs with Comparable Efficiencies to LEDs. *Advanced Optical Materials, 6*(8), 1-8.

[10] Qu, Y., Kim, J., Coburn, C., & Forrest, S. (2018). Efficient, Nonintrusive Outcoupling in Organic Light Emitting Devices Using Embedded Microlens Arrays. *ACS Photonics, 5*(6), 2453-2458.

[11] Zhou, Lei, Xiang, Heng-Yang, Shen, Su, Li, Yan-Qing, Chen, Jing-De, Xie, Hao-Jun, Goldthorpe, Irene A, Chen, Lin-Sen, Lee, Shuit-Tong, and Tang, Jian-Xin. (2014). High-performance flexible organic light-emitting diodes using embedded silver network transparent electrodes. *ACS Nano, 8*(12), 12796-12805

[12] Hippola, Chamika, Kaudal, Rajiv, Manna, Eeshita, Xiao, Teng, Peer, Akshit, Biswas, Rana, Slafer, Warren Dennis, Trovato, Tom, Shinar, Joseph, and Shinar, Ruth. (2018). Enhanced Light Extraction from OLEDs Fabricated on Patterned Plastic Substrates. *Advanced Optical Materials, 6*(4), 1-11.

[13] http://www.lumtec.com.tw/

[14] Salehi, A., Fu, X., Shin, D., & So, F. (2019). Recent Advances in OLED Optical Design. *Advanced Functional Materials, 29*(15), 1-21.

[15]https://www.energy.gov/sites/prod/files/2017/02/f34/forrest_oledoutcoupling_longbeach2017.pdf

[16] Cai, Min, Ye, Zhuo, Xiao, Teng, Liu, Rui, Chen, Ying, Mayer, RobertBiswas, Rana, Ho, Kai-Ming, Shinar, Ruth, and Shinar, Joseph. (2012). Extremely efficient indium-tin-oxide-free green phosphorescent organic light-emitting diodes. *Advanced Materials (Deerfield Beach, Fla.)*, *24*(31), 4337-4342

CHAPTER 6. SUMMARY AND CONCLUSIONS

This dissertation as summarized below juxtaposes on the two realms of OLEDs; its substrate design and the enhanced light extraction.

1. Design aspect of the patterned substrate

AFM, as a metrology tool, is effective on unraveling substrate surface properties whether planar or patterned and hence can be used for the optimization of the substrate design. From it, both qualitative and the quantitative traits of the substrate can be assessed at the same time. The qualitative aspect shows surface impeccability as well as the pattern smoothness and its behavior on the turning points. The color map of the pattern is implicative of its homogeneity and uniformity. Patterns' period, height/depth and their ratio as a quantitative metric is valuable while evaluating the shape and form of OLED stack. Conformal OLED is a precursor for the uniform charge transport and plays crucial role on the field driven devices like OLEDs.

2. Enhanced light extraction

Energetics of the OLED is the principal factor that reigns its performance. Careful energetics is the result of judicious choice of materials that takes into account its physical and chemical properties. Other factors like the layer thicknesses, the layer position in the stack, and doping concentration of the transport layer are equally important. Enhancement in the OLED infers that all the parameters that EQE depends on viz., charge balance, singlet/triplet excitons, radiative recombination are optimized.

In a nutshell, this dissertation successfully demonstrates the feasibility of the low cost corrugated plastic substrate; both PC and PET as a viable means for the enhanced light extraction from the OLEDs.